Final Report
Grant DE-FG02-04ER54752
Intense Magnetized Plasma-Wall Interaction
Feb 15, 2008 – Aug 31, 2013

PI: Bruno S. Bauer, University of Nevada, Reno (UNR)

DOE/Office of Science Program Office: Office of Fusion Energy Sciences (OFES)
DOE/Office of Science Program Technical Program Manager Contact: Dr. Sean Finnegan

Table of Contents

1 Executive Summary 3
2 Publications and Conference Contributions 4
2.1 Publications 4
2.2 Conference Contributions 6
3 Photodiode Array Temperature Calibration 17
3.1 Rayleigh-Jeans Law 19
3.2 Convolution of Planck Blackbody with filters and responsivity 20
3.3 Zemax Ray Tracing 22
3.4 Photodiode Array Test Performed with a Quartz Tungsten Halogen Lamp 24
4 X-Ray Radiography 26
5 EUV Spectroscopy 32
5.1 EUV Spectrometer Dispersion Corrections & PrismSPECT Units Conversion 32
5.2 Spectrometer Calibration 35
5.3 Dispersion Correction for Measured Spectral Intensities 37
5.4 Comparing PrismSPECT Modeling Results with Experimental EUV Spectra 38
5.5 Line-of-sight Integration through R-MHD Modeling Results 39
5.6 Image & Data Processing for the MCP Images of the EUV Spectrometer 40
5.7 Subtraction of MCP Background from the Exponential Decay 42
5.8 ImageJ EUV Spectral Image Corrections 47
5.9 Image Shift Java Code 48
5.10 Background Subtraction ImageJ Java Code 49

5.11 ImageJ Macros 52
5.12 MCP Sensitivity Corrections 52
5.13 Conclusions 54
6 Collaboration on FRCHX and PLX Experiments 55
6.1 Development of a 7-Channel Bias Box for Photodiode Arrays 55
6.2 Electron Impact from Plasma on Al-Coated AXUV Photodiodes 60
6.3 Calculation of Signal Levels from PrismSPECT Ar Plasma Emission Modeling 63
6.3.1 Collection optics 63
6.3.2 Timing considerations and lens *F/#* 63
6.3.3 Ideal lens 64
6.3.4 Collection optics for best lens 64
6.3.5 Energy interval 65
6.3.6 Intensity estimate for Te = 3 eV, n = 10^{17} cm^{-3}, thickness 1cm, non-LTE 65
6.3.7 Intensity estimate for Te = 1 eV, $n = 10^{15}$ cm^{-3}, thickness 1cm, non-LTE 66
6.3.8 Conclusions 66
6.4 CCD Camera Adaptation to a Jobin-Yvon CP-140 Compact Spectrometer 66

1 Executive Summary

This research project studied wall-plasma interactions relevant to fusion science. Such interactions are a critical aspect of Magneto-Inertial Fusion (MIF) because flux compression by a pusher material, in particular the metal for the liner approach to MIF, involves strong eddy current heating on the surface of the pusher, and probably interactions and mixing of the pusher with the interior fuel during the time when fusion fuel is being burned. Given the energy density and magnetic fields involved with MIF, no pusher material will act like room-temperature material. Thus understanding how the pusher responds to megagauss magnetic field and intense plasma radiation is very important.

When the pusher material is a metal liner, high-energy-density conditions result in fascinating behavior. For example, "warm dense matter" is produced, for which material properties such as resistivity and opacity are not well known. Understanding this behavior is useful for optimizing the performance of the liner inner surface in an MIF implosion.

In this project, the transformation into plasma of metal walls subjected to pulsed megagauss magnetic fields was studied with an experiment driven by the UNR 1-MA Zebra generator. This experiment was numerically simulated with using the MHRDR code. This simple, fundamental high-energy-density physics (HEDP) experiment, in a regime appropriate to MIF, has stimulated an important and fascinating comparison of numerical modeling codes and tables with experiment. In addition, we participated in developing the FRCHX experiment to compress a field-reversed-configuration (FRC) plasma with a liner, in collaboration with researchers from Air Force Research Laboratory (AFRL) and Los Alamos National Lab (LANL), and we helped develop diagnostics for the Plasma Liner Experiment (PLX) at LANL.

This project has also enabled us to train students in high-energy-density physics. 3 graduate students, Milena Angelova, Thomas Awe, and Tasha Goodrich, completed their dissertations:

- T.J. Awe, *Experimental Investigation of the Properties and Phase State of Thick Aluminum Surfaces Pulsed to Megagauss Level Magnetic Field in a Z-Pinch Geometry*, Ph.D. Dissertation, UNR, December 2009.
- M.A. Angelova, *Numerical Study of Plasma Formation from Current Carrying Conductors*, Ph.D. Dissertation, UNR, May 2010.
- T.S. Goodrich, *Time Resolved Visible Spectroscopy of Surface Plasma Radiation*, M.S. Thesis, UNR, May 2010.

Milena Angelova and Thomas Awe were awarded PhD degrees, and Tasha Goodrich was awarded an M.S. Their dissertations are available upon request. They provide comprehensive descriptions of the experiment and the modeling.

Most of the results of this project are described in the publications listed in Section 2.1, in the dissertations listed above, and in the technical materials provided in previous reports. Recent technical results are provided in Sections 3 to 6 of this report. Many researchers, students, and staff have contributed to this work, and, implicitly or explicitly, to this report. UNR contributors

include, in addition to the PI, Richard Siemon, Stephan Fuelling, Irvin Lindemuth, Ioana Paraschiv, Milena Angelova, Tom Awe (now at Sandia National Laboratories), Tasha Goodrich, and Kevin Yates. We also thank our external and internal collaborators for many valuable interactions.

2 Publications and Conference Contributions

2.1 Publications

1. M.A. Angelova, B.S. Bauer, R.E. Siemon, I.R. Lindemuth, and V. Makhin, *Sensitivity of m=0 instability to different resistivity models*, IEEE Transactions on Plasma Science **36**, 37 (2008).
2. S. Fuelling, T.J. Awe, B.S. Bauer, T. Goodrich, A. Haboub, V.V. Ivanov, V. Makhin, A. Oxner, R. Presura, and R.E. Siemon, *A Zebra Experiment to Study Plasma Formation by Megagauss Fields*, IEEE Transactions on Plasma Science **36**, 62 (2008).
3. A.A. Esaulov, B.S. Bauer, V. Makhin, R.E. Siemon, I.R. Lindemuth, T.J. Awe, R.E. Reinovsky, K.W. Struve, M.P. Desjarlais, and T.A. Melhorn, *Radiation magnetohydrodynamic simulation of plasma formed on a surface by a megagauss field*, Phys. Review E **77**, 036404, http://link.aps.org/abstract/PRE/v77/e036404 (2008).
4. R.E. Siemon, B.S. Bauer, T.J. Awe, W.L. Atchison, M.A. Angelova, S. Fuelling, T. Goodrich, I.R. Lindemuth, V. Makhin, W.L. Atchison, R.J. Faehl, R.E. Reinovsky, P.J. Turchi, J.H. Degnan, E.L. Ruden, M.H. Frese, S.F. Garanin, and V.N. Mokhov, *The Challenge of Wall-Plasma Interaction with pulsed Megagauss Magnetic Fields*, J. Fusion Energy **27**, 235, http://www.springerlink.com/content/c01q368w00408571 (2008).
5. I. Paraschiv, B.S. Bauer, I.R. Lindemuth, V. Makhin, 'Linear and nonlinear development of the *m* =0 instability in z-pinch equilibria with axial sheared flows,' J. Fusion Energy, http://dx.doi.org/10.1007/s10894-008-9174-x (2008).
6. I. Paraschiv, B.S. Bauer, I.R. Lindemuth, V. Makhin, 'Linear and nonlinear development of the *m* =0 instability in z-pinch equilibria with axial sheared flows,' Proceedings of the 2008 Innovative Confinement Concepts Workshop, Reno, Nevada, June 24-27, 2008, J. Fusion Energy **28**, 195 http://www.springerlink.com/openurl.asp?genre=article&id=doi:10.1007/s10894-008-9174-x (2009).
7. I.R. Lindemuth, R.E. Siemon, B.S. Bauer, M.A. Angelova, W.L. Atchison, S.F. Garanin, and V. Makhin, 'Numerical simulation of metallic surface plasma formation by megagauss magnetic fields,' Proceedings of the 17th IEEE International Pulsed Power Conference, Washington, DC, June 28 – July 2, 2009, Proc. IEEE PPC '09, pp. 193-199, http://ieeexplore.ieee.org/stamp/stamp.jsp?tp=&arnumber=5386244 (2009).
8. T.J. Awe, B.S. Bauer, S. Fuelling, and R.E. Siemon, 'Threshold for thermal ionization of an aluminum surface by pulsed megagauss magnetic field,' Phys. Rev. Lett. **104**, 035001, http://link.aps.org/doi/10.1103/PhysRevLett.104.035001 (2010).

9. I.R. Lindemuth, R.E. Siemon, B.S. Bauer, M.A. Angelova, and W.L. Atchison, 'Computational interpretation of megagauss-magnetic-field-induced metallic surface plasma initiation and evolution,' Phys. Rev. Lett. **105**, 195004, http://prl.aps.org/abstract/PRL/v105/i19/e195004 (2010).

10. T.J. Awe, B.S. Bauer, S. Fuelling, I.R Lindemuth, and R.E. Siemon, 'Experimental investigation of thermal plasma formation from thick aluminum surfaces by pulsed multi-megagauss magnetic field,' Phys. Plasmas **17**, 102507 http://pop.aip.org/resource/1/phpaen/v17/i10/p102507_s1 (2010).

11. I. Paraschiv, B.S. Bauer, I.R. Lindemuth, and V. Makhin, 'Linear and nonlinear development of the m =0 instability in a diffuse Bennett z-pinch equilibrium with sheared axial flow,' Phys. Plasmas **17**, 072107-1-10, http://link.aip.org/link/?PHP/17/072107 (2010).

12. S.F. Garanin, S.D. Kuznetsov, W.L. Atchison, R.E. Reinovsky, T.J. Awe, B.S. Bauer, S. Fuelling, I.R. Lindemuth, R.E. Siemon, 'Numerical simulations of thick aluminum wire behavior under megaampere current drive,' IEEE Trans. Plasma Sci. **38**, 1815 (2010).

13. T.J. Awe, B.S. Bauer, S. Fuelling, and R.E. Siemon, "Mitigation of nonthermal plasma production to measure the pulsed magnetic field threshold for the thermal formation of plasma from thick aluminum surfaces," Phys. Plasmas 18, 056304 (2011) http://link.aip.org/link/?PHP/18/056304

14. "The evolving structure of plasma formed from the surface of aluminum rods driven to megaampere current," T.J. Awe, B.S. Bauer, S. Fuelling, and R.E. Siemon, IEEE Trans. Plasma Sci. 39, 2418 (2011) http://ieeexplore.ieee.org/xpl/freeabs_all.jsp?arnumber=5776691

15. C. Grabowski, J.H. Degnan, D.J. Amdahl, R. Delaney, M. Domonkos, F.M. Lehr, R. Magallanes, P.R. Robinson, E.L. Ruden, W. White, H. Wood, D. Gale, M. Kostora, J. McCullough, W. Sommars, M.H. Frese, S.D. Frese, J.F. Camacho, S.K. Coffey, V. Makhin, T.P. Intrator, G.A. Wurden, J. Sears, P.J. Turchi, W.J. Waganaar, T. Weber, R.E. Siemon, S. Fuelling, B.S. Bauer, A.G. Lynn, and N.F. Roderick, 'FRC lifetime studies for the field reversed configuration heating experiment (FRCHX),' Proceedings of the 18th IEEE Int'l Pulsed Power Conference, Chicago, IL, June 19-23, 2011, Proc. IEEE PPC '11, pp. 431-436 (2011).

16. I.R. Lindemuth, R.E. Siemon, B.S. Bauer, and W.L. Atchison, 'Verification and Validation Adventures in Simulating Megagauss-Magnetic-Field-Induced Plasma Formation on Thickwire Metallic Surfaces,' submitted to the Proceedings of the 14th Int'l Conference on Megagauss Magnetic Field Generation and Related Topics, Maui, Hawaii, October 14 – 19, 2012.

2.2 Conference Contributions

UNR-Megagauss-Experiment Computational Modeling Workshop
University of Nevada, Reno, April 7-9, 2008

1. T.J. Awe, B.S. Bauer, R.E. Siemon, S. Fuelling, I.R. Lindemuth, V. Makhin, *Overview of Zebra Megagauss Experiment*, presented (oral) at UNR-Megagauss-Experiment Computational Modeling Workshop, Reno, Nevada, April 7-9, 2008.
2. V. Makhin, *Numerical Modeling of Behavior of 1 mm Aluminum Wire under the Zebra 1 MA Current*, presented (oral) at UNR-Megagauss-Experiment Computational Modeling Workshop, Reno, Nevada, April 7-9, 2008.
3. R.E. Siemon, *Questions/ideas regarding ionization process*, presented (oral) at UNR-Megagauss-Experiment Computational Modeling Workshop, Reno, Nevada, April 7-9, 2008.
4. I.R. Lindemuth, *MHRDRing the UNR Megagauss Experiment: Code Issues and Sensitivities*, presented (oral) at UNR-Megagauss-Experiment Computational Modeling Workshop, Reno, Nevada, April 7-9, 2008.
5. M.A. Angelova, *Numerical Study of Plasma Formation from Al Rods Driven by Megaampere Zebra Current*, presented (oral) at UNR-Megagauss-Experiment Computational Modeling Workshop, Reno, Nevada, April 7-9, 2008.
6. I. Paraschiv, *Progress on stability investigations*, presented (oral) at UNR-Megagauss-Experiment Computational Modeling Workshop, Reno, Nevada, April 7-9, 2008.
7. A.A. Esaulov, B.S. Bauer, V. Makhin, R.E. Siemon, I.R. Lindemuth, T.J. Awe, R.E. Reinovsky, K.W. Struve, M.P. Desjarlais, and T.A. Mehlhorn, *Radiation MHD simulation of plasma formed on a surface by a MG-field*, presented (oral) at UNR-Megagauss-Experiment Computational Modeling Workshop, Reno, Nevada, April 7-9, 2008.

2008 APS April Meeting and HEDP/HEDLA Meeting
St. Louis, Missouri, April 11-15, 2008

8. T.J. Awe, B.S. Bauer, R.E. Siemon, S. Fuelling, I.R. Lindemuth, V. Makhin, *Plasma Formation on the Surface of mm-Diameter Aluminum Rods by Pulsed Megagauss Magnetic Field*, K1.00048, p.93, presented at the 2008 APS April Meeting and HEDP/HEDLA Meeting, St. Louis, Missouri, April 11-15, 2008.
9. S. Fuelling, B.S. Bauer, R.E. Siemon, T.J. Awe, V. Makhin, T. Goodrich, A. Oxner, R. Presura, *EUV plasma emission from an aluminum surface driven by MG fields*, K1.00043, p.93, presented at 2008 APS April Meeting and HEDP/HEDLA Meeting, St. Louis, Missouri, April 11-15, 2008.
10. V. Makhin, M.A. Angelova, T.J. Awe, B.S. Bauer, I.R. Lindemuth, I. Paraschiv, and R.E. Siemon, *The generation of warm dense matter according to numerical modeling of thick wire heating*, K1.00036, p.92, presented at 2008 APS April Meeting and HEDP/HEDLA Meeting, St. Louis, Missouri, April 11-15, 2008.

Innovative Confinement Concepts 2008 Workshop
University of Nevada, Reno, June 24-27, 2008

11. T.J. Awe, B.S. Bauer, S. Fuelling, I.R. Lindemuth, V. Makhin, R.E. Siemon, *Pulsed Megagauss Magnetic Field on Millimeter Diameter Aluminum Rods*, presented (poster) at Innovative Confinement Concepts 2008 (ICC2007) Workshop, Reno, Nevada, June 24-27, 2008.
12. B.S. Bauer, T.J. Awe, M.A. Angelova, A. Esaulov, S. Fuelling, T.S. Goodrich, B. Le Galloudec, I.R. Lindemuth, V. Makhin, A. Oxner, R. Presura, and R.E. Siemon, *Plasma formation and evolution from an aluminum surface driven by a multi-megagauss field as in Magneto-Inertial Fusion*, presented (oral) at Innovative Confinement Concepts 2008 (ICC2007) Workshop, Reno, Nevada, June 24-27, 2008.
13. Volodymyr Makhin, Milena Angelova, Thomas Awe, Bruno Bauer, Irvin Lindemuth, Ioana Paraschiv, Richard Siemon, *Numerical modeling of Zebra MG experiment shows generation of warm dense matter and surface plasma*, presented (poster) at Innovative Confinement Concepts 2008 (ICC2007) Workshop, Reno, Nevada, June 24-27, 2008..

XII International Conference on Megagauss Field Generation and Related Topics
Novosibirsk, Russia, July 13-18, 2008

14. T. J. Awe, B. S. Bauer, R. E. Siemon, S. Fuelling, V. Makhin, M. A. Angelova, T. Goodrich, B. Le Galloudec, I. R. Lindemuth, I. Paraschiv, R. Presura, W. L. Atchison, R. J. Faehl, R. E. Reinovsky, P. J. Turchi, J. H. Degnan, E. L. Ruden, M. H. Frese, S. F. Garanin, and V. N. Mokhov, *Plasma Formation and Evolution from Thick Aluminum Wires Pulsed with Megagauss Field*, presented (oral) at XII International Conference on Megagauss Field Generation and Related Topics, Novosibirsk, Russia, July 13-18, 2008.

7th International Conference on Dense Z-Pinches
Alexandria, Virginia, August 18-21, 2008

15. B.S. Bauer, T.J. Awe, M.A. Angelova, A.A. Esaulov, S. Fuelling, T.S. Goodrich, B. Le Galloudec, I.R. Lindemuth, V. Makhin, A. Oxner, R. Presura, and R.E. Siemon, *Plasma formation and evolution from an aluminum surface driven by a megagauss field*, presented (oral) at 7th International Conference on Dense Z-Pinches, Alexandria, Virginia, August 18-21, 2008.
16. I.R. Lindemuth, *MHRDRing Z-Pinches and Related Geometries: Four decades of computational modeling using still unconventional methods*, presented (poster) at 7th International Conference on Dense Z-Pinches, Alexandria, Virginia, August 18-21, 2008.
17. T.J. Awe, B.S. Bauer, S. Fuelling, R.E. Siemon, B. Le Galloudec, I.R. Lindemuth, V. Makhin, *Dynamics of Thick Aluminum Wires Pulsed with Megagauss Magnetic Field*, presented (oral) at 7th International Conference on Dense Z-Pinches, Alexandria, Virginia, August 18-21, 2008.

18. M.A. Angelova, V. Makhin, B.S. Bauer, I.R. Lindemuth, and R.E. Siemon, *Numerical Study of Plasma Formation from Thick and Thin Aluminum Rods Driven by Megaampere Currents*, presented (oral) at 7th International Conference on Dense Z-Pinches, Alexandria, Virginia, August 18-21, 2008.

50th Annual Meeting of the APS Division of Plasma Physics
Dallas, Texas, Nov. 17-21, 2008

19. T.P. Intrator, G.A. Wurden, P.E. Sieck, W.A. Waganaar, X. Sun, A. Lynn, M. Gilmore, T. Awe, R.E. Siemon, J. Degnan, E.L. Ruden, M. Domonkos, P. Adamson, T.C. Grabowski, D. Gale, M.H. Frese, S.D. Frese, J.F. Camacho, S.K. Coffey, N.F. Roderick, D.J. Amdahl, P. Parks, 'Overview of FRC Translation Experiments For Magnetized Target Fusion,' presented (poster) at 50th Annual Meeting of the APS Division of Plasma Physics, Dallas, Texas, Nov 17-21, 2008.
20. J.H. Degnan, P. Adamson, M. Domonkos, E.L. Ruden, C. Grabowski, D. Brown, D. Gale, M. Kostora, D. Ralph, W. Sommars, M.H. Frese, S.D. Frese, D.J. Amdahl, J.F. Camacho, S.K. Coffey, T.P. Intrator, G.A. Wurden, S.C. Hsu, P. Sieck, P.J. Turchi, W.J. Waganaar, R.E. Siemon, T.J. Awe, A.G. Lynn, N.F. Roderick, 'Field Reversed Configuration (FRC) Formation And Compression Using Liners,' presented (poster) at 50th Annual Meeting of the APS Division of Plasma Physics, Dallas, Texas, Nov 17-21, 2008.

UNR College of Science Poster Competition
UNR, Reno, Nevada, April 23-24, 2009

21. T.J. Awe, B.S. Bauer, S. Fuelling, R.E. Siemon, I.R. Lindemuth, and V. Makhin, 'Thermal Ionization of Aluminum Surfaces Pulsed with Multi-Megagauss Magnetic Field,' presented (poster) at the University of Nevada, Reno College of Science Poster Competition, Reno, Nevada, April 23-24, 2009.

2nd International Conference on High Energy Density Physics
Austin, Texas, May 19-22, 2009

22. T.J. Awe, B.S. Bauer, R.E. Siemon, S. Fuelling, and V. Makhin, 'Thermal Ionization of an Aluminum Surface Pulsed with MG Magnetic Field,' presented (poster) at the 2nd International Conference on High Energy Density Physics, Austin, Texas, May 19-22, 2009.

36th International Conference on Plasma Science
and 23rd Symposium on Fusion Engineering
San Diego, California, May 31 – June 5, 2009

23. B.S. Bauer, T.J. Awe, M.A. Angelova, S. Fuelling, T.S. Goodrich, B. Le Galloudec, I.R. Lindemuth, R.E. Siemon, V. Makhin, W.L. Atchison, and S.F. Garanin, 'Thermal Ionization of an Aluminum Surface by Pulsed Megagauss Field', presented (oral IO3C-5) at the 36th IEEE International Conference on Plasma Science, San Diego, California, May 31 – June 5, 2009.

24. T.J. Awe, B.S. Bauer, R.E. Siemon, S. Fuelling, I.R. Lindemuth, and V. Makhin, 'Experimental Study of Plasma Formation on an Aluminum Surface Pulsed with Megagauss Magnetic Field', presented (oral IO3C-6) at the 36th IEEE International Conference on Plasma Science, San Diego, California, May 31 – June 5, 2009.

25. M.A. Angelova, V. Makhin, B.S. Bauer, I.R. Lindemuth, and R.E. Siemon, 'Numerical Study of Plasma Formation from Aluminum Rods Driven by Megaampere Currents', Poster IP2D-32, presented at the 36th IEEE International Conference on Plasma Science, San Diego, California, May 31 – June 5, 2009.

26. J.H. Degnan, P. Adamson, D.J. Amdahl, R. Delaney, M.T. Domonkos, G. Gruen, M. Lehr, E.L. Ruden, W. Tucker, C. Grabowski, J. Beach, D. Brown, D. Gale, J. Parker, D. Ralph, W. Sommars, M.H. Frese, S.D. Frese, F. Camacho, S.K. Coffey, J.D. Letterio, T.P. Intrator, G.A. Wurden, S.C. Hsu, P. Sieck, P.J. Turchi, W.J. Waganaar, R.E. Siemon, T.J. Awe, B.S. Bauer, A.G. Lynn, and N.F. Roderick, 'Experiments on Field Reversed Configuration (FRC) Formation and Their Compression Using Liners', Poster IP2C-30, presented at the 36th IEEE International Conference on Plasma Science, San Diego, California, May 31 – June 5, 2009.

17th IEEE International Pulsed Power Conference
Washington, DC, June 28 – July 2, 2009

27. I.R. Lindemuth, R.E. Siemon, B.S. Bauer, M.A. Angelova, W.L. Atchison, S.F. Garanin, and V. Makhin, 'Numerical Simulation of Metallic Surface Plasma Formation by Megagauss Magnetic Fields,' **Invited Talk** (O8-1) at the 17th IEEE International Pulsed Power Conference, Washington, DC, June 28 – July 2, 2009.

28. S.F. Garanin, S.D. Kuznetsov, W.L. Atchison, R.E. Reinovsky, T.J. Awe, B.S. Bauer, S. Fuelling, I.R. Lindemuth, and R.E. Siemon, 'Numerical Simulations of Thick Aluminum Wire Behavior under Megaampere Current Drive,' presented (oral O4-3) at the 17th IEEE International Pulsed Power Conference, Washington, DC, June 28 – July 2, 2009.

2nd Workshop on the UNR Megagauss Experiment
Albuquerque, New Mexico, September 28-30, 2009

29. B.S. Bauer, T.J. Awe, S. Fuelling, T.S. Goodrich, and R.E. Siemon, 'Thermal ionization by pulsed megagauss field: Overview of the experiment,' presented (oral) at 2nd Workshop on the UNR Megagauss Experiment, Albuquerque, New Mexico, September 28-30, 2009.
30. T.J. Awe, B.S. Bauer, S. Fuelling, R.E. Siemon, B. Le Galloudec, 'Surface Temperature and Radial Expansion Measurements of Thick Aluminum Rods Pulsed with Multi-Megagauss Magnetic Field,' presented (oral) at 2nd Workshop on the UNR Megagauss Experiment, Albuquerque, New Mexico, September 28-30, 2009.
31. S. Fuelling, T.J. Awe, B.S. Bauer, T.S. Goodrich, and R.E. Siemon, 'Study of EUV light emission from plasma formation of aluminum rods subjected to MA currents and MG fields by time-resolved EUV spectroscopy,' presented (oral) at 2nd Workshop on the UNR Megagauss Experiment, Albuquerque, New Mexico, September 28-30, 2009.
32. T.S. Goodrich, R.E. Siemon, 'Is spectrum a blackbody?' presented (oral) at 2nd Workshop on the UNR Megagauss Experiment, Albuquerque, New Mexico, September 28-30, 2009.
33. I.R. Lindemuth, 'Modeling the UNR Megagauss Experiment: Some Preliminary MHD and Computational Considerations,' presented (oral) at 2nd Workshop on the UNR Megagauss Experiment, Albuquerque, New Mexico, September 28-30, 2009.
34. I.R. Lindemuth, 'MHRDRing the Zebra Experiment with Eulerian Computations,' presented (oral) at 2nd Workshop on the UNR Megagauss Experiment, Albuquerque, New Mexico, September 28-30, 2009.
35. M.A. Angelova, V. Makhin, B.S. Bauer, I.R. Lindemuth and R.E. Siemon, 'Numerical study of plasma formation from aluminum rods driven by megaampere currents,' presented (oral) at 2nd Workshop on the UNR Megagauss Experiment, Albuquerque, New Mexico, September 28-30, 2009.
36. R.E. Siemon, 'How dense is the plasma layer?' presented (oral) at 2nd Workshop on the UNR Megagauss Experiment, Albuquerque, New Mexico, September 28-30, 2009.
37. S.F. Garanin, S.D. Kuznetsov, W.L. Atchison, R.E. Reinovsky, T.J. Awe, B.S. Bauer, S. Fuelling, I.R. Lindemuth, R.E. Siemon, 'Numerical Simulations of Thick Aluminum Wire Behavior under Megaampere Current Drive,' presented (oral) at 2nd Workshop on the UNR Megagauss Experiment, Albuquerque, New Mexico, September 28-30, 2009.

51st Annual Meeting of the APS Division of Plasma Physics
Atlanta, Georgia, November 2-6, 2009

38. Thomas Awe, Bruno Bauer, Stephan Fuelling, Richard Siemon, Jaspreet Billing, Tasha Goodrich, 'Plasma Formation and Evolution from Thick Metal Pulsed with Megagauss Magnetic Field,' presented (poster) at 51st Annual Meeting of the APS Division of Plasma Physics, Atlanta, Georgia, Nov 2-6, 2009.

39. Tasha Goodrich, Thomas Awe, Stephan Fuelling, Richard Siemon, 'Time resolved visible spectroscopy of surface plasma radiation,' presented (poster) at 51st Annual Meeting of the APS Division of Plasma Physics, Atlanta, Georgia, Nov 2-6, 2009.

40. T. Intrator, G.A. Wurden, P.E. Sieck, W.J. Waganaar, R. Oberto, T.D. Olson, D. Sutherland, J.H. Degnan, E.L. Ruden, M. Domonkos, P. Adamson, C. Grabowski, D.G. Gale, W. Sommars, M. Kostora, M.H. Frese, S.D. Frese, J.F. Camacho, S.K. Coffey, N.F. Roderick, D.J. Amdahl, P. Parks, R.E. Siemon, T. Awe, A.G. Lynn, 'Progress on Field Reversed Configuration target for Magnetized Target Fusion,' presented (poster) at 51st Annual Meeting of the APS Division of Plasma Physics, Atlanta, Georgia, Nov 2-6, 2009.

41. J.H. Degnan, P. Adamson, D.J. Amdahl, R. Delaney, M. Domonkos, F.M. Lehr, E.L. Ruden, W. Tucker, W. White, C. Grabowski, D. Gale, M. Kostora, J. Parker, W. Sommars, M.H. Frese, S.D. Frese, J.F. Camacho, S.K. Coffey, V. Makhin, T.F. Intrator, G.A. Wurden, P.J. Turchi, R.E. Siemon, A.G. Lynn, N.F. Roderick, 'Field Reversed Configuration (FRC) formation and compression using liners,' presented (poster) at 51st Annual Meeting of the APS Division of Plasma Physics, Atlanta, Georgia, Nov 2-6, 2009.

PLX Kickoff Meeting at 51st Annual Meeting of the APS Division of Plasma Physics
Atlanta, Georgia, Nov. 6, 2009

42. B.S. Bauer, T.J. Awe, S. Fuelling, T.S. Goodrich, R.E. Siemon, 'Extreme Ultraviolet and Other Diagnostics for the LANL Plasma Liner Experiment,' presented (oral) at PLX Kickoff Meeting at 51st Annual Meeting of the APS Division of Plasma Physics, Atlanta, GA, November 6, 2009.

University of Nevada, Reno Physics Colloquium
Reno, Nevada, Nov 13, 2009

43. I.R. Lindemuth, 'An Introduction to Fusion Energy: The Fundamental Parameter Space of Controlled Thermonuclear Fusion,' Colloquium presented to the Department of Physics, University of Nevada, Reno, Reno, Nevada, Nov 13, 2009.

Innovative Confinement Concepts 2010 Workshop
Princeton, NJ, February 16-19, 2010

44. B.S. Bauer, T.J. Awe, M.A. Angelova, J. Billing, S. Fuelling, T.S. Goodrich, I.R. Lindemuth, R.E. Siemon, V. Makhin, W.L. Atchison, and S.F. Garanin, 'Aluminum plasma formation and evolution as expected from magneto-inertial fusion surfaces pulsed by multi-megagauss field,' **Invited Talk** at Innovative Confinement Concepts 2010 (ICC2010) Workshop Princeton, New Jersey, February 16, 2010.

International Conference on Plasma Diagnostics
Pont-à-Mousson, France, April 12-16, 2010

45. M. Gilmore, E. Merritt, A.G. Lynn, B.S. Bauer, S. Fuelling, R.E. Siemon, S.C. Hsu, F.D. Witherspoon, S. Brockington, A. Case, S.J. Messer, J.T. Cassibry, and the PLX Team, 'Diagnostics for the Plasma Liner Experiment (PLX),' presented (poster) at the International Conference on Plasma Diagnostics, Pont-à-Mousson, France, April 12-16, 2010.

37th IEEE International Conference on Plasma Science (ICOPS)
June 20-24, 2010, Norfolk, VA, USA

46. T.P. Intrator, G.A. Wurden, W.J. Waganaar, P.E. Sieck, J.H. Degnan, E.L. Ruden, M. Domonkos, C. Grabowski, D.G. Gale, M. Kostora, W. Sommars, M.H. Frese, S.D. Frese, J.F. Camacho, S.K. Coffey, N.F. Roderick, D.J. Amdahl, P. Parks, R.E. Siemon, T. Awe, A.G. Lynn, 'Field Reversed Configuration Target Status for Magnetized Target Fusion,' presented (oral) at the 37th IEEE International Conference on Plasma Science, Norfolk, Virginia, June 20-24, 2010.
47. J.H. Degnan, P. Adamson, D.J. Amdahl, R. Delaney, M. Domonkos, F.M. Lehr, E.L. Ruden, W. Tucker, W.M. White, H.R. Wood, T.C. Grabowski, D. Gale, M. Kostora, J. Parker, W. Sommars, M.H. Frese, S.D. Frese, J.F. Camacho, S.K. Coffey, V. Makhin, N.F. Roderick, T.P. Intrator, G.A. Wurden, P.J. Turchi, W.J. Waganaar, R.E. Siemon, T.J. Awe, B.S. Bauer, S. Fuelling, A.G. Lynn, 'Field Reversed Configuration (FRC) Formation, Translation and Compression,' presented (poster) at the 37th IEEE International Conference on Plasma Science, Norfolk, Virginia, June 20-24, 2010.

DOE-NNSA Nevada Terawatt Facility Annual Review
October 26-27, 2010, Reno, Nevada

48. K.C. Yates, 'Two Year Graduate Experience at NTF,' presented (oral) at DOE-NNSA Nevada Terawatt Facility Annual Review, Reno, Nevada, October 26, 2010.
49. B.S. Bauer, M.A. Angelova, S. Fuelling, I.R. Lindemuth, R.E. Siemon, K.C. Yates, S.F. Garanin, W.L. Atchison, T.J. Awe, and V. Makhin, 'Thermal Plasma Formation and Evolution from a Pulsed Megagauss Field,' presented (poster) at DOE-NNSA Nevada Terawatt Facility Annual Review, Reno, Nevada, October 26, 2010.

52nd Annual Meeting of the APS Division of Plasma Physics
November 8-12, 2010, Chicago, Illinois

50. T.J. Awe, 'Magnetic field threshold for thermal plasma formation from an aluminum surface pulsed to multi-megagauss magnetic field,' **Invited Talk** at 52nd Annual Meeting of the APS Division of Plasma Physics, Chicago, Illinois, Nov 8-12, 2010.

51. B.S. Bauer, M.A. Angelova, S. Fuelling, I.R. Lindemuth, R.E. Siemon, W.L. Atchison, T.J. Awe, S.F. Garanin, S.D. Kuznetsov, 'Numerical Modeling of Plasma Formation and Evolution from Thick Aluminum Pulsed with Multi-Megagauss Magnetic Field,' presented (poster) at 52nd Annual Meeting of the APS Division of Plasma Physics, Chicago, Illinois, Nov 8-12, 2010.

52. S. Fuelling, T.J. Awe, B.S. Bauer, I.R. Lindemuth, R.E. Siemon, and K.C. Yates, 'Plasma Temperature Estimates from EUV Spectroscopy of an Aluminum Rod pulsed with MA Current,' presented (poster) at 52nd Annual Meeting of the APS Division of Plasma Physics, Chicago, Illinois, Nov 8-12, 2010.

53. R.E. Siemon, T.S. Goodrich, B.S. Bauer, S. Fuelling, I.R. Lindemuth, T.J. Awe, 'Measurements and Computations of the Visible Light Spectrum Emitted from the Ionized Surface of Ohmically Heated Aluminum Rods,' presented (poster) at 52nd Annual Meeting of the APS Division of Plasma Physics, Chicago, Illinois, Nov 8-12, 2010.

54. T.P. Intrator, J. Sears, P.J. Turchi, W.J. Waganaar, T. Weber, G.A. Wurden, J.H. Degnan, M. Domonkos, C. Grabowski, E.L. Ruden, W. White, D. Gale, M. Kostora, J. Parker (SAIC); M.H. Frese, S.D. Frese, J.F. Camacho, S.K. Coffey, V. Makhin, R.E. Siemon, S. Fuelling, B.S. Bauer, A.G. Lynn, N.F. Roderick, 'Magnetized Target Fusion Integrated Engineering Test Shot,' presented (poster) at 52nd Annual Meeting of the APS Division of Plasma Physics, Chicago, Illinois, Nov 8-12, 2010.

55. J.H. Degnan, R. Delaney, Domonkos, C. Grabowski, F.M. Lehr, P. Robinson, E.L. Ruden, W. White, H. Wood, D. Gale, M. Kostora, W. Sommars, M.H. Frese, S.D. Frese, J.F. Camacho, S.K. Coffey, V. Makhin, T.P. Intrator, G.A. Wurden, J. Sears, P.J. Turchi, R.E. Siemon, S. Fuelling, B.S. Bauer, A.G. Lynn, ' Field Reversed Configuration (FRC) injection and compression experiments,' presented (poster) at 52nd Annual Meeting of the APS Division of Plasma Physics, Chicago, Illinois, Nov 8-12, 2010.

56. E. Merritt, M. Gilmore, A.G. Lynn, B.S. Bauer, F.D. Witherspoon, J. Cassibry, S. Hsu, 'Diagnostics for the Plasma Liner Experiment (PLX),' presented (poster) at 52nd Annual Meeting of the APS Division of Plasma Physics, Chicago, Illinois, Nov 8-12, 2010.

57. C. Grabowski, J.H. Degnan, R. Delaney, M. Domonkos, F.M. Lehr, P.R. Robinson, E.L. Ruden, W. White, H. Wood, D. Brown, D. Gale, M. Kostora, J. McCullough, W. Sommars, M.H. Frese, S.D. Frese, J.F. Camacho, S.K. Coffey, V. Makhin, T.P. Intrator, G.A. Wurden, P.J. Turchi, R.E. Siemon, S. Fuelling, A.G. Lynn, 'FRC Formation, Translation and Capture Studies for the Field Reversed Configuration Heating Experiment (FRCHX) ,' presented (poster) at 52nd Annual Meeting of the APS Division of Plasma Physics, Chicago, Illinois, Nov 8-12, 2010.

PLX Satellite Meeting at 52nd Annual Meeting of APS Division of Plasma Physics
November 12, 2010, Chicago, Illinois

58. S. Fuelling and B.S. Bauer, 'Radiation Diagnostics for PLX,' presented (oral) at the PLX Satellite Meeting at 52nd Annual Meeting of the APS Division of Plasma Physics, Chicago, Illinois, Nov 12, 2010.

Annual Meeting of the Fusion Power Associates
December 1-2, 2010, Washington, DC

59. I.R. Lindemuth, 'The fusion parameter space from first principles,' **Invited Talk** at the Annual Meeting of the Fusion Power Associates, Washington, DC, Dec 1-2, 2010.

8th International Conference on Dense Z-pinches,
June 5 – 9, 2011, Biarritz, France

60. B.S. Bauer, S. Fuelling, I.R. Lindemuth, R.E. Siemon, T.J. Awe, W.L. Atchison, S.F. Garanin, and S.D. Kuznetsov, 'Thermal Plasma Formation and Evolution from Thick Aluminum Pulsed by Multi-Megagauss Magnetic Field,' presented (oral) at the 8th Int'l Conference on Dense Z-pinches, Biarritz, France, June 5-9, 2011.
61. Stephan Fuelling, Thomas J. Awe, Bruno S. Bauer, Irvin R. Lindemuth, Richard E. Siemon, 'Rapid Rise and Saturation of Upper Temperatures of Al Wall Plasma Generated by Pulsed MG Field,' presented (poster) at the 8th Int'l Conference on Dense Z-pinches, Biarritz, France, June 5-9, 2011.

LULI Colloquium, Ecole Polytechnique
June 16, 2011, Paris, France

62. B.S. Bauer, Oral Presentation in French, 'Fusion magnéto-inertielle: problématique de la paroi métallique,' Ecole Polytechnique LULI seminar, Paris, France, June 16, 2011.

18th IEEE International Pulsed Power Conference
June 19-23, 2011, Chicago, Illinois

63. C. Grabowski, J.H. Degnan, D.J. Amdahl, R. Delaney, M. Domonkos, F.M. Lehr, R. Magallanes, P.R. Robinson, E.L. Ruden, W. White, H. Wood, D. Gale, M. Kostora, J. McCullough, W. Sommars, M.H. Frese, S.D. Frese, J.F. Camacho, S.K. Coffey, V. Makhin, T.P. Intrator, G.A. Wurden, J. Sears, P.J. Turchi, W.J. Waganaar, T. Weber, R.E. Siemon, S. Fuelling, B.S. Bauer, A.G. Lynn, and N.F. Roderick, 'FRC lifetime studies for the field reversed configuration heating experiment (FRCHX),' presented (poster 1P-69) at the 18th IEEE Int'l Pulsed Power Conference, Chicago, IL, June 19-23, 2011.

37th IEEE International Conference on Plasma Science (ICOPS)
June 26-30, 2011, Chicago, Illinois

64. I.R. Lindemuth, R.E. Siemon, B.S. Bauer, and W.L. Atchison, 'Computational Aspects of Simulating Megagauss-Magnetic-Field-Induced Plasma Formation on Thick-Wire Metallic Surfaces,' presented (poster IP3M-37) at the 38th IEEE Int'l Conference on Plasma Science, Chicago, Illinois, June 26-30, 2011.
65. T.C. Grabowski, J.H. Degnan, D.J. Amdahl, R.K. Delaney, M.T. Domonkos, F.M. Lehr, R. Magallanes, P.R. Robinson, E.L. Ruden, W.M. White, H.R. Wood, D.G. Gale, M.R. Kostora, J.L. McCullough, W.E. Sommars, M.H. Frese, S.D. Frese, J.F. Camacho, S.K.

Coffey, T.P. Intrator, G.A. Wurden, J. Sears, P. J. Turchi, W.J. Waganaar, T. Weber, R.E. Siemon, S. Fuelling, B.S. Bauer, A.G. Lynn, and N.F. Roderick, 'FRC Lifetime Studies for the Field Reversed Configuration Heating Experiment,' presented (poster IP1B-14) at the 38th IEEE Int'l Conference on Plasma Science, Chicago, Illinois, June 26-30, 2011.

24th Symposium on Fusion Engineering
June 26-30, 2011, Chicago, Illinois

66. T.P. Intrator, C. Adams, T. Awe, S.C. Hsu, J. Dunn, J. Sears, W. Waganaar, T. Weber, G.A. Wurden, J.H. Degnan, M. Domonkos, C. Grabowski, E.L. Ruden, W. White, D.G. Gale, M. Kostora, W. Sommars, D.J. Amdahl, J.F. Camacho, S.K. Coffey, M.H. Frese, S.D. Frese, N.F. Roderick, B.S. Bauer, S. Fuelling, R.E. Siemon, R. Clark, M. Gilmore, and A. Lynn, 'Magnetized Target Fusion: Potential Path from Science to Practical Fusion Energy,' **Invited Talk** (SO2B-3) at the 24th Symposium on Fusion Engineering, Chicago, Illinois, June 26-30, 2011.
67. I.R. Lindemuth and R.E. Siemon, 'Fusion 101 – The Fusion Parameter Space from First Principles,' presented (oral SO4A-5) at the 24th Symposium on Fusion Engineering, Chicago, Illinois, June 26-30, 2011.
68. I.R. Lindemuth, 'Magnetized Target Fusion (MTF) (a.k.a. Magneto- Inertial Fusion): Can an unexplored, low-cost pathway accelerate the development of fusion power?,' presented (oral discussion) at the SOFE Town Hall Meeting on Accelerating the Development of Fusion Power, at the 24th Symposium on Fusion Engineering, Chicago, Illinois, June 27, 2011.

53rd Annual Meeting of the APS Division of Plasma Physics,
November 14-18, 2011, Salt Lake City, Utah

69. B.S. Bauer, S. Fuelling, I.R. Lindemuth, R.E. Siemon, K.C. Yates, W.L. Atchison, T.J. Awe, S.F. Garanin, S.D. Kuznetsov, 'Evolution of Thermal Plasma Formed from Thick Aluminum Pulsed with Multi-MG Magnetic Field,' presented (oral) at the 53rd Annual Meeting of the APS Division of Plasma Physics, Salt Lake City, Utah, November 14-18, 2011.
70. Stephan Fuelling, Thomas J. Awe, Bruno S. Bauer, Irvin R. Lindemuth, Richard E. Siemon, 'Fast Temperature Rise and Saturation of Al Surface Plasma Generated by Pulsed MG Fields,' presented (poster) at the 53rd Annual Meeting of the APS Division of Plasma Physics, Salt Lake City, Utah, November 14-18, 2011.
71. Chris Grabowski, James Degnan, David Amdahl, Rachel Delaney, Matthew Domonkos, Mark Lehr, Ricardo Magallanes, Randy Robinson, Edward Ruden, William White, Don Gale, Mark Kostora, John Mccullough, Wayne Sommars, Michael Frese, Sherry Frese, Frank Camacho, Sean Coffey, Thomas Intrator, Glen Wurden, Richard Siemon, Stephan Fuelling, Bruno Bauer, Alan Lynn, Norman Roderick, 'FRC Lifetime Studies for the Field Reversed Configuration Heating Experiment', presented (poster) at the 53rd Annual Meeting of the APS Division of Plasma Physics, Salt Lake City, Utah, November 14-18, 2011.

72. J.A. Schwartz, T.J. Awe, S.C. Hsu, E.C. Merritt, A.G. Lynn, M.A. Gilmore, S. Fuelling, 'Visible Spectroscopy on the Plasma Liner Experiment (PLX),' presented (poster) at the 53rd Annual Meeting of the APS Division of Plasma Physics, Salt Lake City, Utah, November 14-18, 2011.

Physics Colloquium, University of Nevada, Reno
December 9, 2011, Reno, Nevada

73. B.S. Bauer, Oral Presentation, 'Plasma Formation and Evolution from Metal Pulsed by Multi-Megagauss Magnetic Field,' University of Nevada, Reno Physics Colloquium, Reno, Nevada, December 9, 2011.

Center for Nonlinear Studies Colloquium, Los Alamos National Laboratory
June 20, 2012, Los Alamos, New Mexico

74. B.S. Bauer, Colloquium, 'Derivation of Plasma Fluid Equations,' (part of the LANL Plasma Physics Summer School), Center for Nonlinear Studies, Los Alamos National Laboratory, Los Alamos, New Mexico, June 20, 2012.

24th Fusion Energy Conference of the International Atomic Energy Agency (IAEA),
October 8 – 13, 2012, San Diego, California

75. J.H. Degnan, D.J. Amdahl, M. Domonkos, C. Grabowski, E.L. Ruden, W.M. White, T.P. Intrator, G.A. Wurden, J. Sears, W.J. Waganaar, M.H. Frese, S.D. Frese, J.F. Camacho, S.K. Coffey, V. Makhin, N.F. Roderick, D.G. Gale, M. Kostora, W. Sommars, G.F. Kiuttu, B.S. Bauer, S. Fuelling, and A.G. Lynn, 'Recent Magneto-Inertial Fusion Experiments on FRCHX,' presented (poster P6-02) at the 24th Fusion Energy Conference of the International Atomic Energy Agency (IAEA), San Diego, California, October 8 – 13, 2012.

14th Int'l Conference on Megagauss Magnetic Field Generation and Related Topics,
October 14 – 19, 2012, Maui, Hawaii

76. I.R. Lindemuth, R.E. Siemon, B.S. Bauer, and W.L. Atchison, 'Verification and Validation Adventures in Simulating Megagauss-Magnetic-Field-Induced Plasma Formation on Thickwire Metallic Surfaces,' **Invited Talk** at the 14th Int'l Conference on Megagauss Magnetic Field Generation and Related Topics, Maui, Hawaii, October 14 – 19, 2012.

77. J.H. Degnan, D.J. Amdahl, M. Domonkos, C. Grabowski, E.L. Ruden, W.M. White, T.P. Intrator, G.A. Wurden, J. Sears, T. Weber, W.J. Waganaar, M.H. Frese, S.D. Frese, J.F. Camacho, S.K. Coffey, V. Makhin, N.F. Roderick, D.G. Gale, M. Kostora, A. Lerma, C. Roth, W. Sommars, G.F. Kiuttu, B.S. Bauer, S. Fuelling, and A.G. Lynn, 'Flux and Magnetized Plasma Compression Driven by Shiva Star,' **Invited Talk** at the 14th Int'l Conference on Megagauss Magnetic Field Generation and Related Topics, Maui, Hawaii, October 14 – 19, 2012.

3 Photodiode Array Temperature Calibration

For an opaque emitter at high temperature, the emission intensity in the long wavelength tail of the Planck distribution approximately follows the Rayleigh-Jeans law. To observe the transition in time from bremsstrahlung radiation to blackbody radiation, we employed a compact spectrometer, the Model CP-140 from Jobin Yvon, equipped with a 32-element photodiode array to continuously measure the spectral emission in the visible. We also imaged the barbell load through an optical port on Zebra through a green, Wratten #58 filter onto a second 32-element photodiode array to continuously monitor the emission intensity from the surface of the narrowed region (0.5 mm – 2.0 mm diameter) of the barbell load. The upper half of the photodiode array also passes through a neutral density filter, in order to attenuate the light for the recording of the late-time emissions of the barbell load.

The filtered emissions from the barbell loads had been analyzed using the spectral transmission curve for the Wratten filter from the supplier's website. However, we have discovered that the spectral transmission curve for the Wratten #58 filter from the supplier's website was incomplete. It only provided the response curve and filter data up to 700 nm. We subsequently found a response curve on the Internet that showed the filter response in the near infrared (NIR) and were surprised to see that the filter did not block NIR but was highly transparent in that region! We subsequently purchased the 'Kodak Handbook of Photographic Filters', which showed the Wratten #58 filter response in great detail.

Comparing the response curve from the vendor (Figure 1, right) with the one from the Kodak handbook (Figure 1, left), we saw that our previous calculations gave a lower bound for temperature that was too high. We have therefore reevaluated our photodiode array data and performed corrections to our older temperature estimates.

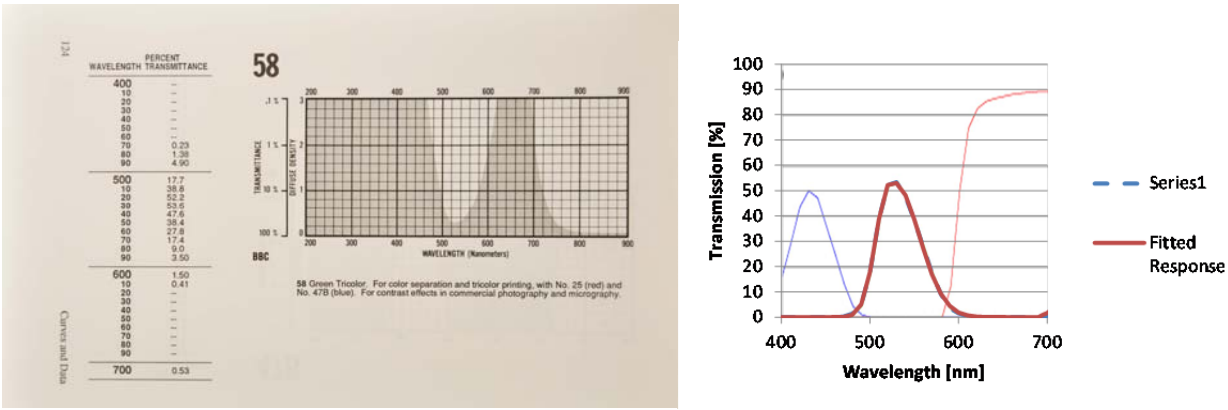

Figure 1. Wratten #58 filter response, from 'Kodak Handbook of Photographic Filters', on the left and the response curve from the supplier, on the right. One can see that the filter becomes completely transparent for wavelengths above 800 nm.

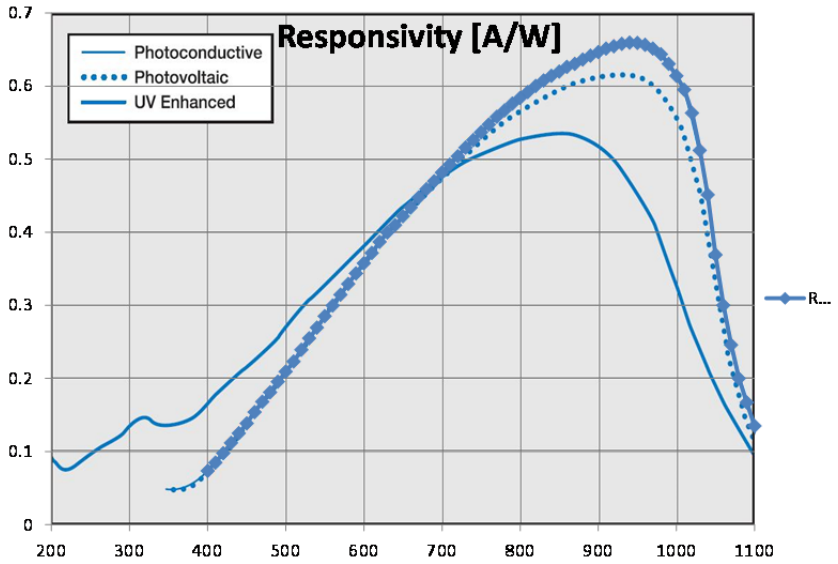

Figure 2. Spectral response of the photodiode array elements.

From Figure 2, the 32-element photodiode array is much more sensitive in the NIR than at 525 nm, where the green light passes through the Wratten #58 filter. In addition, the Wratten #58 filter is narrow at the green bandpass and less transparent (~50%) than in the NIR.

Furthermore, the neutral density filter that was used on half of the array elements has a higher transmission in the NIR than at 525 nm (Figure 3). The combination of the photodiode response with the response curves of the Wratten #58 and the neutral density filter led to a significantly higher contribution from the emissions in the NIR than from the narrow green bandpass to the signal of the photodiode array.

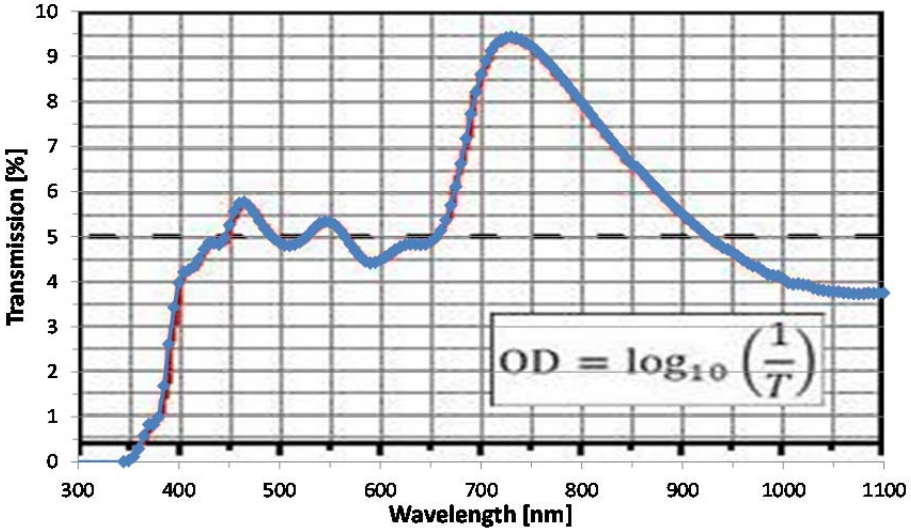

Figure 3. Transmission graph of the Newport ND 1.3 filter. The filter is not flat and has a higher transmission in the NIR than at 525 nm.

3.1 Rayleigh-Jeans Law

For high surface temperatures, it is interesting to use the approximation that the NIR–optical emissions from the barbell load follow the Rayleigh-Jeans law. Then, we can analytically calculate the surface temperature of the barbell load. In the long wavelength limit, the Planck distribution (per steradian) can be approximated by a using Taylor expansion of the exponential function:

$$\exp\left[\frac{h\nu}{kT}\right] \cong 1 + \frac{h\nu}{kT}, \text{ for } kT \gg h\nu$$

Therefore:

$$\frac{dL_B}{dE} = \frac{2E^3}{c^2h^3}\frac{1}{\exp\left[\frac{E}{kT}\right]-1} \cong \frac{2kTE^2}{c^2h^3}, \text{ units: } \left[\frac{\text{W}}{\text{J m}^2\text{sr}}\right]$$

In PrismSPECT the units are [erg/cm^2/sr/s/eV]. We can express the Rayleigh-Jeans law in terms of frequency ν and wavelength λ:

$$\frac{dL_B}{d\nu} = \frac{2kT\nu^2}{c^2}, \text{ units: } \left[\frac{\text{W}}{\text{1/s m}^2\text{sr}}\right]$$

Since $\lambda\nu = c$ and $|d\nu| = c\left|\frac{d\lambda}{\lambda^2}\right|$:

$$\frac{dL_B}{d\lambda} = \frac{2ckT}{\lambda^4}, \text{ units: } \left[\frac{\text{W}}{\text{m m}^2\text{sr}}\right]$$

The amplitude from the filtered photodiode array should be proportional to the temperature of the barbell surface. We want to express the Rayleigh-Jeans law in terms of photon flux. Each photon carries the quantum of energy $E = h\nu = hc/\lambda$. We multiply by the detector area A and solid angle Ω to obtain the photon flux per unit energy, frequency, or wavelength. Therefore, the photon flux for the three forms of the Rayleigh-Jeans law are:

$$n_E = \frac{1}{E}\frac{dL_B}{dE}A\Omega = \frac{2kT}{c^2h^3}A\Omega E, \ \left[\frac{1}{\text{s}}\right]\left[\frac{1}{\text{J}}\right], \text{ or in } \left[\frac{1}{\text{s}}\right]\left[\frac{1}{\text{eV}}\right](\text{x e})$$

$$n_\nu = \frac{1}{h\nu}\frac{dL_B}{d\nu}A\Omega = \frac{2kT}{c^2h}A\Omega\nu, \ \left[\frac{1}{\text{s}}\right]\left[\frac{1}{\text{1/s}}\right]$$

$$n_\lambda = \frac{\lambda}{hc}\frac{dL_B}{d\lambda}A\Omega = \frac{2kT}{h}A\Omega\frac{1}{\lambda^3}, \ \left[\frac{1}{\text{s}}\right]\left[\frac{1}{\text{m}}\right], \text{ or in } \left[\frac{1}{\text{s}}\right]\left[\frac{1}{\text{nm}}\right](\text{x } 10^{-9})$$

More useful in the evaluation of the detector response is the use of quantum efficiency for the detector instead of responsivity. There is a simple relationship between responsivity and quantum efficiency Q:

$$[R] = \left[\frac{\text{A}}{\text{W}}\right], R = \frac{I}{P} = \frac{Ne/\Delta t}{E/\Delta t} = Q\frac{e}{hc}\lambda = \frac{1}{1240} * Q\lambda \text{ [nm]}.$$

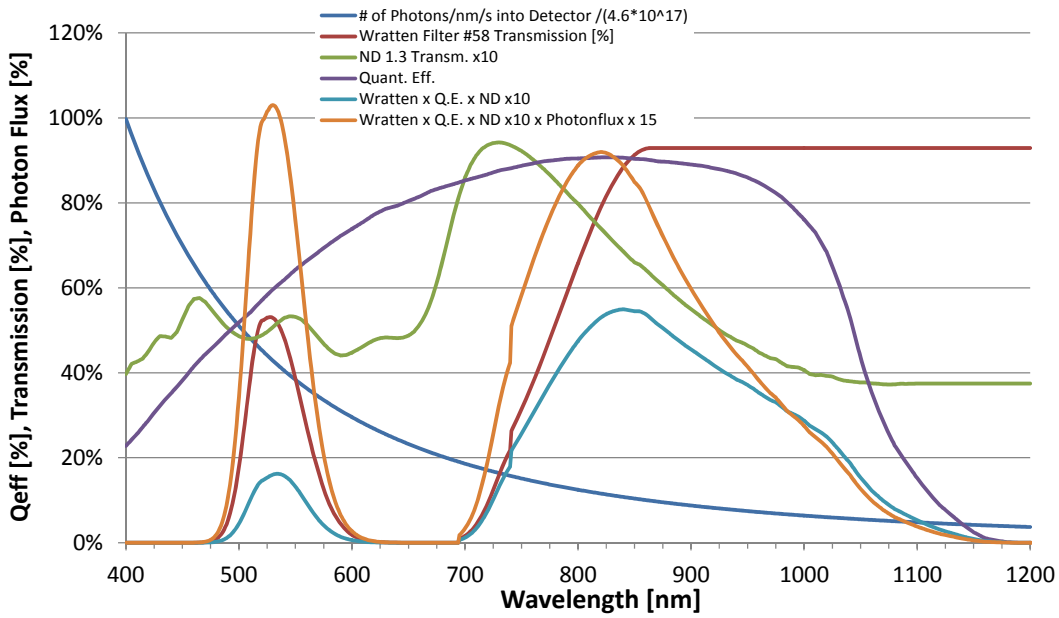

Figure 4. Plot with photon flux (T = 20 eV), Q.E., and transmission coefficients

3.2 Convolution of Planck Blackbody with filters and responsivity

To calculate the response of the photodiode array diagnostic, the Planck blackbody (BB) distribution emission intensity from the load needs to be convoluted with the transmission coefficients of the Wratten Filter and the ND 1.3 filter, and then with the photodiode responsivity data. In addition, geometrical factors need to be taken into account.

The Planck BB distribution intensity is calculated in [erg/cm^2/sr/s/eV] and the generated table values are then multiplied with the Wratten #58 filter response, the Thorlabs neutral density ND 1.3 filter response, with the responsivity of the photodiode array, with the solid angle, the effective detector area, and the energy interval in [eV]. This generates current values per wavelength interval, these are summed up and multiplied by the termination resistor 50 Ω to yield the photodiode (PD) voltage for a given plasma temperature. Tom Awe estimated an additional attenuation factor of 0.79 for various losses in the light transport.

The various contributions to the overall signal response of the photodiode array are plotted in Figure 4.

Table 3.1. Predicted photodiode signal from numerical integration for two wavelength bands, for temperature T = 20 eV. The first band, 400 nm – 650 nm, represents the 'old' Wratten #58 filter calibration, while the second band, 650 nm -1200 nm, represents the NIR band.

	Int. 400-650 nm [V]	Int. 650-1200 nm [V]	Ratio	Total [V]
by Energy:	1.143	3.634	3.180	4.776
by Wavelength:	1.145	3.638	3.178	4.783
w/o R-J approx.:	1.078	3.503	3.251	4.581

Table 3.1 gives the results of the numerical integration for $T = 20$ eV of the convolution of the blackbody emission with the various filter and photodiode responses for the wavelength band of the old Wratten filter #58 response curve and the NIR band. The ratio between the two wavelength bands is also given. The contributions of the NIR band are a factor 3 higher than those from the visible wavelength band. The total predicted voltage is given in the last column. The numerical integration has been performed for the Rayleigh-Jeans law expressed both by the photon flux per energy and by the photon flux per wavelength interval; the two numerical integrations are equal to within 1%. Then we also performed the numerical integration using the Planck distribution and the numerical integration is only about 4% less, meaning that the Rayleigh-Jeans law is a good approximation in our case, at $T = 20$ eV.

Looking at the attenuated curves (with ND1.3) in Figure 5, we see that the previous estimates of the lower bound of the temperature were too high, typically by a factor of 3. Following the black dashed arrows in this example, a PD signal of 1.5 V would give a 6 eV plasma temperature on the red curve (Wratten #58 extended to 1200 nm), while the dark-blue curve gives a 22 eV plasma temperature (Wratten #58 up to 650 nm). Following the red dashed arrows, the former plasma onset temperature of 0.6 eV is now lowered to ~0.3 eV. From Figure 6, the peak temperature from extended Wratten #58 filter response is about 6 eV for MG V shot #2487.

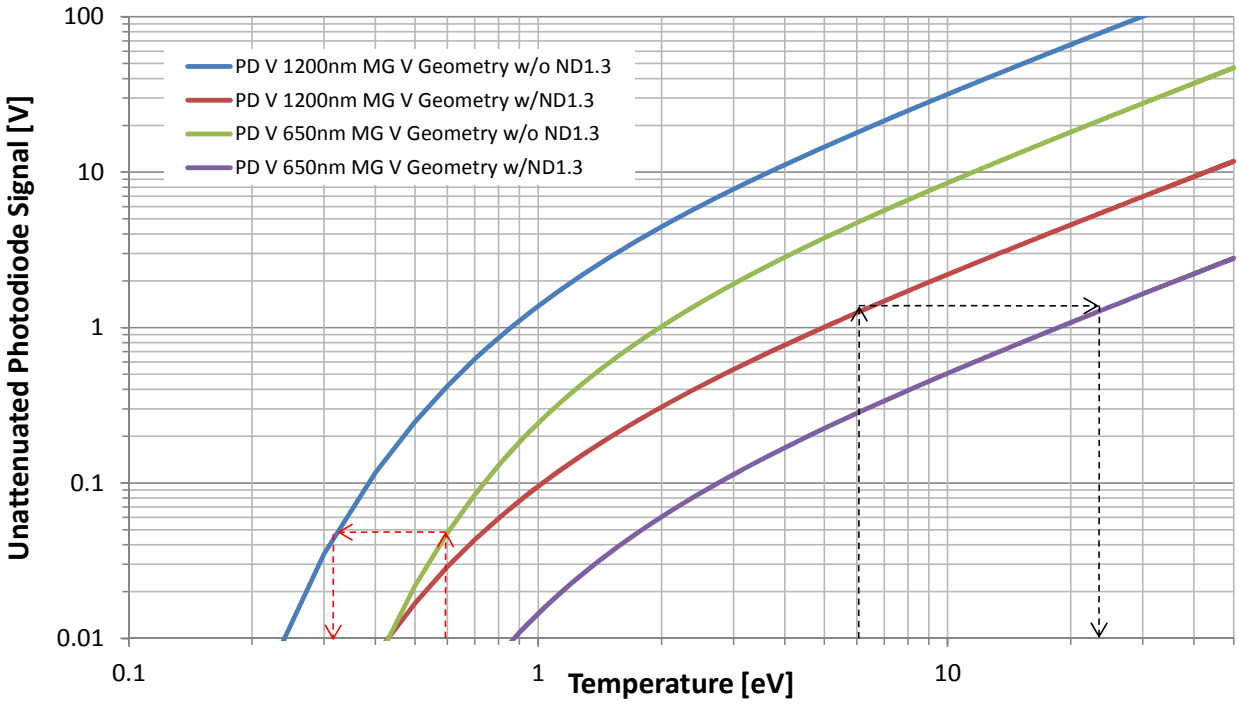

Figure 5. Temperature vs. photodiode voltage for the old and new calibrations. The green and dark-blue curves use a filter cut-off of 650 nm, while the light-blue and red curves extend to 1200 nm.

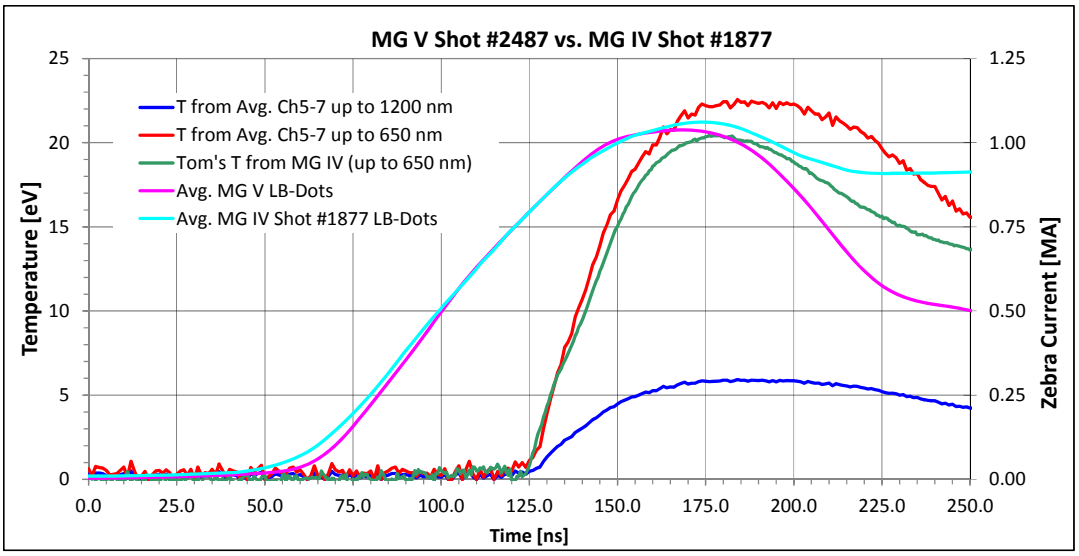

Figure 6. Comparison of the MG IV (shot# 1877) with the 'old' Wratten #58 calibration with the MG V (shot# 2487) with the new Wratten #58 calibration that is extended into the NIR.

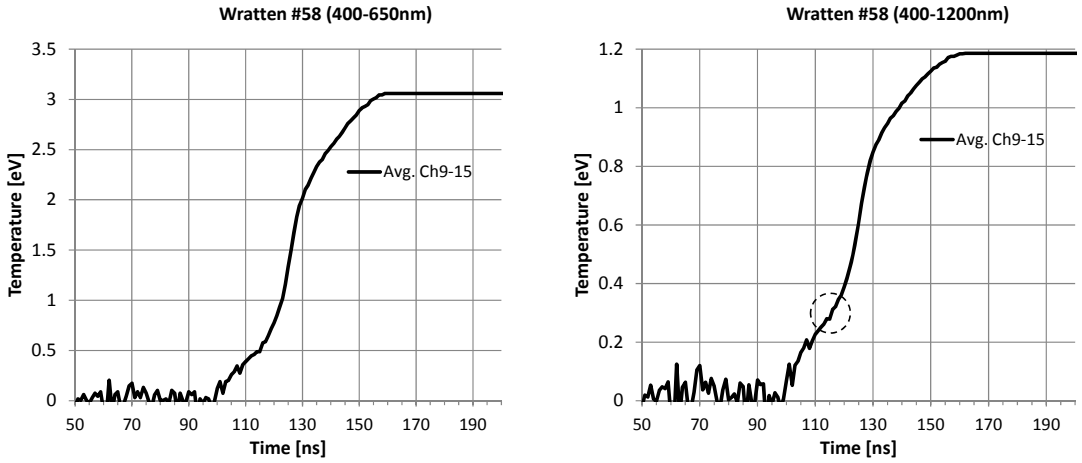

Figure 7. Comparison of the early time photodiode signal with the visible and extended Wratten #58 filter responses.

The time of plasma formation was identified by the sudden change in the slope of the photodiode signal, which does not change in the new calibration, as one can see in Figure 7. However, the temperature at which the onset of plasma formation occurred decreased from about 0.6 eV to 0.3 eV.

3.3 Zemax Ray Tracing

We performed ray tracing using Zemax to determine how the chromatic aberrations of the lens would alter the amount of infrared collected by the photodiodes. Since the image was focused onto the photodiode array in the visible, emissions from the NIR would be out of focus, therefore lessen the amount of light collected by the photodiode array in the NIR.

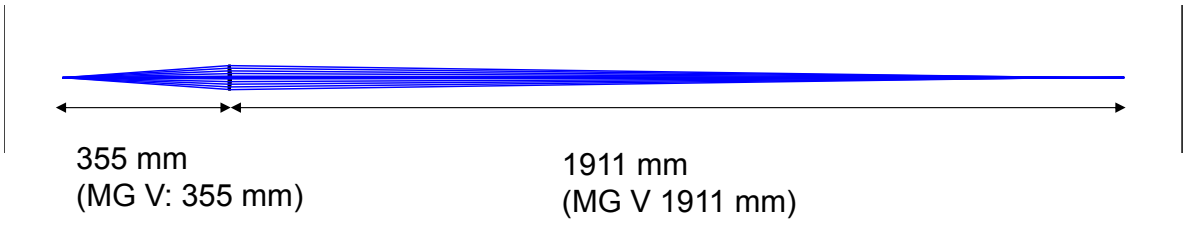

Figure 8. Imaging setup for the MG V experiment.

In the MG IV & V experiments, we used a 3" diameter, 300 mm focal length plano-convex lens (Figure 8). The radius of curvature in the modeling was varied for best focus to fit the MG V dimensions (image and object distances).

We set up Zemax to image a rectangular object that resembles the thinned region of the barbell load and performed an analysis of the imaged object at the two wavelengths (530 nm & 1000 nm) with the best focus left at 530 nm. The efficiency at 530 nm was 82.5%, since Zemax also considers reflection losses on the lens surface. The efficiency at 1000 nm dropped to 60.2%, so we lose about 27% in the NIR due to the blurred image that causes the NIR light to overspill the detector width.

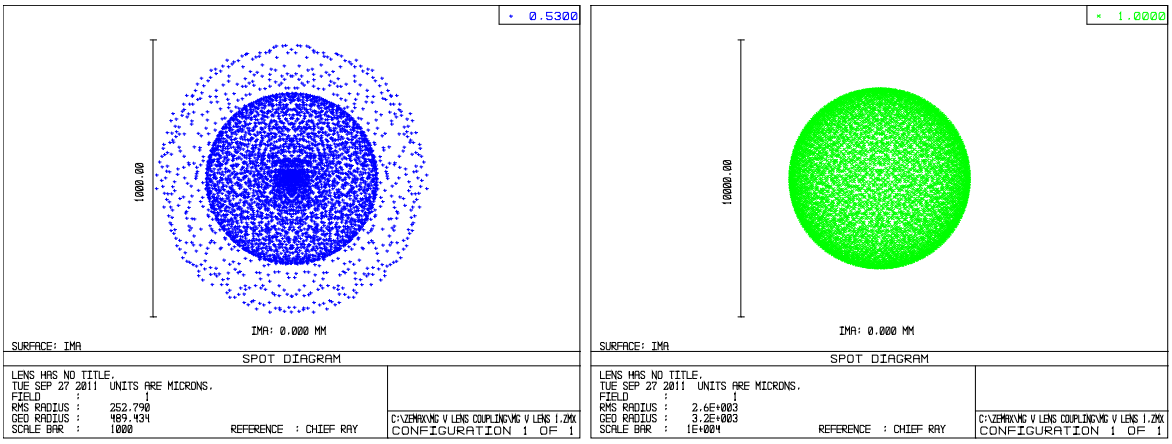

Figure 9. BK7 bi-convex lens, spot focus at 530 nm (blue) and at 1000 nm (green).

Using a bi-convex lens with the distance dimensions of MG V and optimizing for lens curvature, the RMS spot radius is 0.253 mm at 530 nm and 2.6 mm at 1000 nm.

3.4 Photodiode Array Test Performed with a Quartz Tungsten Halogen Lamp

In order to verify our findings, we purchased an Oriel quartz tungsten (QTH) halogen lamp with an output of 50 W and also bandpass filters that would block the NIR. We measured the power input of the QTH lamp to be almost exactly 50 W when driven by a 12 V constant voltage power supply.

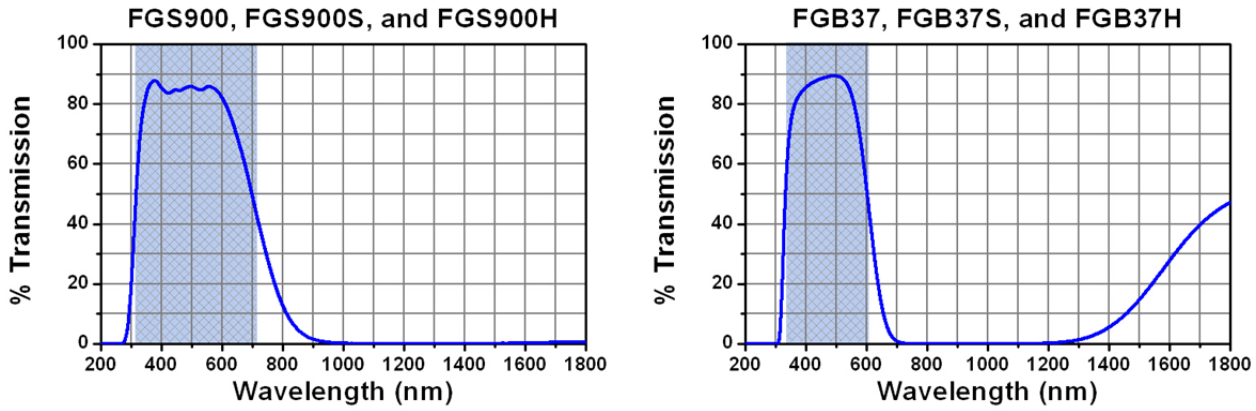

Figure 10. Filter transmission curves for two Newport glass filters.

We used two bandpass filters from Newport (Figure 10) placed in front of the photodiode array (Figure 11). We built a holder and housing for the QTH filament light bulb. We also ran a test with two razor blades separated by 1 mm placed in front of the light bulb, to mimic the 1-mm diameter barbell load. The irradiance curve of the QTH lamp and the imaged filament are given in Figure 12.

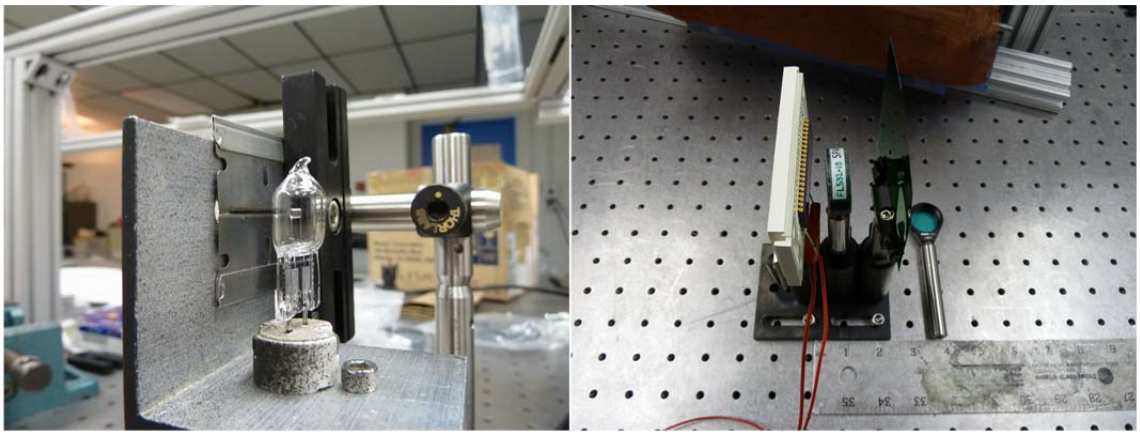

Figure 11. Test setup with QTH lamp, and photodiode array with filters.

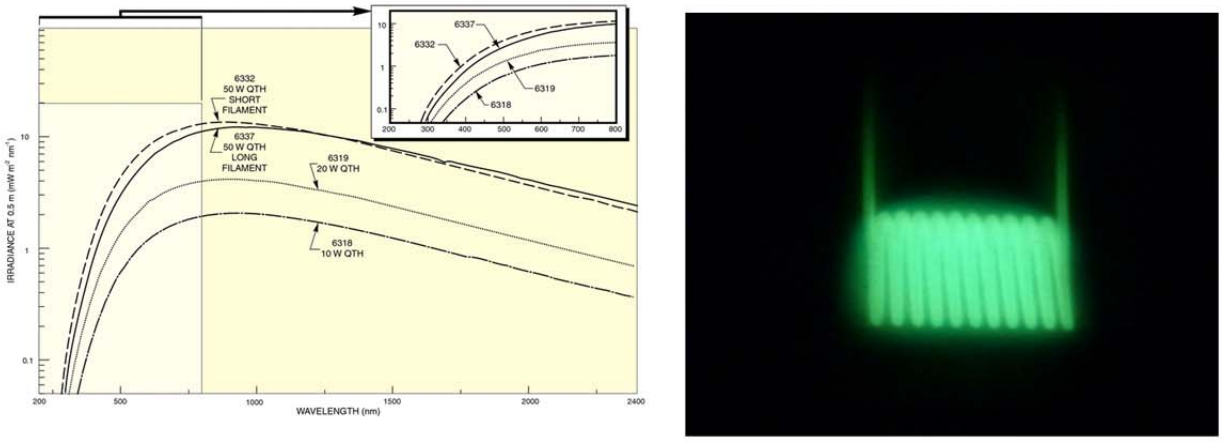

Figure 12. Irradiance curve from the QTH filament lamp (left) and green filtered image of the filament onto the photodiode array (right). Apparent is the halo around the filament image due to spherical aberrations.

The experimental results are summarized in Table 3.2 can compared to calculated photodiode currents. For the FGS900 filter, the error is relatively high (~25%), possibly due to the not well-known transition of the Wratten filter in the region between 700 nm – 800 nm, which intersects with the FGS900 filter transition (compare Figure 1 with Figure 10). However, there is good agreement with the FBG35 filter (Figure 10), the error is fairly small (<5%).

The FBG35 completely eliminates the NIR transmission of the Wratten #58 filter and since the test results are in good agreement with those predicted from the convolution of the irradiance of the QTH lamp with the filter curves and the photodiode array responsivity curve, we can have confidence in the recalibrated temperature measurement of the barbell loads.

Table 3.2. Result from the measured photodiode current (in μA) with the QTH lamp and comparison with the expected photodiode currents that were calculated using the irradiance data and filter curves.

	Theoretical		**Measurement**		
	Sum	**Ratio**	3" + GS	**Meas.Ratio**	%Error
Wratten Only	2.276	**100.00%**	480	**100.00%**	
Wr&FGS900	0.164	**7.19%**	25.65	**5.34%**	-25.66%
Wr&FGB37	0.043	**1.87%**	9.39	**1.96%**	4.66%

4 X-Ray Radiography

Although the present diagnostics provide considerable information, the great majority of the material is inaccessible to them, because it is optically thick to visible light. Even in the relatively low density plasma region, no density measurement is currently available, because the green laser interferometer beam is absorbed going through the density required to cause half a fringe shift (about 0.01% of solid density). Soft x-rays are needed to probe deeper into the expanding material and measure the density profile. X-rays from hot laser-plasmas or x-pinches[1,2,3] can be used to backlight high density plasmas. We investigated how to perform radiographs using Leopard-laser-generated x-rays and/or x-rays generated by x-pinches in the current return path of the barbell loads. A mass density and a temperature profile at peak current obtained from numerical simulations performed with the MHRDR code are shown in Figure 13.

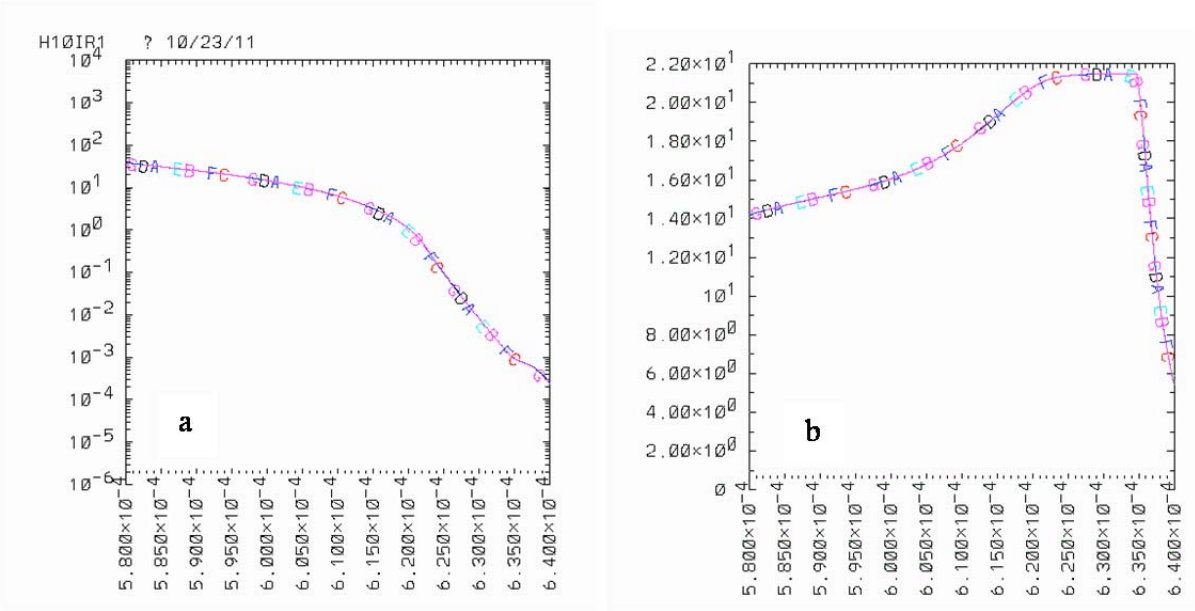

Figure 13. Aluminum load density and temperature profiles from MHRDR code simulation. Horizontal axis is the load radius (in m), vertical axis are (a) density (in kg/m^3) and (b) electron temperature (in eV). The density gradient is steep, with >3 orders of magnitude drop in density over about 20 μm. With a camera magnification of 5x, we can examine this interesting region of dense, hot plasma.

[1] S.V. Lebedev et al., 'X-ray backlighting of wire array Z-pinch implosions using X pinch,' Rev. Sci. Instrum. **72**, 671 (2001).

[2] S.A. Pikuz, T.A. Shelkovenko, V.M. Romanova, D.A. Hammer, A.Ya. Faenov, V.A. Dyakin, and T.A. Pikuz, 'High-luminosity monochromatic x-ray backlighting using an incoherent plasma source to study extremely dense plasmas,' Rev. Sci. Instrum. **68**, 740 (1997).

[3] D.H. Kalantara and D.A. Hammer, 'The x-pinch as a point source of x rays for backlighting,' Rev. Sci. Instrum. **66**, 779 (1995).

The 50-TW Leopard laser is at a stage permitting the development of x-ray radiography on Zebra. This insightful diagnostic could provide detailed measurements of the dynamics of warm, dense metal driven by multi-megagauss magnetic field. The Leopard laser can provide >10 J of 1054 nm light in a 0.3-picosecond pulse, focused to ~10 μm diameter, for an intensity on target of order 10^{19} W/cm^2. When applied to a foil target, such intensity will yield of order 10% conversion of laser energy to 100-1000 keV electrons. The energetic electrons will emit bremsstrahlung radiation and also excite ionic states, which will provide intense line radiation.

Flash x-ray radiographs of the load can be made by projection of a point source of x-rays made by the laser (Figure 14a). A few-micron-diameter pinhole will be used to limit the size of the x-ray source, as necessary (e.g., the Leopard-driven Cu L-shell x-ray spot has a diameter of 150 μm).

We have recently designed, constructed, and tested an x-ray camera that is well suited for recording flash x-ray radiographs inside the Zebra z-pinch vacuum chamber (Figure 14b). The camera holds multiple layers of x-ray film and a Storage Phosphor Screen. The recording media have a large area (38-mm exposed diameter), for a wide view of the load. The film compartment is connected to the outside via a serpentine tunnel that enables the camera to be quickly evacuated, but that lets through so few photons that the recording media are insignificantly exposed, even if the camera is left all day under bright fluorescent lights.

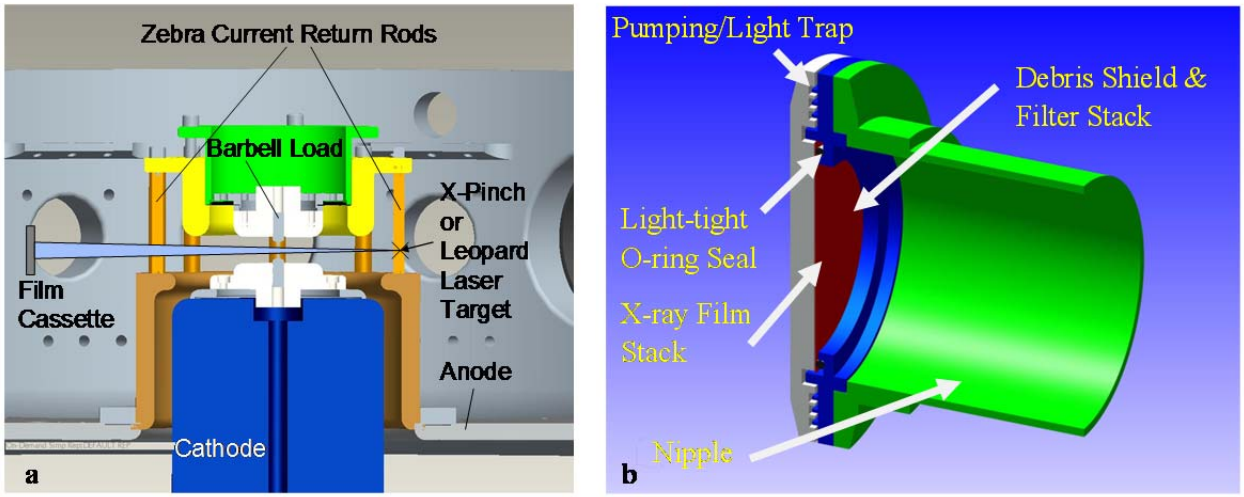

Figure 14. (a) Schematic of caged load configuration, with x-pinch or laser target placed at the current return rods, for point-projection x-ray radiography of load driven by Zebra. The narrow central section of the barbell load is probed by x-rays that are recorded on Tritium (GE) or other film in shielded and filtered film cassettes. **(b)** X-ray film camera. Made partially with modified ISO-50 parts; the x-ray film stack is covered by a light-tight filter stack, composed of debris shield(s) and x-ray filter(s). The x-ray and filter stack can be pumped out from the sides through a light trap, coated with graphite. We have tested the camera on the Zebra machine and on the Leopard laser and the camera proved to be light-tight and free of virtual leaks. For additional debris protection, a plastic foil can be wrapped around the nose of the ISO-50 nipple. The assembly is held together by an ISO-50 C-clamp.

The x-ray camera holds x-ray filter(s) in front of the film, to reject radiation coming from the plasma. A variety of thin foil filters are on hand for the experiment, including about twenty 50-mm-square 12.5-μm-thick titanium foils. The x-ray filters are in contact with the film, to avoid blurring from x-ray fluorescence of the filter. The plasma will produce much softer radiation than the radiography x-ray sources (laser-driven foil and/or x-pinch), as the rod surface temperature is only a few tens of eV.

Although film is a time-integrating detector, the radiograph will only record the instantaneous image of the load at the moment the radiography x-ray source is on. For the short-pulse laser-plasma, the duration of the radiographic flash can be as short as picoseconds (although the short-pulse laser only lasts 0.3 ps, x-rays are emitted from the laser hot spot until it cools). Because the rod plasma is relatively cold, even nanosecond time-resolution is adequate to capture structure at the 10 μm scale. Such time resolution can also be achieved with x-pinches, or with the uncompressed Leopard laser pulse. These technical options provide some significant conveniences over the short-pulse laser approach, and their availability makes the likelihood of success for obtaining x-ray radiographs very high.

The x-ray camera also holds debris shielding, consisting of multiple separated layers of polyethylene and aluminum foil. Tests of the camera close to the exploding rod have shown that such debris shielding layers are needed to stop "bullets" of rod metal from penetrating the x-ray filters, creating small apertures that expose the film.

Radiographs can be made with a few different x-ray energies, for optimal contrast in different parts of the exploding load. Figure 15 shows the aluminum attenuation length vs. x-ray energy and the K, L, and M-shell energies from selected metals (listed in Table 4.1). The most interesting energies are those that will give good contrast radiographs of the transition region between low density plasma and warm dense aluminum: Ti K-shell (4.7-5 keV), Mo L-shell (2.5-2.9 keV), or Cu L-shell (0.9-1.1 keV) x-rays. For example, Ti K-shell x-rays are attenuated by 0.3 mm of 0.1-1 g/cm^3 density aluminum by a factor of 2-1000, increasing with density. Mo or Cu L-shell x-rays have the same attenuation range for densities 3 times smaller. Other options in Figure 15 will be used to examine lower or higher density ranges.

The timing jitter of Leopard with respect to the Zebra current is currently 25-100 ns, depending on the condition of the Zebra trigger generators, spark gaps, and gas switch. This timing jitter is acceptable for our experiment, as we are interested in the entire evolution of the load. We can accumulate a full sequence of radiographs (randomly) over many discharges by repeating the experiment with the same load parameters.

A second way to radiograph loads has recently been developed on Zebra: by placing one or more wire x-pinches in the return current path. This has been successfully implemented on Zebra by Dr. Presura, with x-pinch spots of diameter < 10 μm achieved. The x-pinches flashed at Zebra currents between 100 and 500 kA, producing a single x-ray burst of duration < 1 ns. Radiographs generated from 35 and 50 μm thick tungsten x-pinches were captured on Tritium film from General Electric, filtered by 12.5 μm thick titanium foil and 12.5 μm polycarbonate film. Tritium film exhibits a resolution of about 50 μm. The resolution of the radiograph of the load is higher, thanks to magnification in the x-ray backlighting system. A contrast ratio of about 1:1000 can be achieved. Better results are expected with x-ray film with a film resolution of 2 μm and a contrast ratio of 1:10,000.

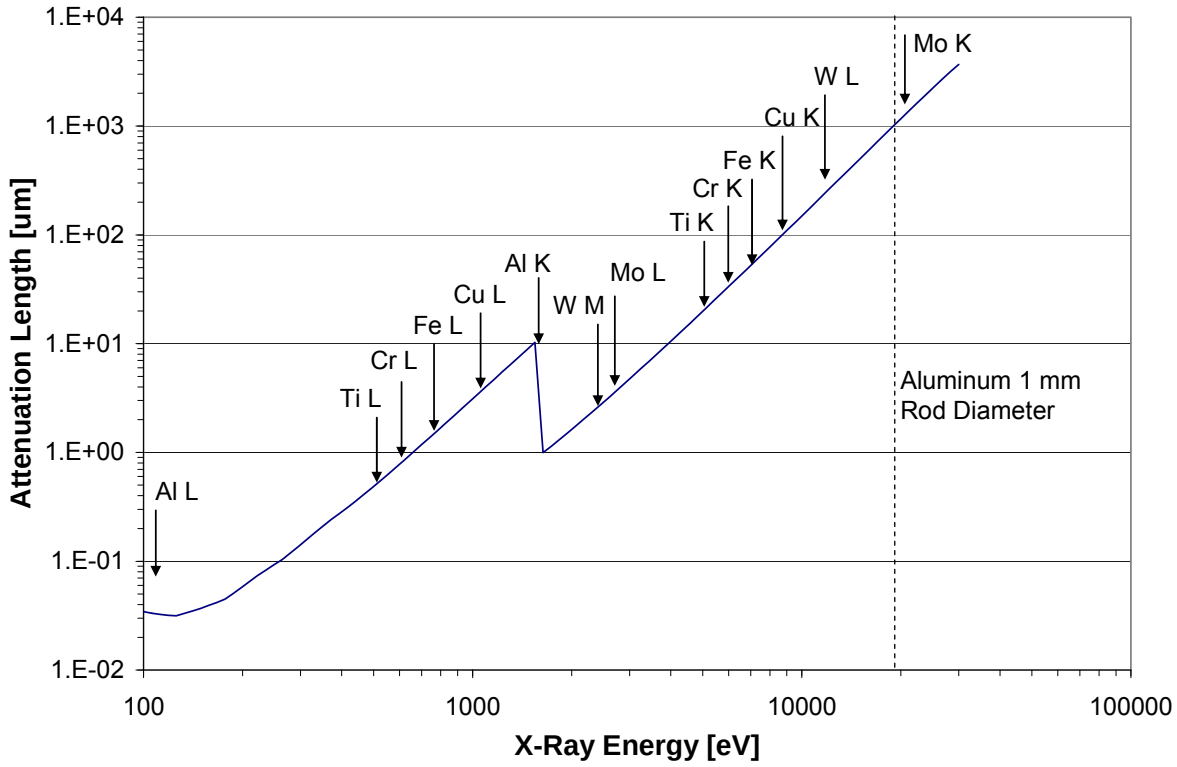

Figure 15. Aluminum attenuation length at solid density (2.699 g/cm^3), with K, L, & M-shell energies indicated for selected x-ray backlighter metals (Table 4.1). The attenuation curve has been generated from: http://henke.lbl.gov/optical_constants/atten2.html.

Table 4.1. Compilation of K, L and M-shell energies for neutral atoms, taken from: http://henke.lbl.gov/optical_constants/pert_form.html. References in the table are: (1) J. A. Bearden and A. F. Burr Rev. Mod. Phys. **39**, 125 (1967). (2) M. Cardona and L. Ley, Eds., *Photoemission in Solids I. General Principles* (Springer-Verlag, Berlin, 1978). (3) J. C. Fuggle and N. Martensson, J. Electron Spectrosc. Relat. Phenom. **21**, 275 (1980). (4) Unpublished. (5) S. Kraft, J. Stumpel, P. Becker, U. Kuetgens, Rev. Sci. Instrum. **67**, 681 (1996).

	Al		Ti		Cr		Fe		Cu[eV		Mo			
Shell	**[eV]**	**Ref**	**[eV]**	**Ref**	**[eV]**	**Ref**	**[eV]**	**Ref**	**]**	**Ref**	**[eV]**	**Ref**	**W [eV]**	**Ref**
M5											228	3	1,809	1
M4											231	3	1,872	1
M3			33	3	42	3	53	3	75	3	394	3	2,281	1
M2			33	3	42	3	53	3	77	3	412	3	2,575	1
M1			59	3	74	3	91	3	123	3	506	3	2,820	1
L3	73	4	454	3	574	3	707	3	933	3	2,520	1	10,206	1
L2	73	4	460	3	584	3	720	3	952	3	2,625	1	11,544	1
L1	118	2	561	3	696	3	845	3	1,097	3	2,866	1	12,100	1
K1	1,560	1	4,966	1	5,989	5	7,111	5	8,981	5	20,000	5	69,525	1

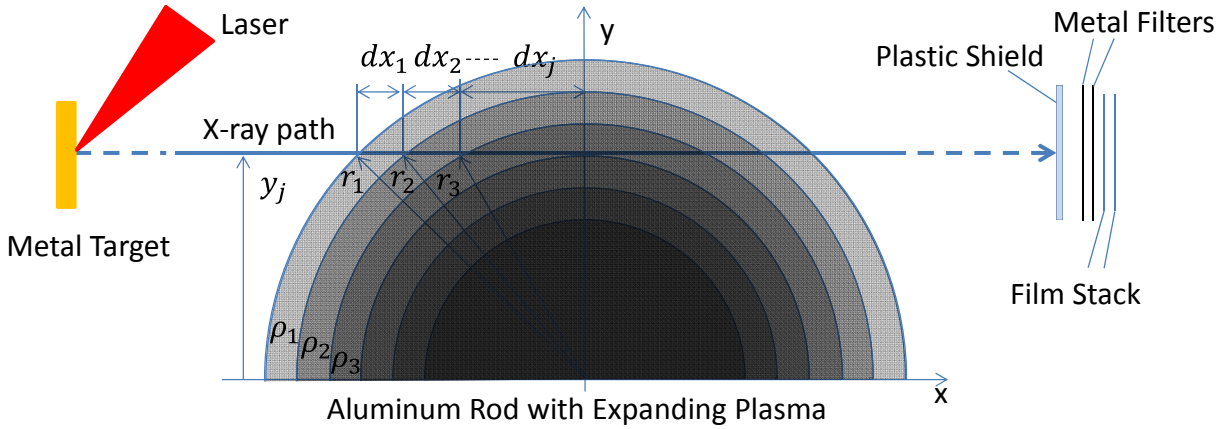

Figure 16. X-ray absorption path through different plasma layers of the barbell load. X-rays are generated by the Leopard laser hitting a metal target or by an x-pinch that is located at one of the current return rods of the load assembly.

In order to investigate the penetration of x-rays through the barbell load, we performed a line-of-sight integration (Figure 16). The intensities of the x-rays are absorbed in the different layers according to

$$I_j = I_0 * \exp\left(\mu(E) x_j\right), \quad x_j = \sum_{i=1}^{j-1} \frac{\rho_i}{\rho_0} \left\{ (r_i{}^2 - y_j{}^2)^{1/2} - (r_{i+1}{}^2 - y_j{}^2)^{1/2} \right\}$$

Where I_j is the transmitted intensity at the height y_j, $\mu(E)$ is the aluminum mass absorption coefficient at x-ray energy E, and x_j is the target thickness at solid density.

The result of the numerical integration is shown in Figure 17 and Figure 18. The line-of-sight x-ray absorption calculation used R-MHD MHRDR modeling results from Irvin Lindemuth.

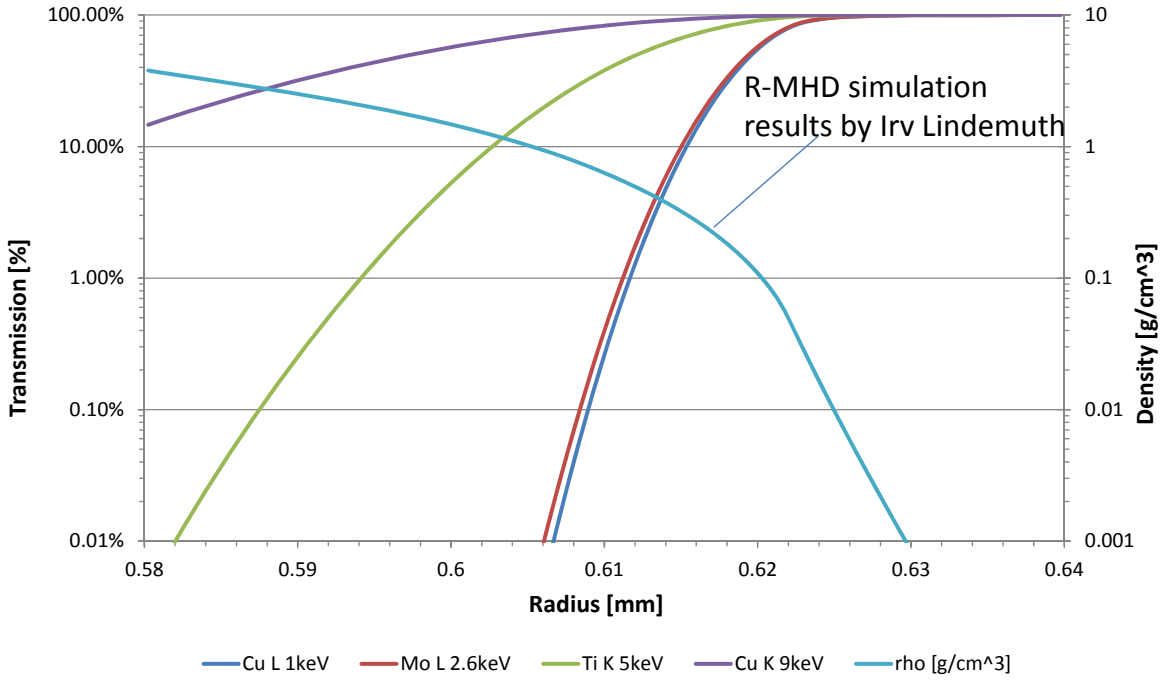

Figure 17. Graph with transmission plots for different x-ray energies.

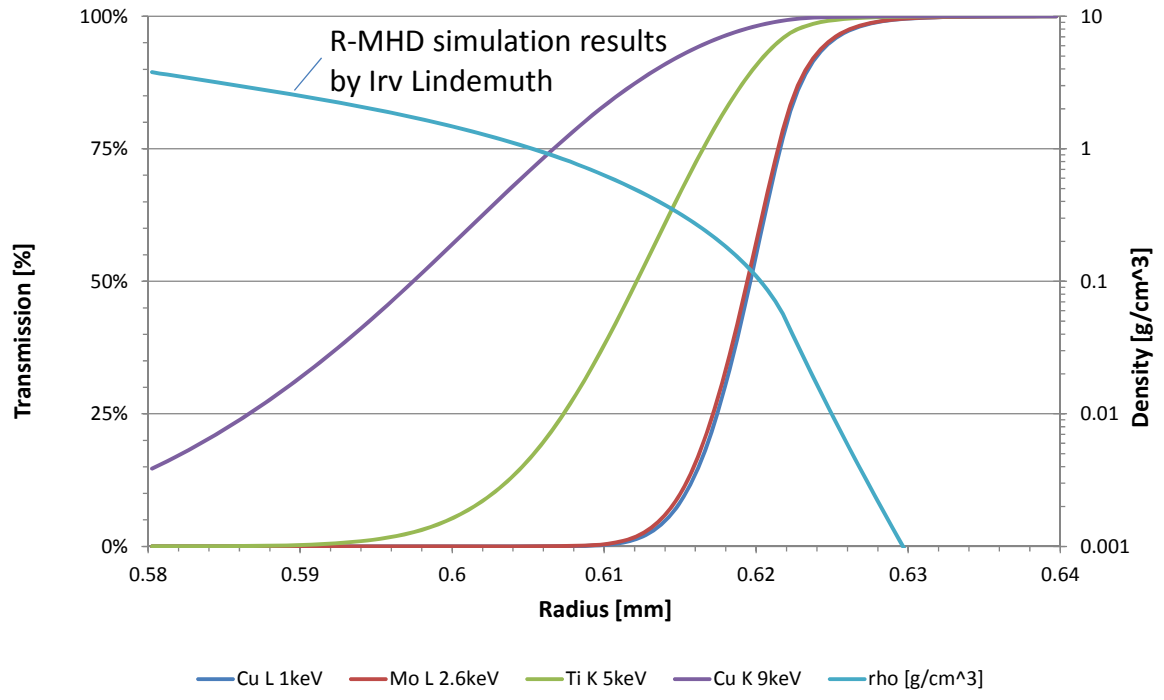

Figure 18. Same as in Figure 17, but with linear axis.

5 EUV Spectroscopy

5.1 EUV Spectrometer Dispersion Corrections & PrismSPECT Units Conversion

The time-resolved EUV spectra from the McPherson Model 310G grazing incidence spectrometer are captured by a MCP/CCD detection system. In order to compare the spectroscopic modeling results from PrismSPECT with those obtained from the Model 310G, the spectra have to be converted to photons/nm. This requires examining the dispersion of the EUV light onto the MCP surface. This leads to a conversion formula that allows converting the location on the MCP into a calibrated wavelength scale. In addition, the derived formula allows for corrections of the MCP misalignment with respect to its ideal tangential placement. We then derive a small dispersion correction, due to the nonlinear conversion.

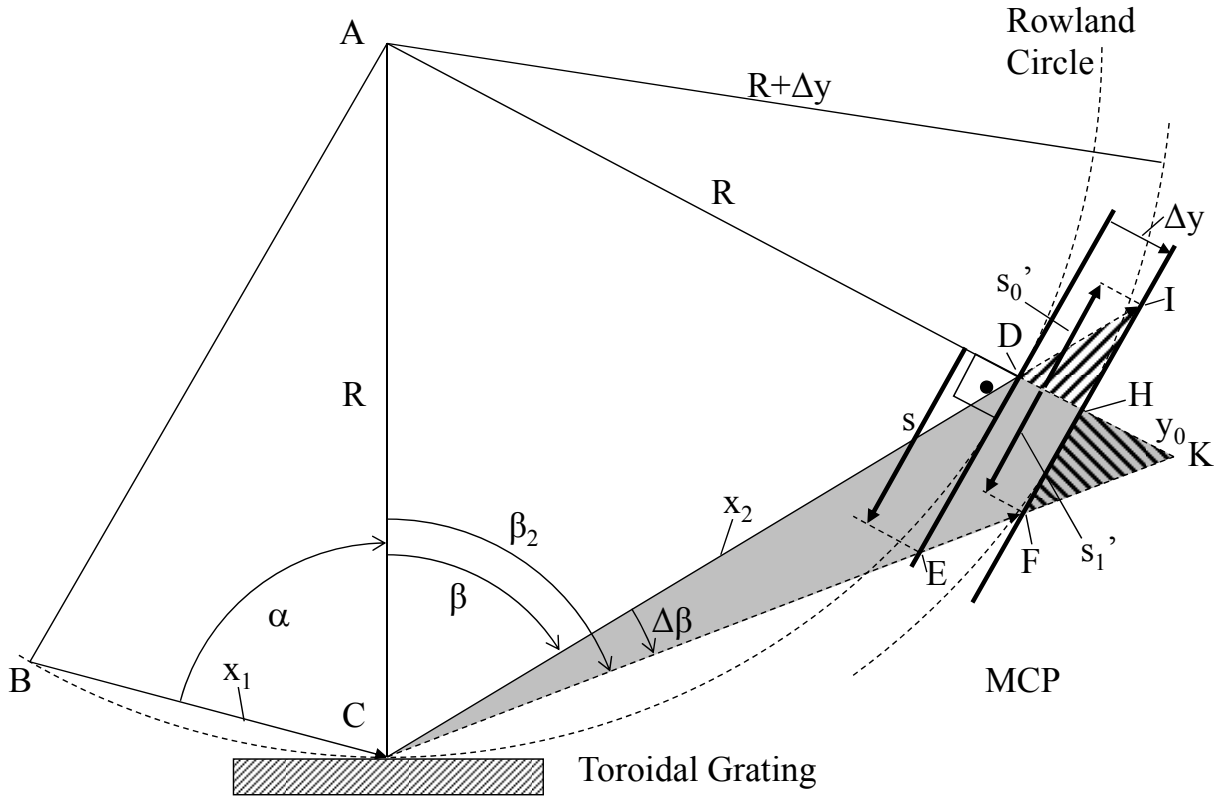

Figure 19. Geometric relationships to calculate the wavelength position across the MCP when the MCP has an offset of Δy with respect to the Rowland circle. The angle of incidence is α and the central exit angle is β. $\beta_2 = \beta + \Delta\beta$ is the angle of the ray CE that refers to the location s on the tangential plane and is also the angle of the ray CF that refers to the location s_1' on the displaced MCP surface.

We first want to arrive at a formula that will give us the corrected wavelength for location $s_1' = \overline{FH}$ on the MCP with offset $\Delta y = \overline{DH}$ (Figure 19). Define $y_0 = \overline{HK}$ and $\sphericalangle DKC = \beta - \Delta\beta$, $\sphericalangle DCK = \Delta\beta$. Therefore, the law of sines for $\triangle CDK$ gives

$$\frac{y_0+\Delta y}{\sin\Delta\beta} = \frac{x_2}{\sin(\beta-\Delta\beta)} \qquad (1)$$

With $\sphericalangle HFK = \beta - \Delta\beta$, we obtain from the law of sines in $\triangle FHK$:

$$y_0 = \frac{s_1'}{\tan(\beta - \Delta\beta)}$$

With $x_2 = 2R\cos\beta$, this yields:

$$s_1'\cos(\beta - \Delta\beta) + \Delta y \sin\big(\beta - \Delta\beta\big) = x_2 \sin\Delta\beta \quad (2)$$

After some algebra, using $x_2 = 2R\cos\beta$, we arrive at:

$$\Delta\beta = \operatorname{atan}\left[\frac{s_1'+\Delta y\tan\beta}{2R+\Delta y - s_1'\tan\beta}\right] \quad (3)$$

We now examine corrections for an MCP that is offset by Δy and tilted by the tilt angle Δγ.

In Figure 20, the shaded triangles give $\sphericalangle HFG = 90° - (\beta - \Delta\beta)$, $\sphericalangle FGH = 90° + \beta - \Delta\beta - \gamma$, $\sphericalangle JIH = 90° - \beta$, and $\sphericalangle HJI = 90° + \beta - \gamma$.

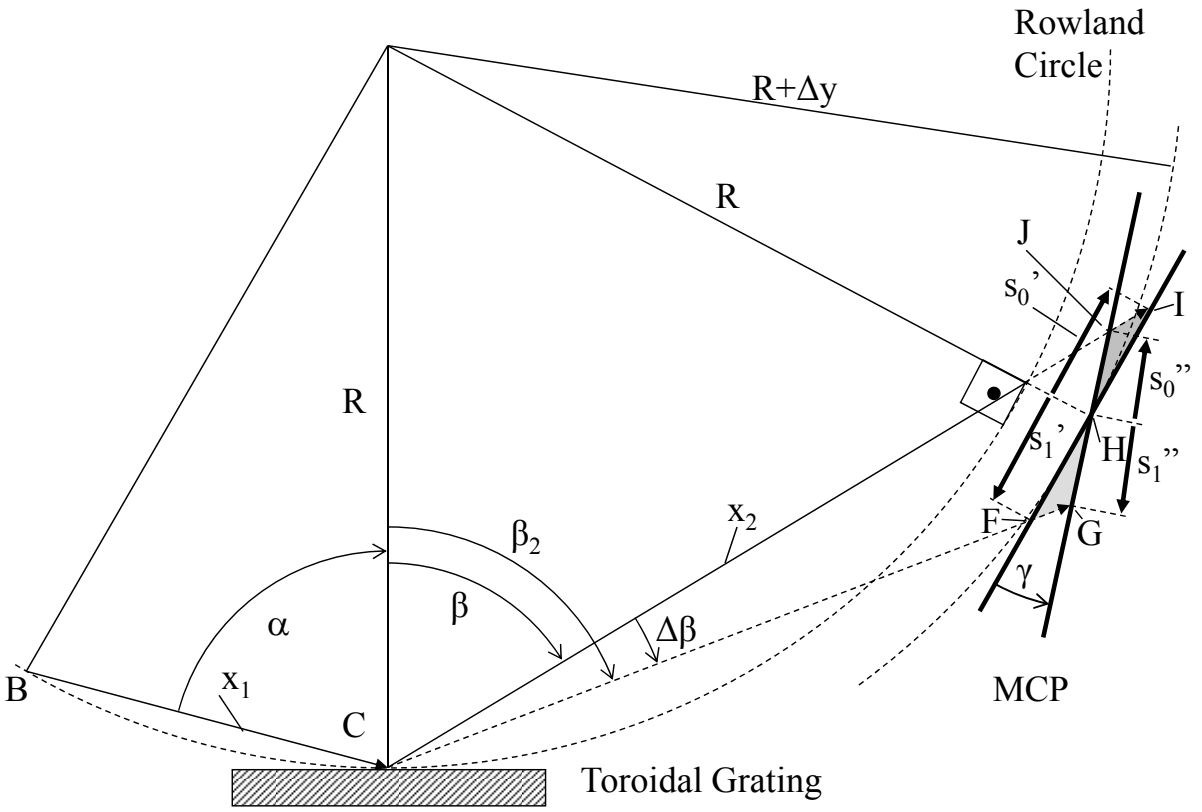

Figure 20. Tilted MCP with offset Δy and tilt Δγ. Here, $\beta_2 = \beta + \Delta\beta$ is the angle of the ray CG that refers to the position s_1" on the tilted MCP surface.

The law of sines for the two shaded triangles gives:

$$s_1' = s_1'' \frac{\cos(\beta - \gamma - \Delta\beta)}{\cos(\beta - \Delta\beta)} \quad (4)$$

$$s_0' = s_0'' \frac{\cos(\beta - \gamma)}{\cos(\beta)} \quad (5)$$

We insert (4) into (2) and solve for $\Delta\beta$:

$$\Delta\beta = \operatorname{atan}\left[\frac{s_1''\cos(\beta-\gamma)+\Delta y \sin\beta}{(2R+\Delta y)\cos\beta - s_1''\sin(\beta-\gamma)}\right] \quad (6)$$

The dispersion formula with correction for the MCP with offset Δy and tilt angle γ is:

$$m\lambda = d(\sin\alpha - \sin(\beta + \Delta\beta)) \quad (7)$$

5.2 Spectrometer Calibration

We first identified the spectral line with the help of NIST tables for aluminum ions. The derived dispersion formula and its parameters were entered into an Excel spreadsheet, where the sum of all wavelength errors was minimized using the 'Solver' add-in. This minimized the wavelength error over a wide wavelength range (8 nm – 36 nm).

Figure 21 shows the wavelength region that is of greatest interest to our Megagauss experiments, where the emission lines of multiply ionized aluminum is observed and compared to PrismSPECT modeling. Figure 22 shows the complete wavelength region from 8 nm to 36 nm. The calibration results are summarized in Table 5.1.

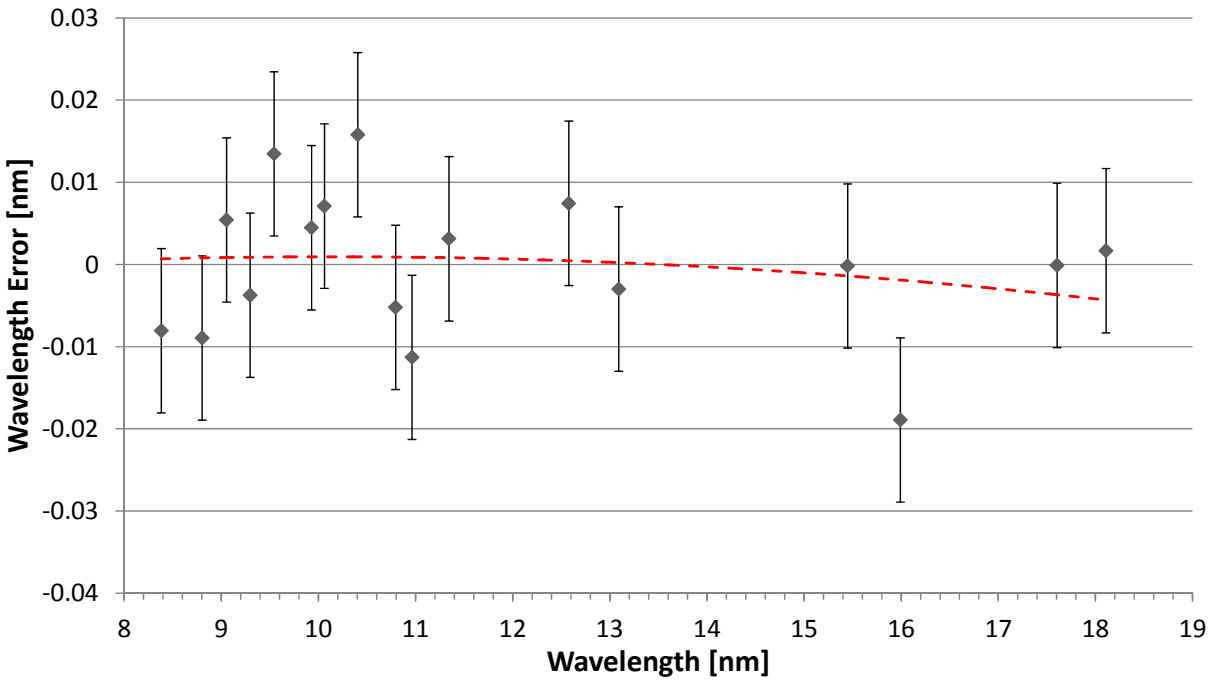

Figure 21. Calibration result for the wavelength region between 8 nm – 18 nm.

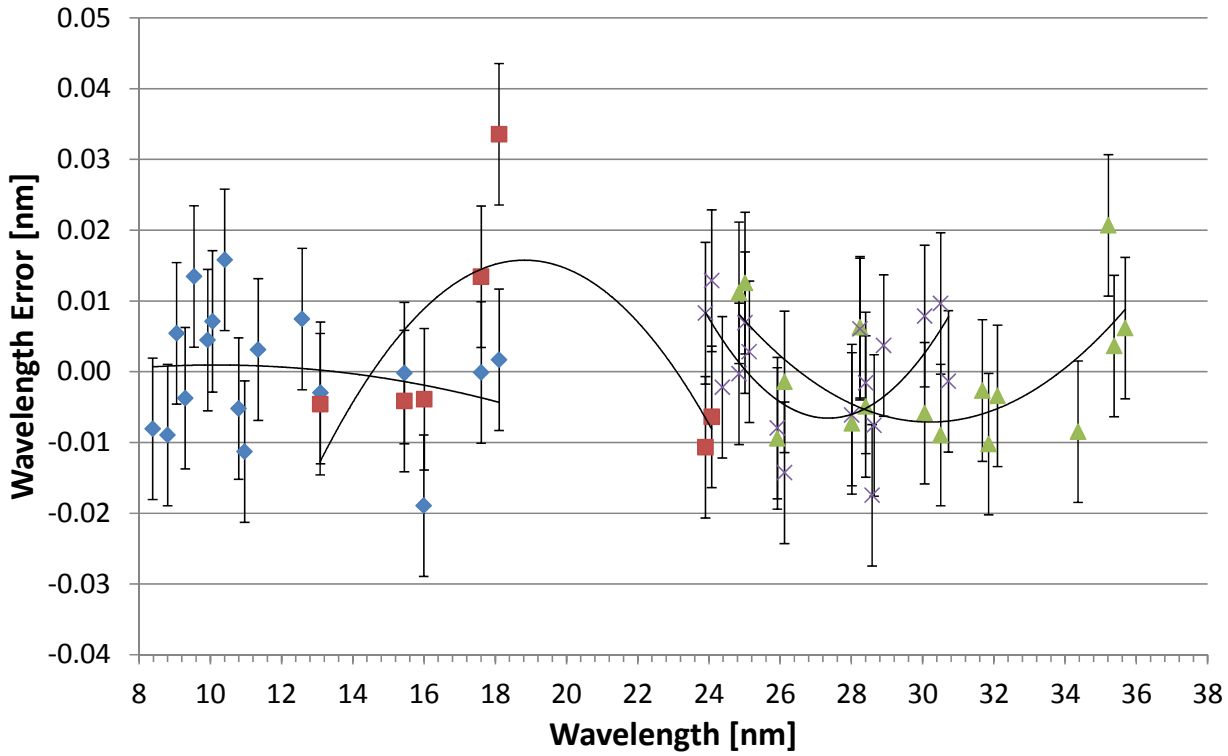

Figure 22. Calibration result for a wavelength region from 8 nm to 36 nm.

In the calibration, we kept the entrance angle α, the MCP offset Delta_Y and the fiber optic reducer magnification M constant but allowed the counter offset X_00 and the MCP tilt angle γ to vary freely for each wavelength region. The standard deviation is σ = 0.01 nm, which represents 1 CCD pixel.

Table 5.1. Calibration result for four wavelength regions.

Shot #	Min [nm]	Max [nm]	Alpha [degree]	X_00 [inch]	Gamma [degree]	Delta_Y [mm]	M
1439	8.229	18.243	85.056	-0.083	-1.016	-0.243	3.028
1443	12.955	24.194	85.056	-0.089	-1.057	-0.243	3.028
1447	18.388	30.743	85.056	-0.089	-1.206	-0.243	3.028
1448	24.448	38.130	85.056	-0.086	-1.271	-0.243	3.028

5.3 Dispersion Correction for Measured Spectral Intensities

In order to compare with PrismSPECT results, we need to correct the measured spectra for uneven spectral densities across the MCP. We want to derive the *reciprocal linear dispersion* $\frac{d\lambda}{ds}$ of the grating at the MCP surface, where *s* is the location parameter across the MCP surface:

$$\frac{d\lambda}{ds} = -\frac{d}{m}\cos(\beta + \Delta\beta)\frac{d(\Delta\beta)}{ds}, \text{ we set } s \coloneqq s_1''$$

We set $s \coloneqq s_1''$ and set $\varepsilon \coloneqq \frac{s\cos(\beta-\gamma)+\Delta y \sin\beta}{(2R+\Delta y)\cos\beta - s\sin(\beta-\gamma)}$. The calculate the differential d(Δβ)/ds:

$$\frac{d(\Delta\beta)}{ds} = \frac{d}{ds}\operatorname{atan}\varepsilon = [1+\varepsilon^2]^{-1}\frac{d\varepsilon}{ds}$$

$$\frac{d\varepsilon}{ds} = \frac{\cos(\beta-\gamma)}{(2R+\Delta y)\cos\beta - s\sin(\beta-\gamma)} - \frac{(s\cos(\beta-\gamma)+\Delta y\sin\beta)(-\sin(\beta-\gamma))}{\left((2R+\Delta y)\cos\beta - s\sin(\beta-\gamma)\right)^2}$$

$$= \frac{(2R+\Delta y)\cos\beta\cos(\beta-\gamma) + \Delta y\sin\beta\ \sin(\beta-\gamma)}{\left((2R+\Delta y)\cos\beta - s\sin(\beta-\gamma)\right)^2}$$

Therefore:

$$\frac{d(\Delta\beta)}{ds} = \frac{\left((2R+\Delta y)\cos\beta - s\sin(\beta-\gamma)\right)^2}{\left((2R+\Delta y)\cos\beta - s\sin(\beta-\gamma)\right)^2 + (s\cos(\beta-\gamma)+\Delta y\sin\beta)^2} * \frac{d\varepsilon}{ds}$$

We put this result into the formula for dλ/ds and obtain:

$$\frac{d\lambda}{ds} = \frac{d}{m}(-\cos(\beta+\Delta\beta))\frac{(2R+\Delta y)\cos\beta\cos(\beta-\gamma) + \Delta y\sin\beta\ \sin(\beta-\gamma)}{\left((2R+\Delta y)\cos\beta - s\sin(\beta-\gamma)\right)^2 + (s\cos(\beta-\gamma)+\Delta y\sin\beta)^2}$$

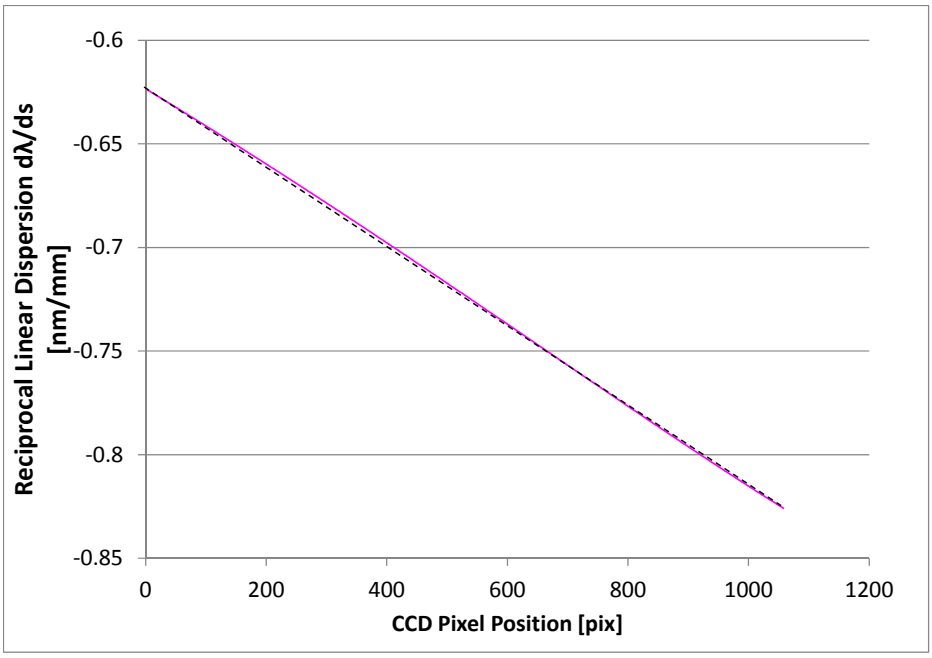

Figure 23. Plot of the reciprocal linear dispersion dλ/ds in [nm/mm] versus CCD pixel position.

The plot result (violet line) is shown in Figure 23. The dispersion dλ/ds only changes by about 25% across the CCD (or MCP) and is almost linear (black dashed line).

5.4 Comparing PrismSPECT Modeling Results with Experimental EUV Spectra

The program PrismSPECT calculates specific intensities of atomic & ionic emission spectra in units of [erg / eV s cm^2 sr]. In order to compare with experimental spectra, we have to multiply the PrismSPECT output by experimental parameters and convert to [Photons/nm]. Each experimental pixel count has to be divided by the corresponding wavelength interval, which depends on the dispersion of the EUV spectrometer.

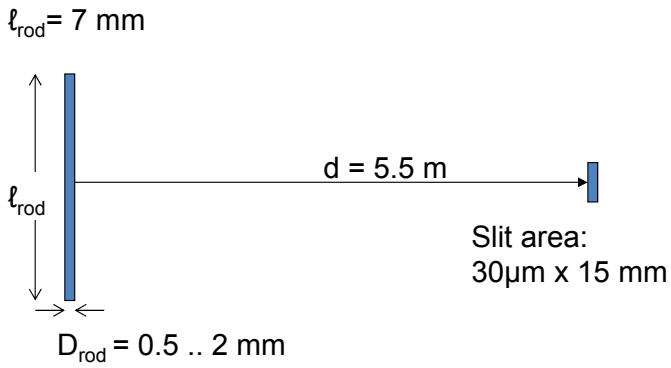

Figure 24 Geometrical entities for determining the solid angle.

Prism uses the units [erg /s /eV/cm^2/sr], where[erg] = [10^{-7} J], [eV] = [e*J/C], therefore [erg/eV] = [10^{-7} J C / e/J] = 6.241x10^{11} J/J. In Figure 24, the rod area is 1 mm x 7 mm = 0.07 cm^2 and the solid angle for the EUV spectrometer is $\Omega = a_{slit}/d^2 = 1.49\text{x}10^{-8}$ sr. The MCP integration time is 6 ns = 6x10^{-9} s. To convert into photons per nm, we have to multiply by λ/hc (convert J/J to number of photons/J) and by $dE/d\lambda = hc/\lambda^2$ (to convert to photons/nm), so by a factor $1/\lambda$, where λ is in units of nm. The total conversion factor is

$$3.9 \text{ x } 10^{-6} \text{ [s eV cm}^2 \text{ sr / erg] [N}_{photons}\text{]},$$

which still has to be divided by the corresponding wavelength λ in units of [nm] in the spreadsheet to obtain [$N_{photons}$/nm], the number of photons per nm.

5.5 Line-of-sight Integration through R-MHD Modeling Results

From a modeling data set that Dr. Sergey Garanin provided for us, we performed PrismSPECT modeling with a subsequent, simplified line-of-sight integration that assumed a flat aluminum surface instead of a round one (Figure 25).

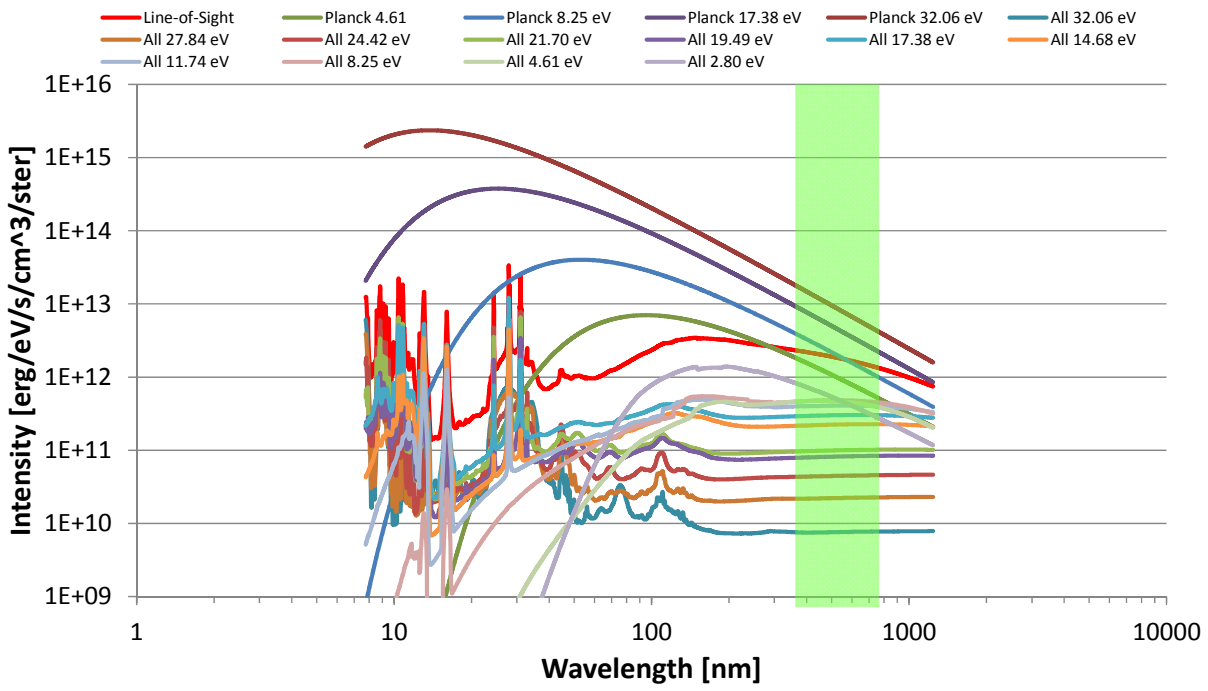

Figure 25. PrismSPECT modeling results from an MHD-R modeling data set by Dr. Sergey Garanin and line-of-sight integration (red). The green area represents the wavelength region for visible spectroscopy.

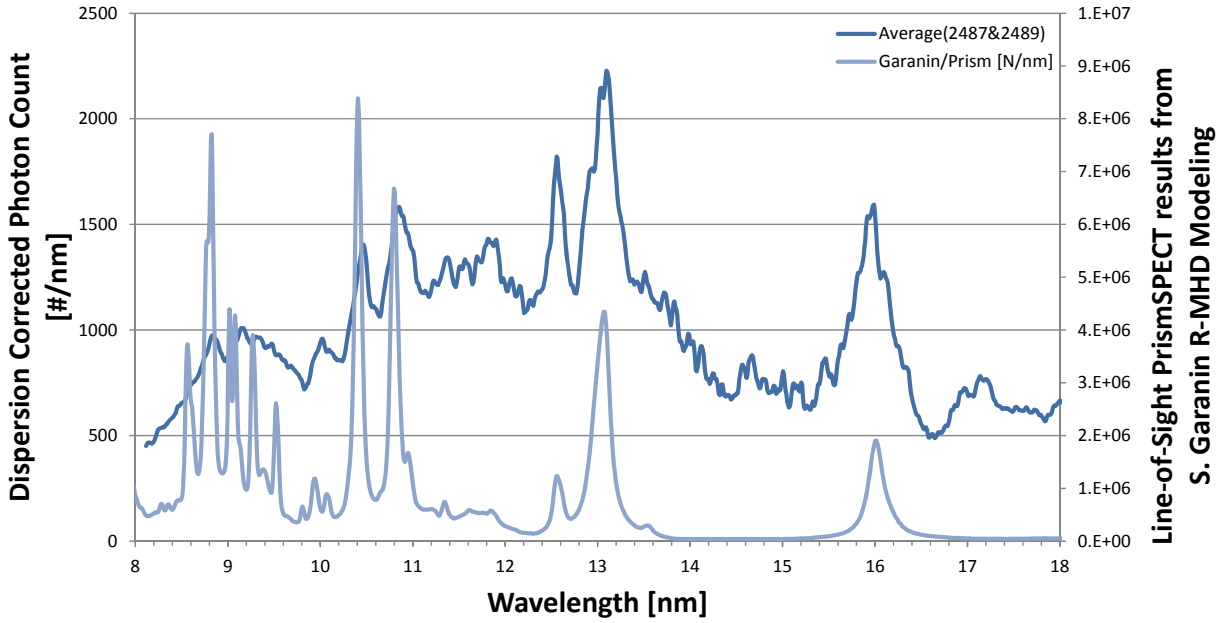

Figure 26 Comparison of experimental spectrum with line-of-sight integrated modeled spectrum from PrismSPECT, using an MHD-R modeling result data set from Dr. Sergey Garanin.

Figure 26 shows a comparison between experimental and modeled spectra. The peak plasma temperature in Garanin's data set was 32 eV. The comparison suggest that the MHD-R modeling result gave too high a plasma temperature.

5.6 Image & Data Processing for the MCP Images of the EUV Spectrometer

In order to extract good spectral data from the MCP images obtained from the McPherson Model 310/G extreme ultraviolet spectrometer, the images have to been processed with regard to background and the obtained spectra have to be adjusted for variation in sensitivity across the MCP surface.

The CCD camera is biased with a DC offset, which is about 4800. This bias level is reached after the CCD camera has been cooled down to -20 °C. A representative background image has been filtered and smoothed and will be used to subtract from each captured EUV spectral image. The background in Figure 27 varies between 4790 – 4812 counts across the image area.

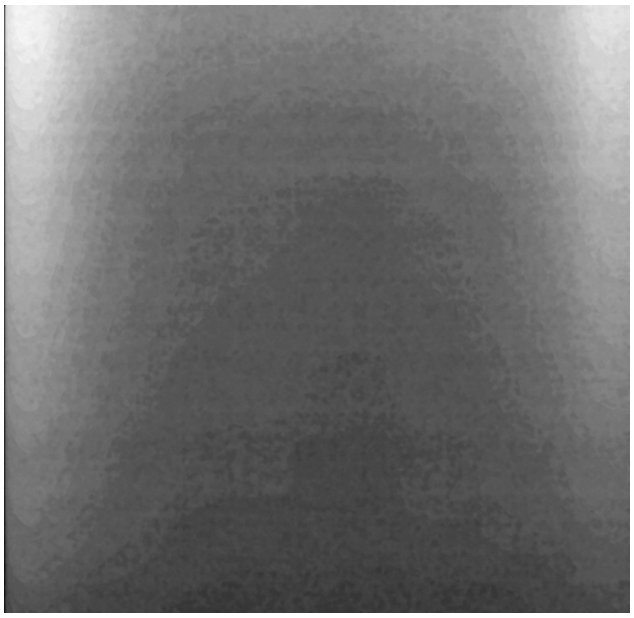

Figure 27 Smoothed CCD camera background.

Figure 28 shows a representative line profile. The entrance slit width was set at 30 μm and the grating mask was removed for better throughput, since the spectral images were fairly weak. The FWHM is about 9 pixels, which is less than 0.1 nm. Let us look at this line profile on a logarithmic scale, to see what background this line produces.

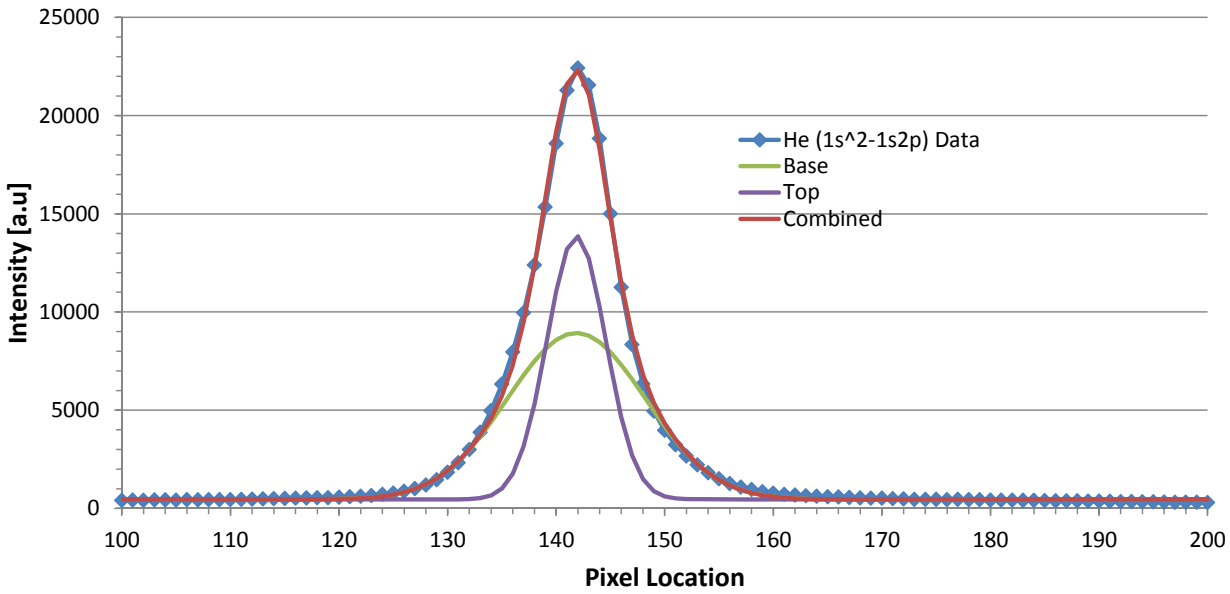

Figure 28 Spectral line profile represented by two Gaussian distribution functions. The FWHM is about 9 pixels.

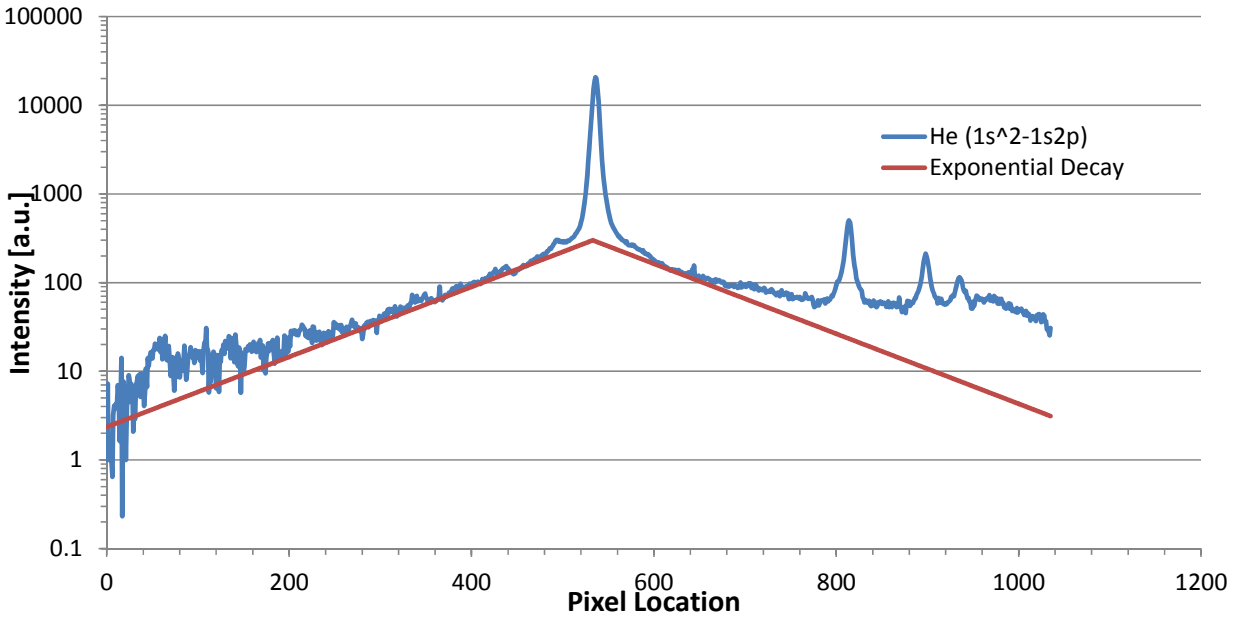

Figure 29. Line profile on logarithmic scale. One can see 'shoulders' to the left and right, which represent and exponential decay due to pixel to pixel crosstalk.

The logarithmic representation of the line profile in Figure 29 reveals 'shoulders' of exponential decay from the central line. This is due to pixel to pixel crosstalk. We remove this background with the help of a Fast Fourier Transform (FFT) convolution (next Section).

5.7 Subtraction of MCP Background from the Exponential Decay

A direct FFT deconvolution of the MCP image by a spread function was not successful. So, we investigated generating a background image of the exponential decay. Assume the primary image I_0 and the exponential spread function f produce the recorded image I_1:

$$I_1 = I_0 + f * I_0$$

If the spread function f were known, then the convolution of the recorded image I_1 would yield:

$$I_2 = f * I_1 = f * I_0 + f * (f * I_0)$$

Subtracting I_1 from I_2 yields:

$$I_1 - I_2 = I_0 - f * (f * I_0) \approx I_0 , \text{ for } f * (f * I_0) << I_0$$

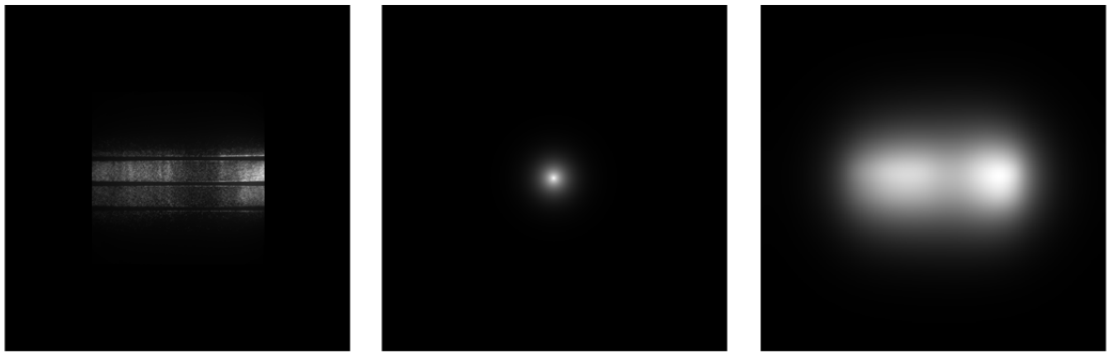

Figure 30. Left: EUV spectra on an enlarged 'canvas'. Middle: exponential spread function. Right: convolution of the EUV spectra with the spread function, which will be used as the new background.

Figure 30 details the image processing steps of the generation of the convoluted background picture, which we will use to subtract from the original EUV spectra. This is performed individually for each Zebra shot, meaning for each EUV spectral image, since this background depends on the actual EUV image.

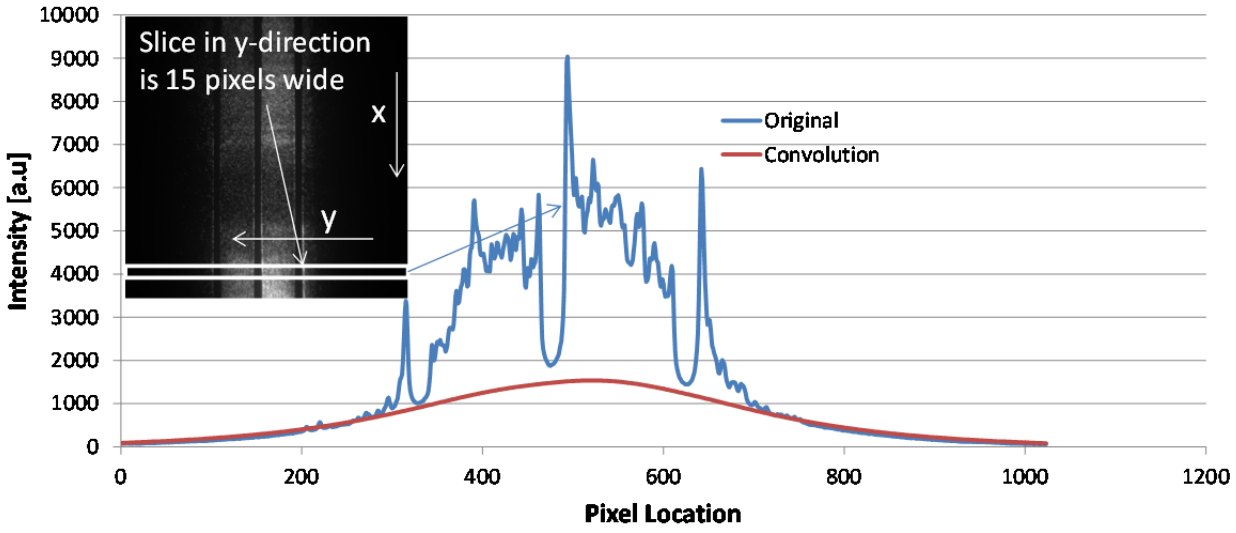

Figure 31. Result from the scaled convolution with an exponential spread of 1/(100 pixels). The convolution shows general agreement but the gaps are not well represented.

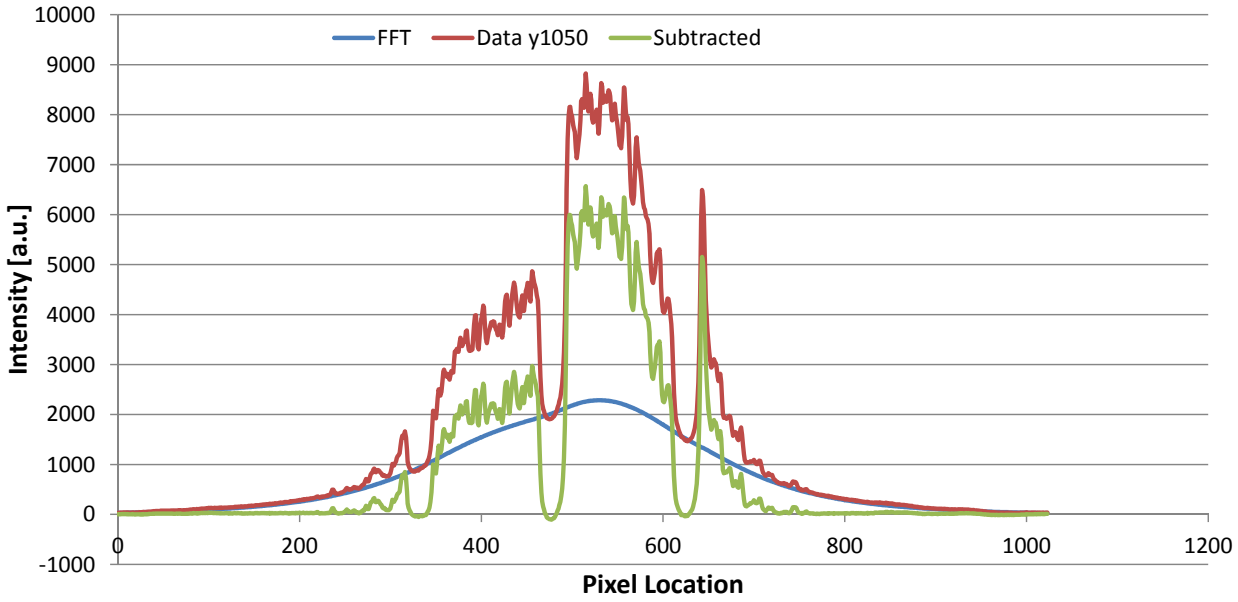

Figure 32. A better match is achieved for a narrower spread function with an exponential spread of 1/(55 pixels).

Figure 31 and Figure 32 show the applied convoluted spread function. In the last case, where an exponential spread of 1/(55 pixels) was used, the agreement is very good. Next, let us look at the result along the strip gaps (i.e. the gaps left between adjacent MCP strips).

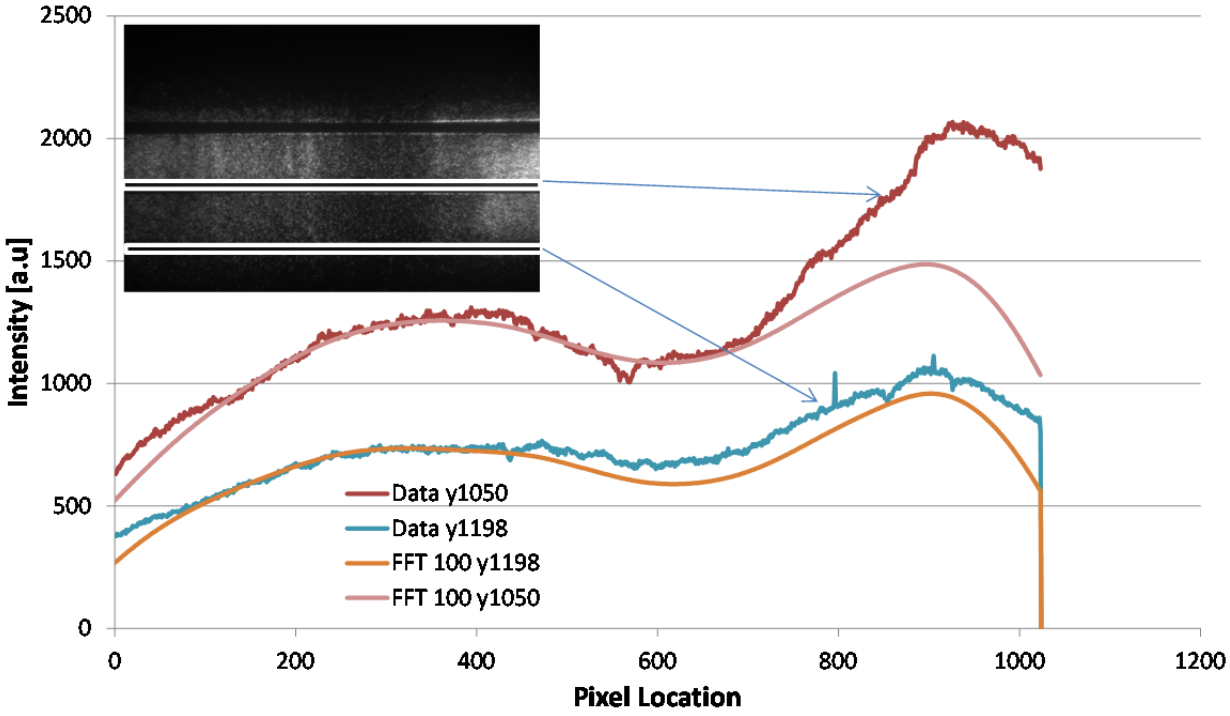

Figure 33. Comparison between the convoluted spread function and the original EUV data, looking along the gaps between adjacent MCP strips.

Figure 33 shows the comparison between the convoluted spread function and the original EUV data. If the convolution were perfect, it would completely follow the intensity profile of the gaps. Although there is a fairly good agreement in the center portion, the edges are not well reproduced. We therefore used an interpolated approach:

- We use the pixel values of the MCP strip gaps to scale the convoluted background of a 1/(55 pix) exponential spread function for each y-slice;
- We then subtract this scaled y-slice of the convoluted background from the corresponding y-slice of the MCP image;
- The resultant image is a much improved background corrected spectrum.

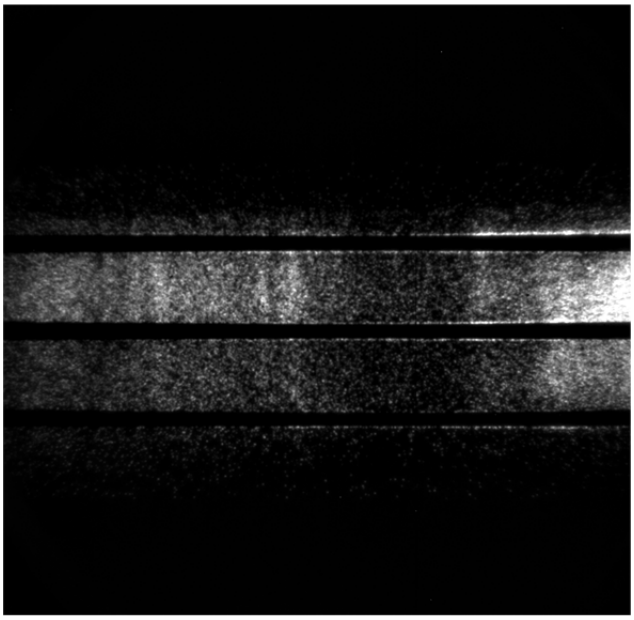

Figure 34. Final result from the image processing.

Figure 34 and Figure 35 show the EUV spectral image before and after the interpolated background subtraction. (The static background was already subtracted.)

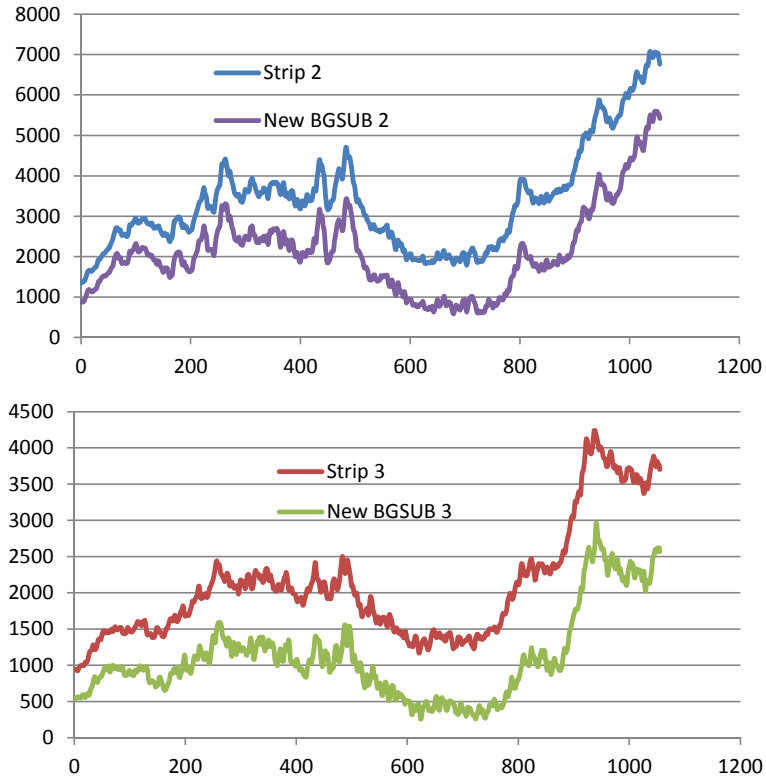

Figure 35. Examples of the spread function background subtraction. Spectral data (intensity [counts] vs. pixel location).

5.8 ImageJ EUV Spectral Image Corrections

The toroidal grating of the EUV spectrometer, which operates in the Rowland circle mount, produces image distortions. The entrance slit produces spectral line images on the MCP that are slightly curved (Figure 36, Table 5.2). The radius of curvature is about 4057 pixels and the center of the circle lies at the point (x, y) = (3624, 577).

We therefore wrote an ImageJ plugin, which straightens these curved spectral lines before the 'plot profile' operation to average over the width of the MCP strips.

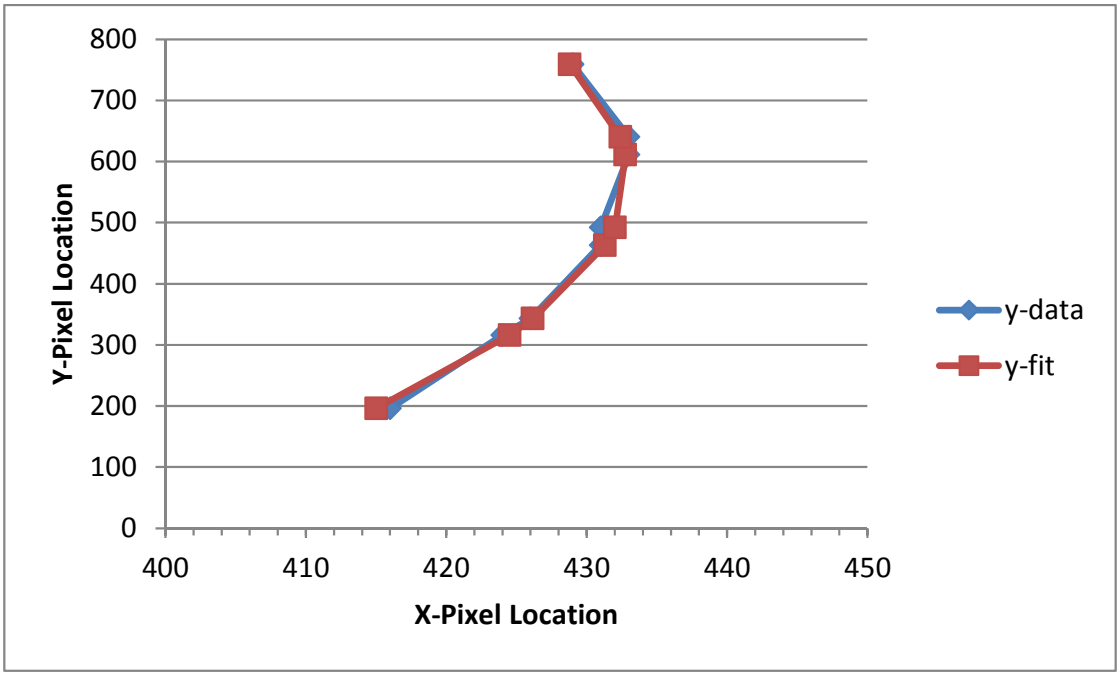

Figure 36. Image shift over the MCP surface as recorded by the CCD camera. Plotted is the location of a strong line emission. Then a fit is applied to the data, which is a portion of a circle with radius r and offsets x_0 and y_0. Please note that the scaling is different for the *x*- and *y*-axis.

Table 5.2. Result from circular fit; x_0 and y_0 are the x- and y-offsets, r is the radius of curvature.

x0	-3623.67
y0	576.6049
r	4056.57

5.9 Image Shift Java Code

This Java code is implemented as an ImageJ plugin and is called during the image processing of EUV spectral images to correct for the curved spectral line on the MCP.

```
public class Image_Shift2 implements PlugInFilter, Measurements {
	public int setup(String arg, ImagePlus imp) {
		if (IJ.versionLessThan("1.37j"))
			return DONE;
		else
			return DOES_ALL+DOES_STACKS+SUPPORTS_MASKING;
	}

	public void run(ImageProcessor ip) {
		int imageWidth, imageHeight, yCenter;
		double dx1=0, dx2=0, dy1=0, dy2=0, r=0, r1=4056.57, r2=5000.0, r3=4500,
y0=576.6049;
		float dxdy, dx=(float)0, ddx=(float)0;
		r=r1;
		ImagePlus imp = IJ.getImage();
		imageWidth = ip.getWidth();
		imageHeight = ip.getHeight();

		for (int y=0; y<imageHeight; y++){
			dx = (float)r*(float)((float)1-Math.cos(Math.sin(((float)y-(float)y0)/(float)r)));
			ddx = dx - (int)dx;
			for (int x=imageWidth-(int)dx-1; x>1; x--){
				ip.set((x+(int)dx), y, (int)((ddx)*ip.get(x-1,y)+(1-ddx)*ip.get(x,y)));
			}
		}
	}
}
```

5.10 Background Subtraction ImageJ Java Code

The whole image processing has been automated with the help of specific ImageJ plugin algorithms written in Java and ImageJ macro calls. We modified an existing ImageJ plugin (BlendImages.java) to perform the static and exponential spread function background subtraction.

Here a listing of only the modified Java code, the modified "BlendImages.java "plugin has been renamed to 'Background_Subtract3':

```
public class Background_Subtract3 implements PlugInFilter {
   static String image1name = "";  //name of the first image ("Image 1")
   static String image2name = "";  //name of the other image that will be added ("Image 2")
   static float weight1;           //weight of the image that the filter is applied to ("Image 1")
   static float weight2 = 0.5f;    //weight of the other image, that will be added ("Image 2")
   static boolean fixWeight1 = false; //Whether to set weight1 = 1. Otherwise weight1 = 1 -
weight2
public int setup(String arg, ImagePlus imp) {
                if (IJ.versionLessThan("1.37j"))
                        return DONE;
                else
                        return DOES_ALL+DOES_STACKS+SUPPORTS_MASKING;
        }

   public void run (ImageProcessor ip) {
        ImagePlus imp1 = IJ.getImage();
        imp1.unlock();
        imp1.show();
        IJ.run("OutliersImageShift");  // Calls the OutliersImageShift ImageJ macro
        IJ.showMessage("Hello");
        imp1.show();
        ImageCalculator ic = new ImageCalculator();
        ImagePlus imp2 = IJ.openImage("D:/Documents/Research/Spectroscopy/MCP
Normalization/Smoothed Dark Frame.fits");  // Opens the normalized smoothed CCD
background image
        imp1 = ic.run("Subtract create", imp1, imp2);          //Subtract smoothed background
from MCP image
        ImageProcessor ip1 = imp1.getProcessor();
        ip1.flipVertical();                                    //Flip the image horizontally & vertically
        ip1.flipHorizontal();
        CanvasResizer cr = new CanvasResizer();            //Enlarge the 'canvas' size, so FFT
can be done on 2048x2048
        ip1 = cr.expandImage(ip1,2048,2048,512,512);       // Place the image at (512,512)
        imp1.setProcessor(null,ip1);
```

```
        ImagePlus conv1 = new ImagePlus();
        conv1 = IJ.openImage("C:/Program Files/ImageJ/plugins/EUV
Spectrometer/Exponential2048-55.fits");
        FFTMath fft1 = new FFTMath();
        fft1.doMath(imp1,conv1);                //Convolute the MCP image by the exponential
spread function image
        ImagePlus cimp2 =  WindowManager.getImage("Result");
                                //get the convoluted image for second background subtraction
        ImageProcessor cip2 = cimp2.getProcessor();
        cip2.setRoi(512,512,1056,1027);      //Clip the convoluted image back to 1056 x 1027
        cip2 = cip2.crop();
        cip2.multiply(1.0/30.0);          //Divide by 30 and then convert from 32-bit back to 16-bit
        cimp2.setProcessor(null,cip2);
        ImageConverter icv = new ImageConverter(cimp2);           // Need ImageConverter to
convert to 16-bit
        icv.convertToGray16();
        ip1.setRoi(512,512,1056,1027);                //Clip the MCP image back to 1056 x 1027
        ip1 = ip1.crop();
      FloatProcessor fp1 = null, fp2 = null, fp3 = null;          // non-float images will be converted
to these
      fp1 = ip1.toFloat(0,fp1);                              // convert MCP image to float
      fp2 = cip2.toFloat(0,fp2);          // this is the cropped convoluted image, the "background"
converted to float
      subtractBackground(fp1, fp2);
         cimp2.close();
         ip1.setPixels(0, fp1);                              // convert back from float
         imp1.setProcessor(null,ip1);
         imp1.show();                      // show the double-background subtracted MCP image
         IJ.showMessage("Press when ImageJ is finished");
         IJ.run("MCP Profiles [Q]");     //Sometimes this doesn't work right and I have to call the
macro by hand
   }


   public static void subtractBackground(FloatProcessor fp1, FloatProcessor fp2) {
            FloatProcessor fp3 = new FloatProcessor(1056,1027);

            int[] y1 = new int[]{400,550,700,550};
            int idx = 0;
            int xw = fp1.getWidth();
            int yh = fp1.getHeight();
            float zfactor = (float)0;
            float zloop = (float) 0;
            String msg1 = " xw " + xw + " yh " + yh;
```

```
            String msg2 = "";
//          IJ.showMessage(msg1);

      float[] pixels1 = (float[])fp1.getPixels();     // array of the pixels of fp1
      float[] pixels2 = (float[])fp2.getPixels();
      float[] pixels3 = (float[])fp3.getPixels();
         for (int i=0; i<xw*yh; i++) pixels3[i] = pixels1[i];         // need an undisturbed copy of the
MCP image
            for (int x=0; x<xw; x++){
                  msg2 = "";
                  zfactor = (float) 0;
                  zloop = (float) 0;
                  for (int iy = 0; iy<3; iy++)
                        for (int dy = -1; dy<=1; dy++)
                              for (int dx = -3; dx<=3; dx++)
                              if(x+dx>=0 & x+dx<=xw){
                                    zloop++;
                                    idx = x+dx+(y1[iy]+dy)*xw;
                                    zfactor = zfactor + (float)pixels3[idx] / (float) pixels2[idx];
                                          // don't want to use pixels1[] instead!!
                              }
                        zfactor = zfactor / zloop;
                        for (int y=0; y<yh; y++){
                        int ip = x + y*xw;
                        pixels1[ip] = pixels1[ip] - (int)(zfactor*(float)pixels2[ip]);
                        // here the pixles1[] gets changed, that's why we need pixels3[] up there
                  }
            }
            return;
   }
```

5.11 ImageJ Macros

The macro “MCP Profiles [Q]” is called in the “Subtract_Background3” plugin. It selects four regions that represent the four central MCP strips and performs the “Plot Profile” ImageJ command, which produces an averaged plot profile over the width of each MCP strip.

```
 macro "MCP Profiles [Q]" {
        makeRectangle(0, 274, 1056, 108);
        run("Plot Profile");
        run("Put Behind [tab]");
        makeRectangle(0, 421, 1056, 108);
        run("Plot Profile");
        run("Put Behind [tab]");
        makeRectangle(0, 568, 1056, 108);
        run("Plot Profile");
        run("Put Behind [tab]");
        makeRectangle(0, 715, 1056, 108);
        run("Plot Profile");
}
```

The macro “OutliersImageShift” calls the “Remove Outliers…” ImageJ command and calls the “Image Shift2” plugin, which straightens the curved spectral lines that are imaged onto the MCP.

```
 macro "OutliersImageShift" {
        run("Remove Outliers...", "radius=1 threshold=500 which=Bright");
        run("Image Shift2");
 }
```

5.12 MCP Sensitivity Corrections

The EUV spectral images have been corrected for static and exponential spread function background, the curved spectral lines have been straightened and the MCP strips have been averaged over their width, plotted and transferred to an Excel spreadsheet. What is left is a sensitivity correction for the MCP, since the response across the MCP is not constant. Surprisingly, the variations in sensitivity across the MCP that were measured under DC operation using a continuous helium microwave plasma source were quite different during the Megagauss experiments on Zebra under pulsed operation.

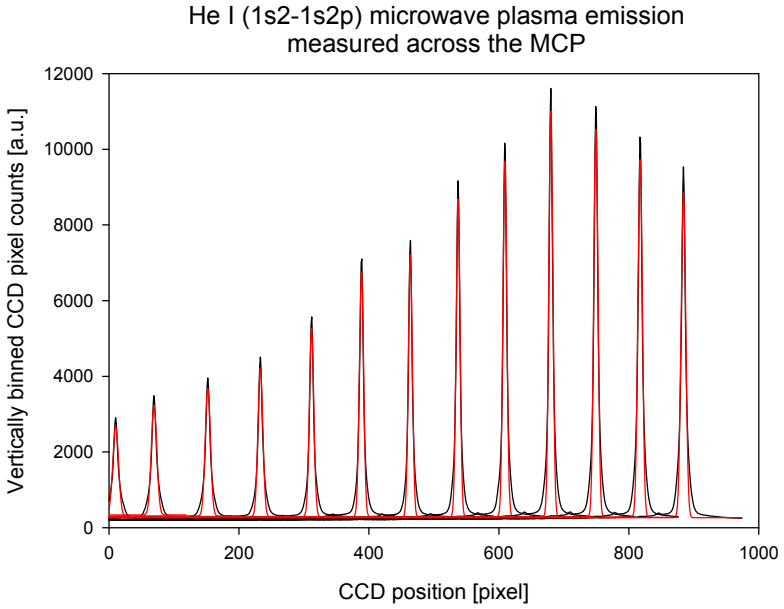

Figure 37. The graph shows sensitivity variations across the MCP by up to a factor 4. Peak sensitivity centered at around pixel location ~700.

Figure 37 shows the MCP sensitivity variations under DC high voltage operation with the helium microwave plasma source. It shows that the sensitivity is highest at around the pixel location 700, falling off to the MCP edges. Under pulsed operation (Figure 38), however, the sensitivity is much increased at the edges, especially at the right side, where the high voltage pulse is fed to the MCP. This behavior is not understood, it may be due to impedance mismatch between the 50 Ω impedance of the coax cable and the 25 Ω impedance of the MCP strips. The other end of the MCP strips has an open circuit (not terminated), therefore the HV pulse causes an open-end reflection, which should double the voltage pulse that is applied.

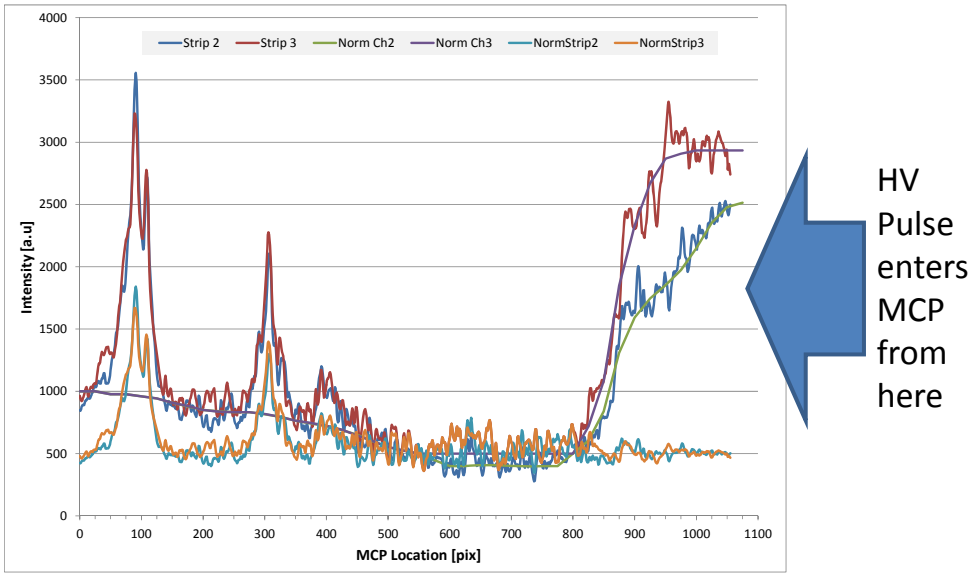

Figure 38. Background subtracted EUV spectra and sensitivity corrected EUV spectra for the two inner MCP strips under pulsed operation.

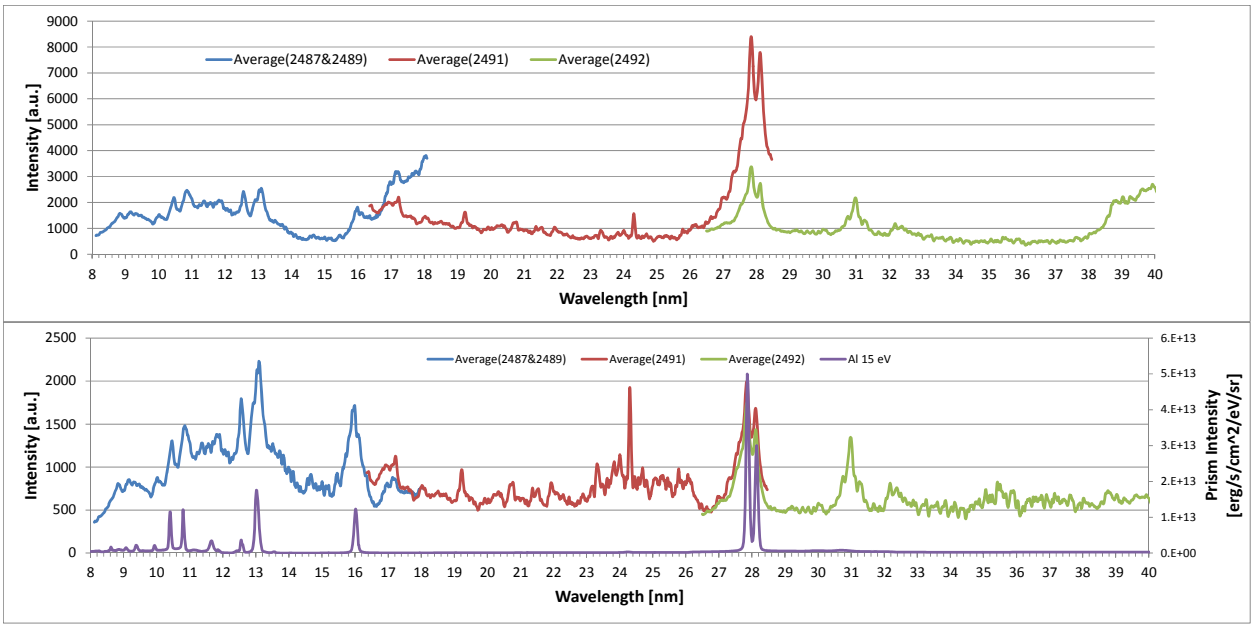

Figure 39. EUV spectra before and after sensitivity corrections. A better match with the PrismSPECT atomic modeling (for T_e=15 eV) is also achieved.

When the sensitivity corrections are applied, overlapping sections of the EUV spectra show a fairly good continuation (Figure 39).

5.13 Conclusions

The processing of the MCP images of the EUV spectrometer requires both background subtractions and sensitivity adjustments. The pulsed sensitivity adjustments were vastly different from the DC sensitivity measurements. The output from the MCP is blurred by an exponentially decaying function during the image transfer from the MCP phosphor, through the 3:1 fiber-optic reducer, the two Nikkor lenses, to the CCD chip. The attempt to use a convoluted image of the exponentially decaying function with the MCP image for background subtraction was successful when the convoluted background was scaled for each pixel slice in the y-direction.

6 Collaboration on FRCHX and PLX Experiments

6.1 Development of a 7-Channel Bias Box for Photodiode Arrays

We developed a 7-channel photodiode array with AXUV-type photodiodes that have directly deposited filters. The photodiodes require a DC reverse biasing of maximum 50 V and we therefore developed a compact 7-channel bias box powered by a 45 V battery. We added circuitry that monitors the reverse current drawn by each photodiode and individually indicates with a red LED if the current is too high. It also can test for forward current which indicates proper function of the photodiodes via green LEDs. Finally, we added a battery test switch with a green LED that indicates sufficient voltage of the bias battery.

In the biasing circuit, each photodiode has five 1 μF, one 0.1 μF and one 0.01 μF. The smaller capacitors are for improving the frequency response. Each circuit has a charge resistor of 10 kΩ and the battery is buffered by another set of low inductance caps, such that cross-talk through the bias circuit is eliminated.

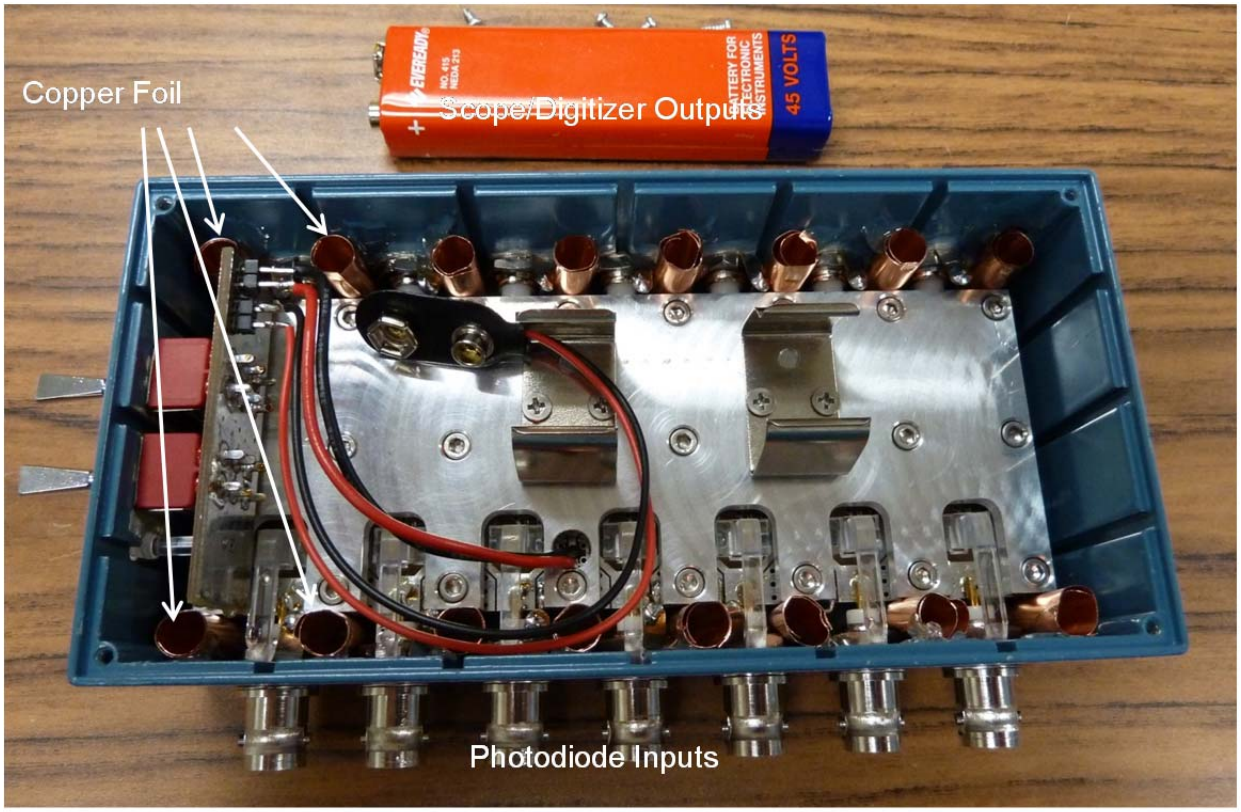

Figure 40. Picture of the 7-ch bias box. Each channel is shielded by means of PCB ground planes, aluminum cover and additional copper foils to suppress crosstalk.

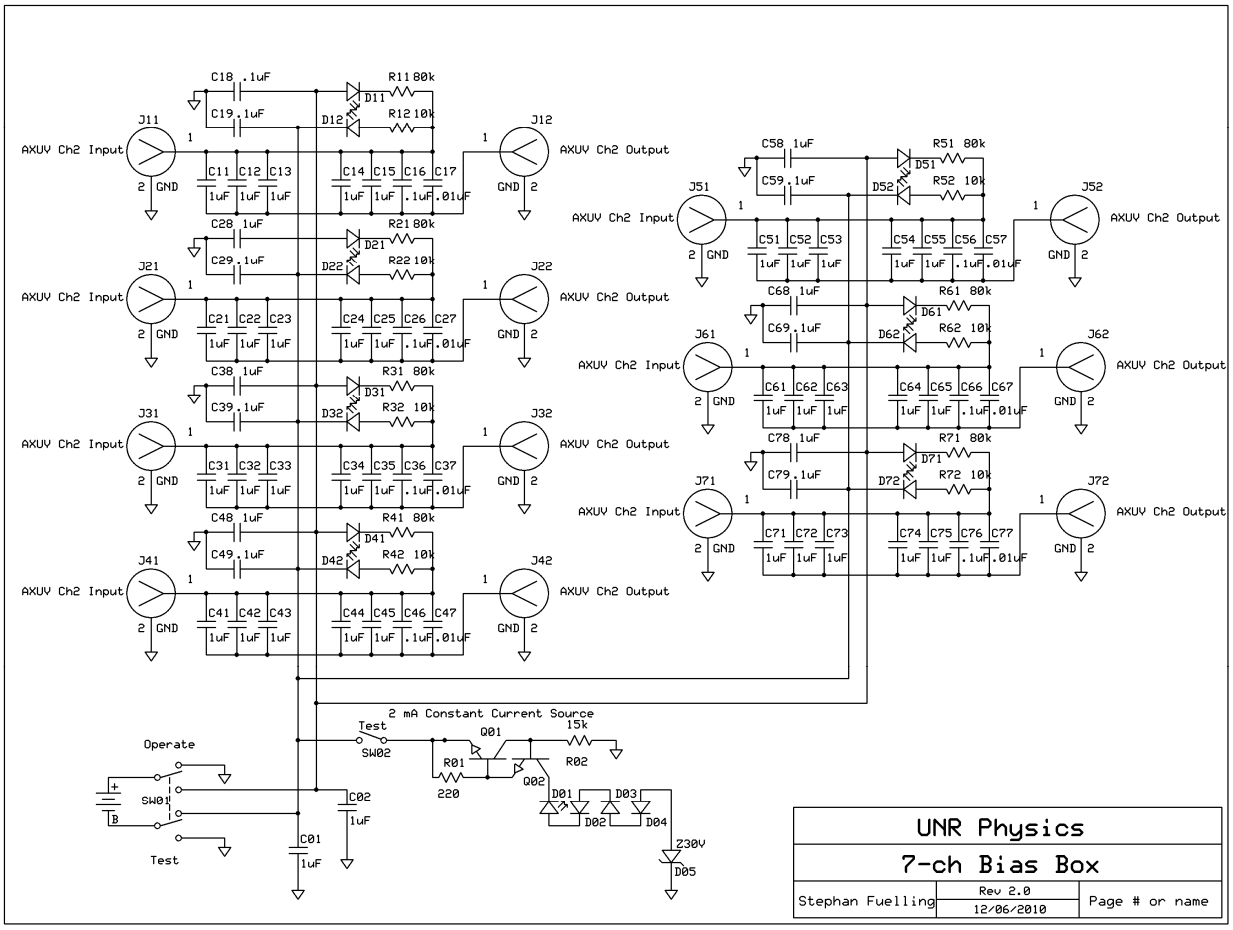

Figure 41. Circuit diagram of the 7-channel bias box.

Each channel is equipped with a two-color LED, which indicates a fault (red, for too high bias current) or whether the photodiode responds to a forward bias (green LED), for the forward bias test the polarity of the battery is temporarily reversed. This simple test circuit indicates shorted or damaged photodiodes that are either open circuit or draw too much bias current. In our experiments on Zebra, we have often encountered the problem of faulty photodiodes, due to damage from debris or irradiation. The battery test is accomplished via a 2 mA constant current source that is biased at about 33 V, such that the battery indicator LED won't light if the battery voltage drops below 33 V.

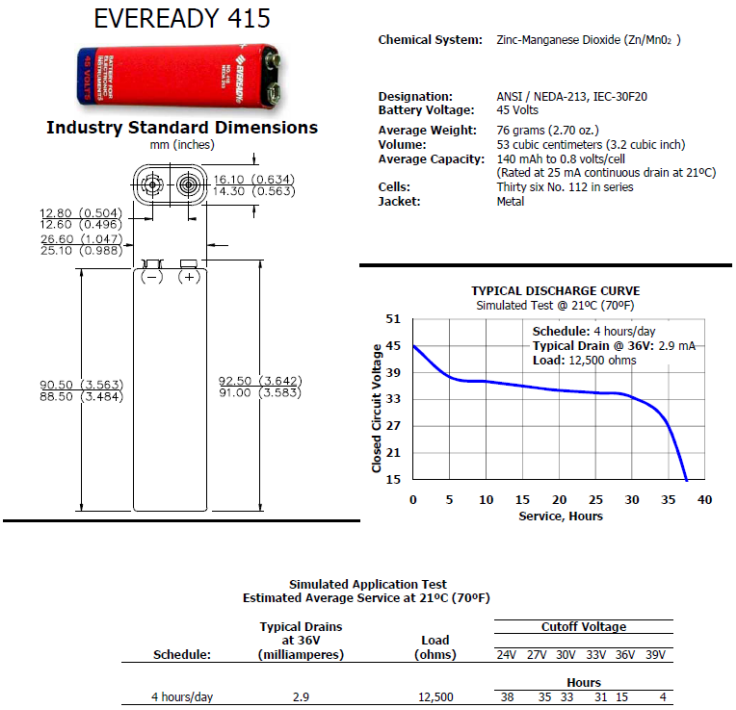

Figure 42. Specification of the Eveready 415; the nominal voltage is 45 V. From the graph on the right, one can see that the battery has to be replaced when the voltage reaches about 33 V.

In Figure 42, the battery specifications are shown. The discharge curve shows a knee in the voltage vs. service hours at about 33 V. At this voltage the battery has reached the end of its service life. This is why we choose the battery indicator light to extinguish at that voltage and it will become dim before that. Since the frequency response of the high capacity MLCCs is limited, we added two capacitors of lower capacitance to increase the frequency response. The frequency response of the MLCCs is shown in Figure 43.

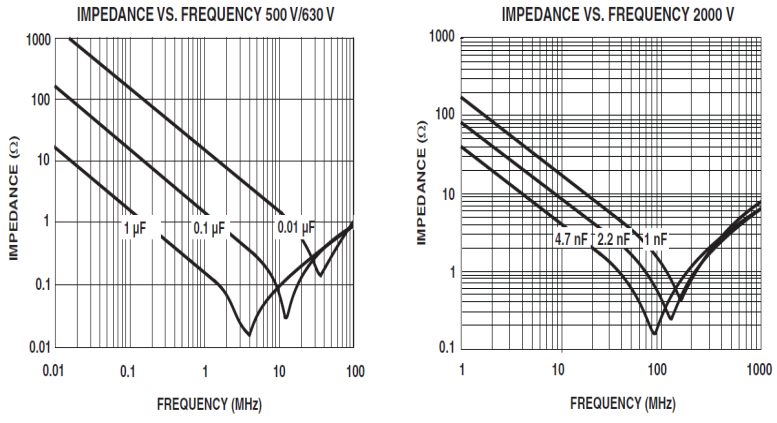

Figure 43. Frequency response of Vishay non-magnetic multilayer ceramic capacitors (from Vishay MLCC literature). By combining MLCC of different capacitance on can improve the frequency response.

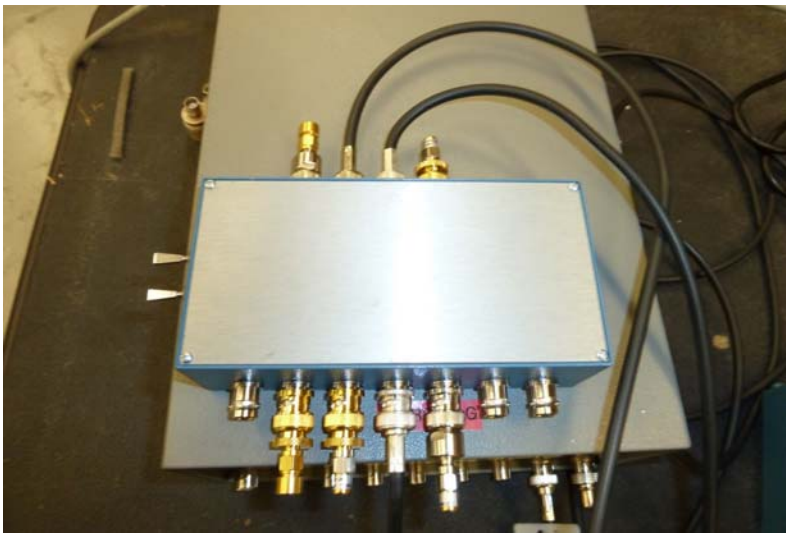

Figure 44. Bias box cross-talk test. One channel of the bias box is connected to a Stanford Research DG 535 and the neighboring channels are monitored for crosstalk signals. In this example, the signal from the DG535 is fed into ch#4 'Diode input' and monitored at ch#3 and ch#4 'Scope Output'. Neighboring channels are terminated with 50 Ohm, also the input of ch#3.

We tested the 7-ch bias box by applying a fast rising pulse on one channel and measuring the crosstalk pulse on the adjacent channels (Figure 44). We terminated the other ends with 50 Ω, as it would be under normal operational conditions. This also increased the crosstalk, due to stronger magnetic coupling between neighboring channels. However, due to carefully shielding, the crosstalk was minimized to below 60 dB (Figure 45 and Figure 46).

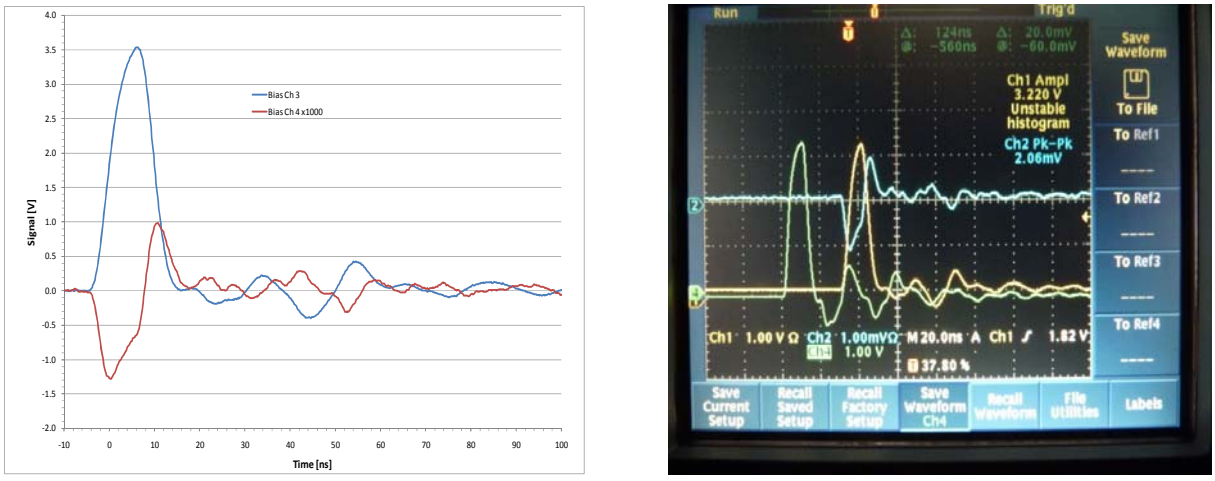

Figure 45. Result from the crosstalk measurement with wire mesh placed in the gaps between the BNC connectors to reduce inductive coupling. The signal is applied to ch 5 and read out on ch 4 (x 1000). There is a better than 60 dB suppression of crosstalk between the channels.

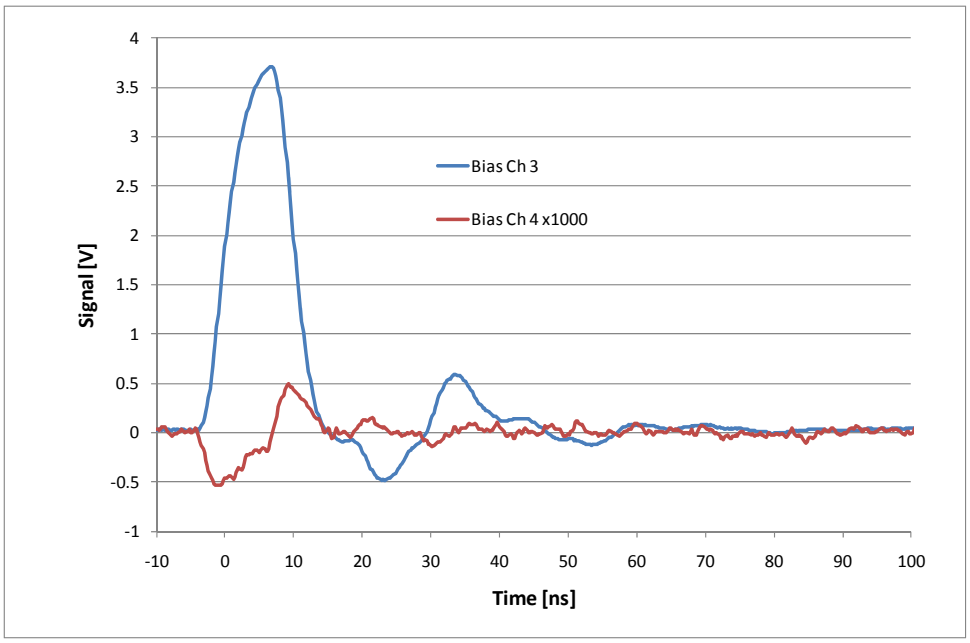

Figure 46. Improvement of the crosstalk reduction by using copper foil between adjacent BNC connectors to reduce inductive coupling. The crosstalk is reduced well below 60 dB.

Connections and Operation

The input and output channels and the switches were labeled as shown in Figure 47. We used switches that for the up position had a 'momentary ON' state, by releasing the switch it would go back to the 'OFF' position. This would allow for a quick test and prevent the switch to stay in that position and drain the battery.

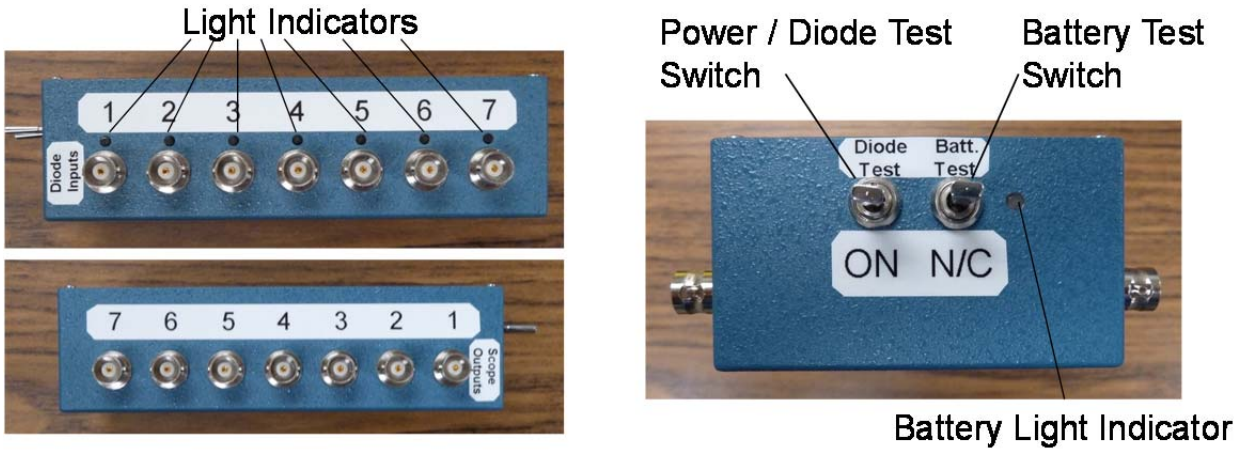

Figure 47. Several views of the 7-channel bias box to show photodiode inputs and outputs, as well as the power/diode test switch and the battery test switch.

Test Procedure:

- To test proper connection to diodes, keep left switch in the 'Diode Test' position:
  - At each 'Diode Input' channel, light indicator should show **green**
- To turn bias battery power on, push left switch down ('ON'),
- To test bias battery voltage, move right switch up ('Batt. Test'), battery light indicator should light up bright **green**
- At any time, if any photodiode is shortened or draws a lot of bias current, the corresponding light indicator will show a **red** light at that channel

6.2 Electron Impact from Plasma on Al-Coated AXUV Photodiodes

For plasma emission measurements on the FRCHX experiment at Shiva Star at the Air Force Research Laboratory in Albuquerque, New Mexico, we designed a 7-channel photodiode array. Since fast electrons from the FRC plasma could impact the photodiode detector, we examined the likelihood that hot electrons could penetrate the directly deposited aluminum film (200 nm thickness) and cause the generation of electron-hole pairs in the silicon photodiode.

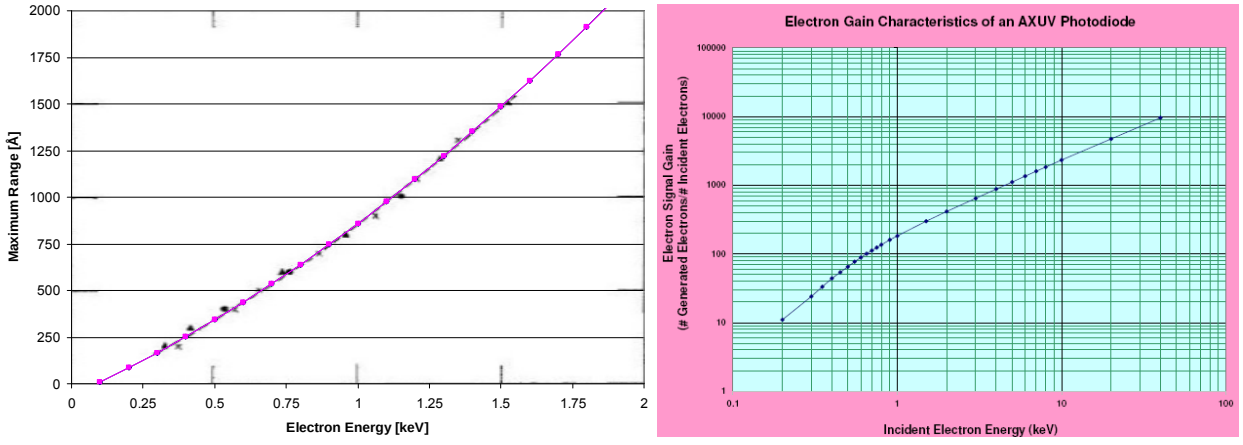

Figure 48. Graphs taken from S. Thomas and E.B. Pattinson, "Range of electrons and contribution of back-scattered electrons in secondary production in aluminium," 1970, J. Phys. D: Appl. Phys. **3**, 349, (http://iopscience.iop.org/0022-3727/3/3/315) and "Electron Gain Characteristics of an AXUV Photodiode," from http://www.ird-inc.com/electron-detectors.htm. The experimental data has been fitted and extrapolated to higher electron energies.

From Figure 48, a 200nm thick Al film will protect from electrons with up to ~2keV energy. The AXUV photodiode is a very good electron detector: 1 hole-pair per 4-5 eV! The fitted curve follows the following quadratic equation (E in keV and R in Å):

$$R(E) = -63.1 + 702 \cdot E + 220.5 \cdot E^2$$

Our Al films are 200 nm thick, so electrons with E > 2 keV will pass through. The Maxwell energy distribution is:

$$f(E) = \frac{2}{\sqrt{\pi}} \left(E_{therm}\right)^{-3/2} \sqrt{E} \exp\left(-E / E_{therm}\right)$$

For each electron with kinetic energy E > 2 keV, $(E\text{-}E_{loss})/E_{pair}$ number of electron-hole pairs will be generated in the silicon, where E_{loss}= 2 keV, the energy loss due to the Al film. Therefore,

$$F = \int_{E_{loss}}^{\infty} \frac{E - E_{loss}}{E_{pair}} f(E) dE$$

The integration for E_{pair} = 5 eV and E_{therm}= 300 eV yields F = 0.253.

For a given electron density n_e, plasma column length L, and detector area A (= 0.01 cm^2) N hole pairs will result:

$$N = n_e \cdot F \cdot L \cdot A$$

Assuming an FRC density of 5x10^{16}cm^{-3}, and that the FRC 'exhaust' is 1/10 of that, then n_e = 5x10^{15}cm^{-3}. With a plasma column length of 10 cm, the number of electron-hole pairs is

$$N = 5 \times 10^{15}\,\mathrm{cm}^{-3} \cdot 0.32 \cdot 10\,\mathrm{cm} \cdot 10^{-2}\,\mathrm{cm}^2 = 1.6 \times 10^{14}$$

If this occurs over a time period of t = 1μs, then a current of $I = N \cdot e / t = 26\mathrm{A}$ is generated, giving rise to a voltage of $V = I^*R$ = 1300 V.

Now let us consider the angular distribution of the thermal electrons. We must integrate over all possible angles and account for longer pathways (Figure 49).

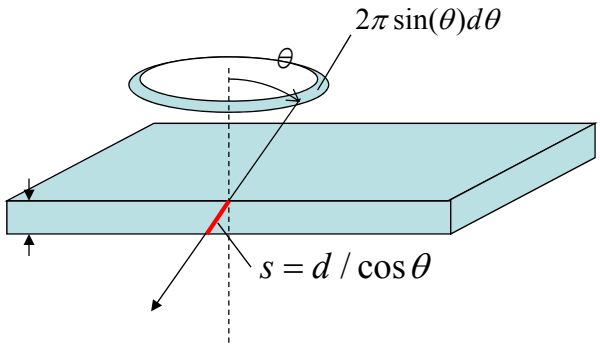

Figure 49. Integration over the angular distribution of the electrons penetrating the thin aluminum coating.

Using the asymptotic function of the electron range R in Al films makes the integration easier:

$$R = (E - 0.39\text{keV}) * \frac{2000\text{Å}}{1.5\text{keV}}$$

We solve for E and set $R = d/\cos(\alpha)$:

$$E = E_{\text{loss}}(\alpha) = \frac{d}{\cos(\alpha)} \frac{1.5\text{keV}}{2000\text{Å}} + 0.39\text{keV}$$

E is now the energy loss due to the passage through the film at an angle α. The integration over the electron distribution and all angles, with d = 2000Å:

$$F = \frac{1}{2} \int_0^{\pi/2} \sin(\theta) \int_{E_{\text{loss}}}^{\infty} \frac{E - E_{\text{loss}}(\theta)}{E_{\text{pair}}} f(E) dE d\phi, \text{ with } E_{\text{loss}}(\theta) = \frac{1.5\text{keV}}{\cos(\alpha)} + 0.39\text{keV}$$

The result from MathCad is F = 0.028 for T_e= 300 eV, about 1/9 of the earlier result of 0.253 for the constant path length.

The graph in Figure 50(a) shows the resultant AXUV photodiode signal as a function of electron temperature for the same plasma parameters. Thermal electrons become important for T_e > 125 eV (signal > 10 mV). The contour plot in Figure 50(b) shows the signal voltage in [V] generated by hot electrons. The contour limit of '-2' is 10 mV and represents the critical signal voltage, which could interfere with the photon signal measurement.

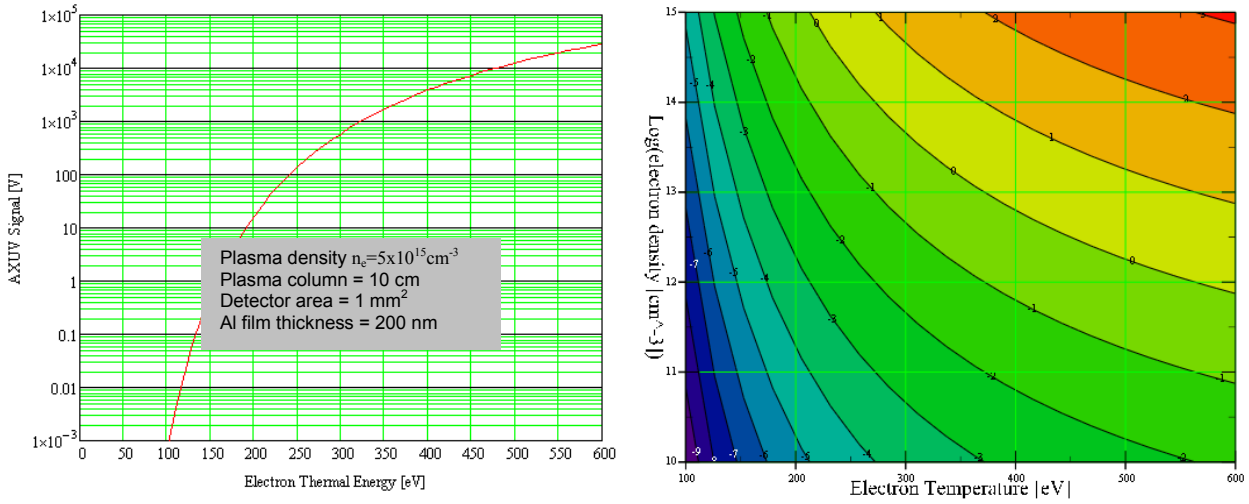

Figure 50. AXUV Signal (a) and electron density (b) vs. electron temperature in eV.

6.3 Calculation of Signal Levels from PrismSPECT Ar Plasma Emission Modeling

The plasma liner experiment (PLX) at the Los Alamos National Laboratory needed spectroscopic diagnostics for measuring the argon plasma emissions in order to calculate plasma density and temperature. We analyzed the optical coupling requirements to fiber optic cables and performed PrismSPECT simulations to predict signal levels and detection efficiency requirements.

6.3.1 Collection optics

In Figure 51, the plasma bullet has a diameter of D_P = 10 mm and the fiber diameter D_F = 0.1 mm, therefore the lens system has to de-magnify by at least a factor $M = D_P/D_F$ = -100. Also $M = f/(f-x_1) = -x_2/x_1$, solving for f: $|f| = |x_2/(M-1)| = 13.6$ mm

This is the maximum focal length; shorter focal lengths will work too but will have a larger field of view.

6.3.2 Timing considerations and lens *F/#*

The plasma passes the view of the fiber optic lens only for a short time. For $v \approx$ 50-70 km/s the observation time for a 1 cm large plasma object is $\tau \approx$ 140-200 ns. Shorter focal lengths will track the plasma bullet for a longer time, however one should not reduce the *F/#* to less than unity, otherwise the light will not be transmitted by the fiber optic cable. The $F/\# = f/D > 1$, therefore the lens diameter should not be larger than the focal length (or the fiber will not catch all the light).

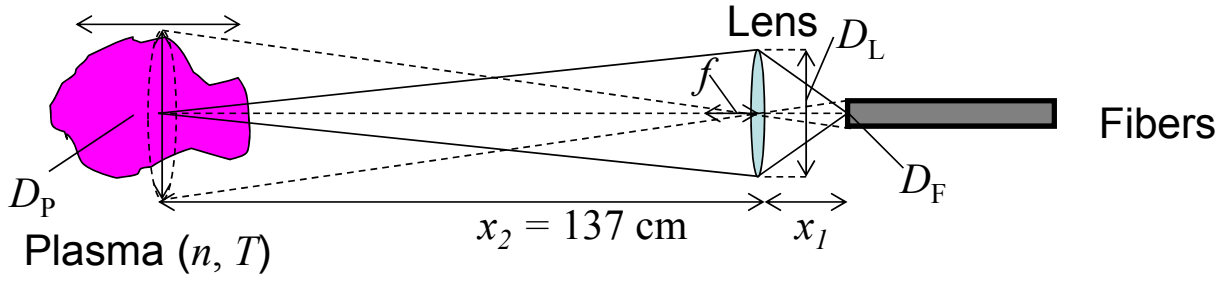

Figure 51. Diagram of the collection optics. Shown are the argon plasma, the lens and the fiber optic cable.

Table 6.1. Thorlabs lenses

350 - 700 nm AR-Coated Precision-Polished Large-Diameter Aspheric Lenses

Order

Based on your currency / country selection, your order will ship from Newton, New Jersey

+1QTY	Part Number - Imperial	Price	Available/Ships
0	AL108-A - Ø10 mm, f=8 mm, NA=0.547, S-LAH64 Aspheric Lens, ARC: 350-700 nm	$142.00	√ Today
0	AL1210-A - Ø12.5 mm, f=10 mm, NA=0.545, S-LAH64 Aspheric Lens, ARC: 350-700 nm	$164.00	√ Today
0	AL1225-A - Ø12.5 mm, f=25 mm, NA=0.230, N-BK7 Aspheric Lens, ARC: 350-700 nm	$164.00	√ Today
0	AL1512-A - Ø15 mm, f=12 mm, NA=0.546, S-LAH64 Aspheric Lens, ARC: 350-700 nm	$175.00	√ Today
0	AL1815-A - Ø18 mm, f=15 mm, NA=0.534, S-LAH64 Aspheric Lens, ARC: 350-700 nm	$190.00	√ Today

6.3.3 Ideal lens

The collection optics should have

- An *F/#* 2 or *NA* ~ 1
- A collection angle of $\Theta \sim 0.43°$
- A focal length of $f \leq 13.6$ mm
- A lens diameter that collects sufficient light but with the restriction of $D = f/(F/\#) \approx 11$ mm (for $f = 11$ mm and $F/\# = 1$)

Best collection optics with adjustable focus: $f = 12$ mm, $NA = 0.5$, $D = 12$ mm.

From Table 6.1, we choose the AL1512-A since it is the best candidate, with $f = 12$ mm, $NA = 0.546$, and $D = 15$ mm. The useful diameter of the lens will be $D = 12$ mm. The lens is unmounted and needs to be integrated with a F/O coupling.

6.3.4 Collection optics for best lens

Light emission from plasma with density n, temperature T and thickness d is collected by a lens with diameter D_L and focal length f at a distance x_2 and focused into a fiber (bundle) at distance x_1 (Figure 51). The collection solid angle is about

$$\Omega = \pi * sin^2(0.42°/2) = \mathbf{4.2x10^{-5}\ sr}$$

The area of the lens is $A = \pi*(D/2)^2$, e.g. for $D = 12$ mm, $\mathbf{A = 1.13\ cm^2}$

In order to use the PrismSPECT output (for a given set of plasma parameters *n, d, T*) to estimate the amount of light collected from the plasma, we have to multiply the intensity *I* (erg/eV/cm^2/s/sr) with the product $\Omega*A$, multiplied by the integration time *t* (s) and by the energy interval *dE* (eV).

Furthermore, all the various efficiencies need to be considered:

- Fiber-optic coupling 70% into the fiber and 70% out of the fiber, total ~ 50%
- Fiber attenuation
- Grating efficiency (20%-40%)
- Q.E. of the CCD camera (max. 50% for front-illuminated, 90% for back illuminated, wavelength dependent)

6.3.5 Energy interval

From $E = hc / \lambda$ we get: $dE = -(hc / \lambda^2) d\lambda$

$$\Delta E \approx 3.2\text{x } 10^{-4} \text{ eV}$$

at λ = 620 nm, also using the spectral resolution of $\lambda/\Delta\lambda$ = 6200, which is also used in the PrismSPECT plot. Each fiber has its own collection optics and the spectral image height of a 100 μm fiber will illuminate about 10 CCD pixels vertically, which should be binned, if possible.

6.3.6 Intensity estimate for Te = 3 eV, n = 10^{17} cm^{-3}, thickness 1cm, non-LTE.

The energy interval was 3.2x 10^{-4} eV and the collected light from the lens was distributed height-wise over 10 CCD pixels. The PrismSPECT intensity gives 2.4x10^{10} erg/eV/cm^2/s/sr = 2.4x10^3 W/eV/cm^2/sr (Figure 52). For a plasma observation time of t = 200 ns, with 1 erg = 10^{-7}J and λ = 620 nm (2 eV), we will have about 2.3x10^7 photons. Considering the various efficiencies, we may end up with about 10% of that, and this is distributed over 10 pixels vertically by 10 pixels horizontally (total attenuation of 1/1000 for each pixel total). Therefore, each CCD pixel should receive 23,000 photoelectrons, compared to the well-depth of each pixel of 75,000 e^-. We can bin the ten vertical pixels and could capture 230,000 e^-.

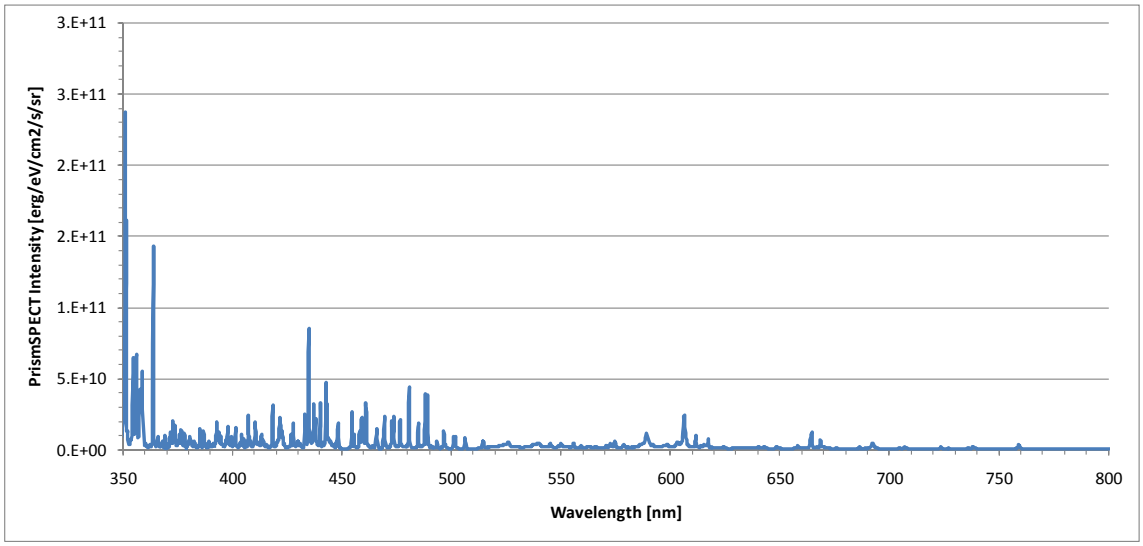

Figure 52. Argon jet emission spectrum for T_e = 3 eV, n = 10^{17} cm^{-3}, thickness 1cm, non-LTE.

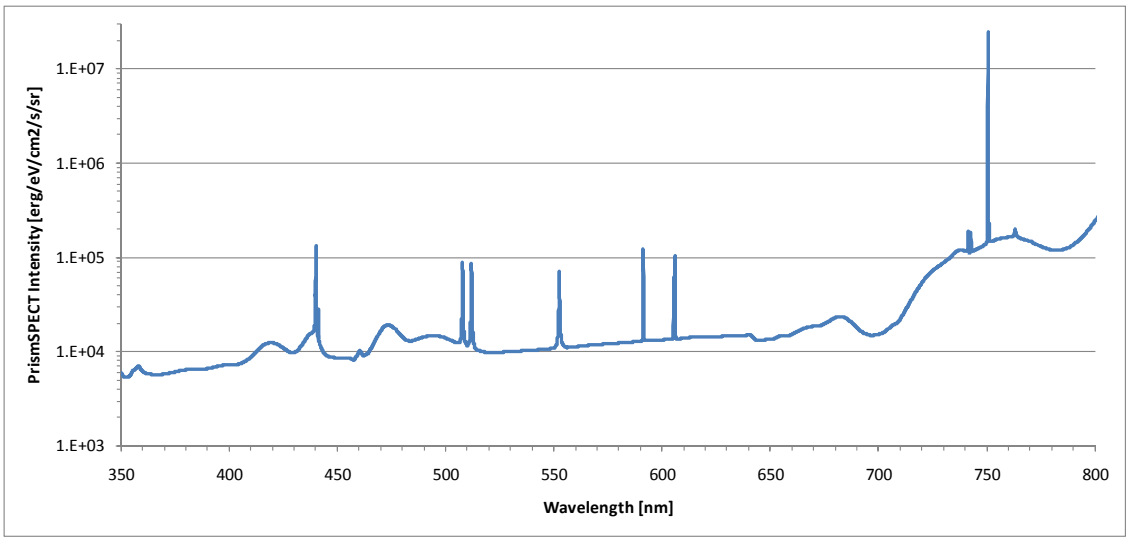

Figure 53. Argon jet emission spectrum for T_e = 1 eV, $n = 10^{15}$ cm^{-3}, thickness 1cm, non-LTE.

6.3.7 Intensity estimate for Te = 1 eV, $n = 10^{15}$ cm^{-3}, thickness 1cm, non-LTE

The line intensity at around 620 nm for the lower temperature and density is about factor 2.4x10^5 smaller, which would result in about one photoelectron per ten binned CCD pixels (Figure 53).

6.3.8 Conclusions

We estimate about 23,000 photoelectrons generated in the CCD pixels that record the line emission at 620 nm from a 1 cm^3 plasma 'bullet' with a density of $n = 10^{17}$cm^{-3} and a temperature of T_e= 3 eV. We also estimated about one photoelectron per ten binned pixel for a 1 cm^3 plasma 'bullet' with a density of $n = 10^{15}$cm^{-3} and a temperature of T_e= 1 eV. Expansion and cooling drastically reduces the number of photons emitted. The lens-coupled light collection may not be sufficient for lower temperature, lower density plasma. Larger collection optics, like a parabolic mirror, cannot improve the result due to the focal length and *F/#* restrictions. However, other spectral lines than chosen here may produce better results. Better light collection is only possible by moving the light collection closer to the path of the plasma jet.

6.4 CCD Camera Adaptation to a Jobin-Yvon CP-140 Compact Spectrometer

We shipped our compact Jobin Yvon CP-140 spectrometer to the Physics Liner Experiment (PLX) at LANL. The team at PLX wanted to equip the CP-140 with a liner fiber-optic bundle at the input and with a CCD at the output port to capture emission spectra of the argon plasma that is generated by the plasma guns. Figure 54 shows a picture and drawing of the CP-140.

The specifications of the CP-140 are

- F/2 with 140 mm focal length
- Grating: 400-1100 nm (grating purchased)
- 230 g/mm
- 23.3 mm length of spectrum
- Image plane: 25.83 mm from exit port
- Slit: 100 µm x 8.25 mm

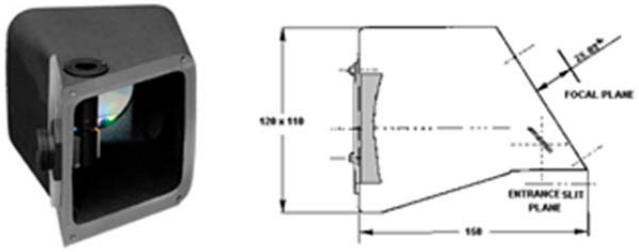

Figure 54. Picture and mechanical drawing of the CP-140.

Since there were no detailed mechanical drawings available for the CP-140, we made a mechanical model to ease the CCD camera adaptation at PLX. Figure 55 shows a more detailed drawing of the SP-140 and the proposed CCD camera mounting plate.

The CCD sensor has to be placed 25.83 mm from the exit port and centered on the 23.3 mm wide image plane of the spectrometer. The entrance slit measures 100 µm x 8.25 mm. The mounting plate needs four mounting holes with a hole pattern of 80 mm wide and 96 mm high for M4 holes. A rectangular window allows the spectrum to pass through. On this plate, the CCD camera can be mounted.

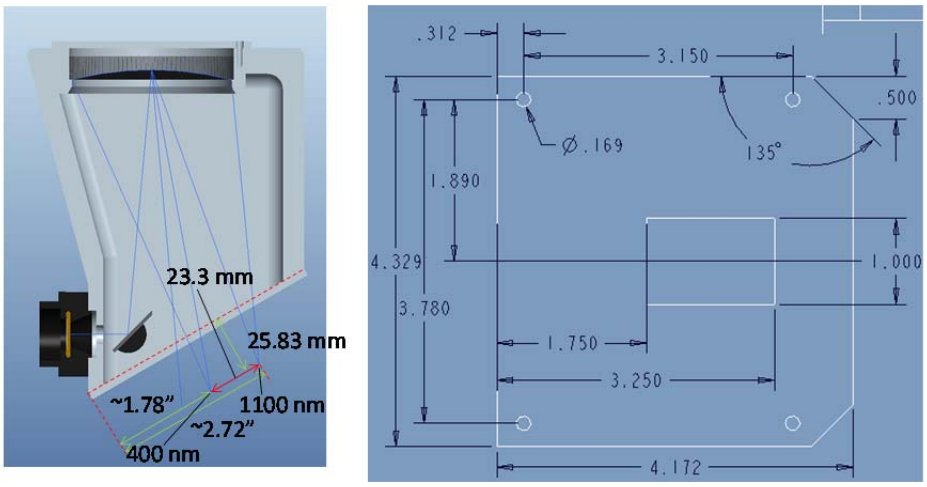

Figure 55. Mechanical drawings of the CP-140 and the proposed output port mounting plate for mounting the CCD camera to the CP-140.

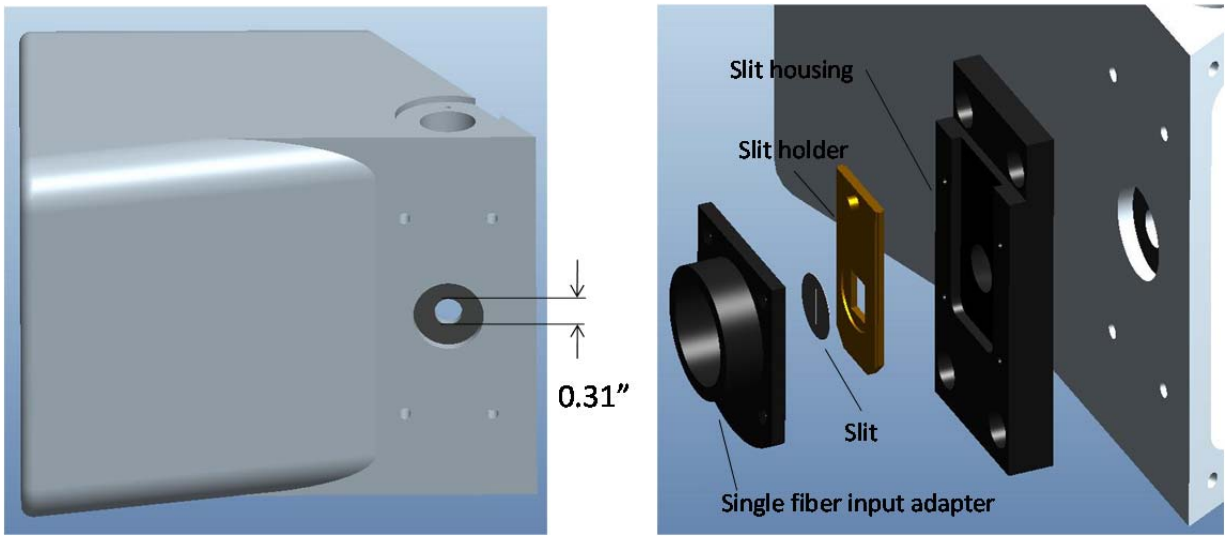

Figure 56. Input port and slit assembly modifications.

For the linear 10 fiber bundle, the input port needs to be enlarged. From factory, the input port diameter is about 0.31” (see Figure 56). The fiber optic bundle needs an adapter, which will be installed instead of the current single fiber input adapter.

Figure 57 shows the mechanical drawings for the slit housing and the slit holder. These have to be modified in order to accommodate the linear fiber optics array.

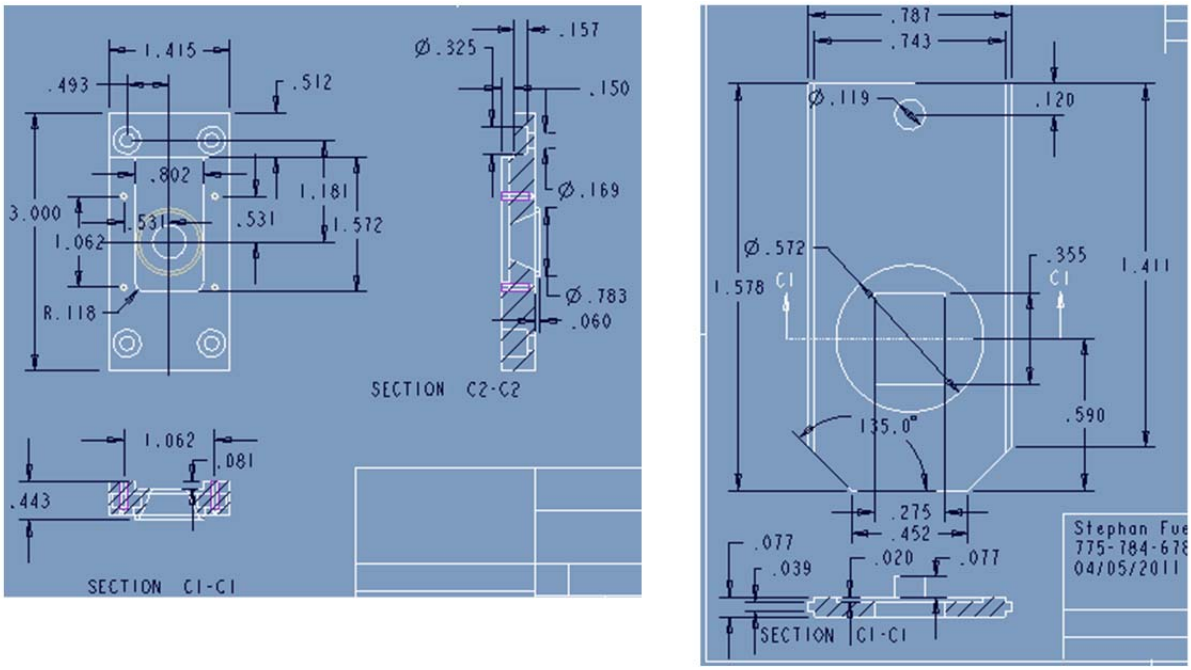

Figure 57. Mechanical drawings for the slit housing and the slit holder.